Department of Physics

Faculteit Wetenschappen

Departement Fysica

Tight-binding investigation of the electronic properties of phosphorene and phosphorene nanoribbons

Tight-binding onderzoek van de elektronische eigenschappen van fosforeen en fosforeen nanostructuren

Thesis submitted to achieve the degree of doctor of science by
Esmaeil Taghizadeh Sisakht

Supervisors:
Prof.dr. Farhad Fazileh
Isfahan University of Technology, Iran
Prof. dr. François Peeters
University of Antwerpen, Antwerpen, Belgium

Academic year 2018-2019

January 2019

DEDICATION

I dedicate my thesis to God who has been my guide during all my life. My faith in Him always empowered me with the courage to help me cross each hurdle that I came across as I did this thesis.

Also, I dedicate my thesis to my wife Khadijeh, my son Mohammad Mahdi and my loving parents who have made me stronger, better and more fulfilled than I could have ever imagined.

Members of the Jury:

Chairman
Prof.dr. Ismaeil Abdolhosseini Sarsari, Isfahan University of Technology, Iran

Supervisors
Prof.dr. Farhad Fazileh, Isfahan University of Technology, Iran
Prof.dr. François Peeters, Universiteit Antwerpen, Belgium

Members
Prof.dr. Farhad Shahbazi, Isfahan University of Technology, Iran
Prof.dr. Ismaeil Abdolhosseini Sarsari, Isfahan University of Technology, Iran
Prof.dr. Gholamreza Rashedi, University of Isfahan, Iran
Prof.dr. Mohammad Mardani, Shahrekord University, Iran

Contact Information

Esameil Taghizadeh Sisakht
G.U. 205
Groenenborgerlaan 171
2020 Antwerpen
Belgium
etsisakht28@gmail.com

ACKNOWLEDGEMENT

Contents

List of Figures

List of Tables

List of abbreviations

2D	Two-dimensional
2DEG	Two-dimensional electron gas
2D TI	Two-dimensional topological insulator
3D	Three-dimensional
3D TI	Three-dimensional topological insulator
Al_2O_3	Aluminum oxide
aPNR	Armchair phosphorene nanoribbon
ARPES	Angle-resolved photoemission spectroscopy
BBP	Bulk black phosphorus
BCB	Bulk conduction band
BN	Boron nitride
BP	Black phosphorus
BVB	Bulk valence band
BZ	Brillouin zone
CBM	Conduction band minimum
DFT	Density functional theory
DOS	Density of states
FET	Field effect transistor
FQHE	Fractional quantum Hall effect
GGA	Generalized gradient approximation
HBZ	Half the Brillouin zone

HgTe	Mercury telluride
HOTI	Higher order topological insulator
IQHE	Integer quantum Hall effect
LDA	Local density approximation
LL	Landau level
MBP	Monolayer black phosphorus
MLP	Monolayer phosphorene
MoS_2	Molybdenum disulfide
NI	Normal insulator
n-n	Next-nearest
P	Phosphorus atom
PNR	Phosphorene nanoribbon
QHE	Quantum Hall effect
QSHE	Quantum spin Hall effect
SiO_2	Silicon dioxide
SO	Spin-orbit
SOC	Spin-orbit coupling
SSB	Surface state band
STM	Scanning tunneling microscopy
STS	Scanning tunneling spectroscopy
TB	Tight-binding
TCI	Topological crystalline insulator
TI	Topological insulator
TM	Topological metal
TMD	Transition metal dichalcogenide
TRIM	Time-reversal invariant momenta
TRS	Time-reversal symmetry
VBM	Valence band maximum
vdW	van der Waals
zPNR	Zigzag phosphorene nanoribbon

Introduction

Recent decade has experienced an increasing interest in two-dimensional (2D) and quasi-2D structures. The starting point for such substantial scientific movement was the experimental discovery of graphene in 2004 [1] which raised the hopes for application of these structures in technology. Among the wide list of these structures, graphene, transition metal dichalcogenides (TMDs), and monolayer black phosphorus (MBP) have been in the focus of these studies due to their excellent electronic, mechanical, optical, thermoelectric and optoelectronic properties[2–9].

Although graphene is the most important candidate because of its high carrier mobility and excellent mechanical properties [3, 4], the lack of an energy gap [3] in its band structure limits its performance. These limitations were the motivation for researches on other layered structures with semiconducting characters which have the potential of being used in electronic devices. In his regard, the next generation that has been in the focus of attention is layered TMDs [10].These structures are layered in the form of single MX_2 sheets in which M is a transition metal such as V, W, Mo or Pt and X represents a chalcogen like Se, S or Te [10]. These single sheets are not single atomic layers; but they are rather formed in X-M-X configuration in a way that the metal is compacted between two chalcogen layers. That is why these structures are known as quasi-2D [10]. In this family, molybdenum disulfide (MoS_2) has been in the focus of studies due to its robustness [11]. As a TMD, MoS_2 has a direct band gap of $\sim 1.8eV$ [12] and a relatively high on/off ratio ($\sim 10^8$) [13] which is one of the most important parameters in the transistor industry. Therefore, the existence of a strong spin-orbit interaction[11] in addition to the desired electronic and

mechanical properties of this structure have made this material one of the most interesting candidates of 2D materials for fundamental and applied studies.

However, one of the important drawbacks of MoS_2 in comparison with graphene is its low carrier mobility [9]. The experimental measured charge carrier mobilities of a suspended sheet of monolayer graphene and a sheet of monolayer graphene on a substrate are $\sim 200,000$ cm^{2}V^{-1}s^{-1}, and $\sim 2,000$-$5,000$ cm^{2}V^{-1}s^{-1}, respectively [9]; whereas the maximum theoretical value for electrons and holes in MoS_2 was estimated 320 cm^{2}V^{-1}s^{-1} and 270 cm^{2}V^{-1}s^{-1}, respectively [9]. Therefore, studies continued to find monolayer structures with semiconducting character which possess desired mechanical and electronic properties and also benefit from large carriers mobility in comparison with MoS_2. These researches resulted in the rediscovery of the previously known layered structure of bulk black phosphorus (BBP) [14].

1.1   Rediscovery of black phosphorus

The explosion of research interest in this structure can be regarded as rediscovery of black phosphorus. In what follows, the crystal structure of monolayer and few-layer black phosphorus (BP) will be introduced and some methods of preparation will be briefly reviewed.

1.1.1   Allotropes of phosphorus

Phosphorus (P) is a multiple valence non-metal element in the nitrogen group. This element has numerous allotropes with completely different properties [10]. The first records about the description of a phosphorous compound dates back to 3000 years ago in China [9]. White, red and black phosphors are among the most famous allotropes of P [9]. White phosphorus is one of the most important stable allotropes of phosphorus which was discovered in 1669 [9]. It is available in molecular form with tetrahedron P_4 structure. In 1914, Percy Bridgman observed a phase transition during high-pressure investigation of white phosphorus and called the new phase black phosphorus [10]. Although the discovery of BP occurred centuries after the discovery of elemental phosphorous, it is the most stable allotrope of P [10].

1.1.2   Crystal structure of BP

One of the main properties of 2D materials is the formation of strong covalent bonds between atoms of each layer, whereas the inter-layer bonds are formed via van der Waals

(vdW) interaction. In other words, the weak vdW force between layers results in a small amount of energy for separation of the layers. BP is a 2D layered material similar to graphite with the difference that the covalent bonds in a graphite layer have sp^2 hybridization while the hybridization of covalent bonds in a layer of BP is sp^3 [9]. This difference in the hybridization is the reason for the hexagonal structure of graphite while the most stable structure of BP is base-centered orthorhombic [9]. Figure 1.1 shows the crystal structure of BBP and its corresponding first Brillouin zone (BZ). Each unit cell contains eight P atoms with four atoms per layer as indicated by 1-4 and 5-8 in Fig. 1.1 (b). As shown in Figs. 1.1 (a) and (c), the structure is composed of puckered layers stacked along the z axis. In other words, the atoms of each layer are not located in the same plane; but each layer includes an upper and a lower chain of P atoms. We also have shown the lattice constants of this structure whose experimental values are: $a = 4.374$ Å, $b = 3.313$ Å, and $c = 10.473$ Å [15]. Due to the existence of two different bond angles $96.34°$ and $103.09°$, each atom has two neighbors located at distance 2.224 Å and a third one that rests at the distance of 2.244 Å [9].

Note that BBP layers can exist in three types AA, AB and AC stacking [16]. However, since the AB stacking is the most stable form in the experimental synthesis, throughout this thesis, by BP, we refer to the AB stacking.

Based on the nomenclature standards, the appropriate name for MBP is phosphane [17]. However, because it has often called phosphorene in the literature, we will also use this more well-known name throughout this thesis.

In what follows, the experimental methods for synthesis of BBP and few-layer phosphorene (FLP) will be discussed.

1.1.3 Preparation of phosphorene

By applying the pressure of 1.3 Pa to a sample of white phosphorous at $200°$C in a short time, Bridgman observed a phase transition which was accompanied by a change in the color of the sample and a reduction in the volume [10]. After his discovery, more attempts were made by researchers to improve the synthesizing of BBP with the same method. From late 1960s, increasing interest in superconductivity resulted in focusing on the rich phase-diagram of phosphorous which then led to the development of experimental methods for BP synthesis [18]. In 2007, it was revealed that BP can be produced by use of red phosphorous at lower pressures and $500°$C through adding small amounts of gold, tin and tin (IV) iodide [19]. Although this method results in good crystallinity, but the process is time consuming and about 10 to 70 hours are needed for formation of the new phase [9]. In this regard, development of a safe and efficient method capable of large-scale production with less time is one of the main challenges for future applications of phosphorene [9].
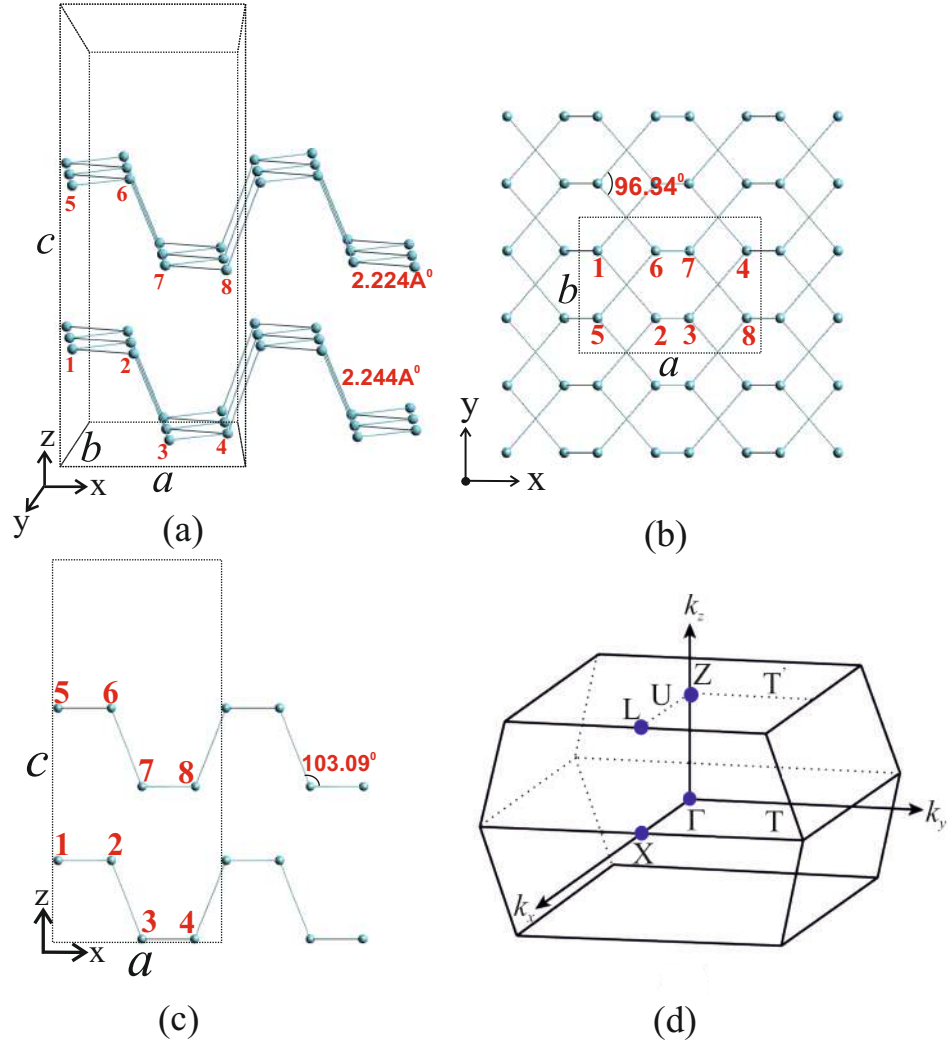
Figure 1.1: (a) The crystal structure of BBP. The lattice constants and the eight P atoms of a unit cell are shown. (b) and (c) show top and side views of BBP lattice structure. (d) Shown is the first BZ of BBP and some of important points in the reciprocal lattice.

Since BBP is classified as a vdW material, the top-down method which has been used for graphene synthesis from graphite can be also used for preparation of phosphorene from BBP. Phosphorene layers isolation was first reported by two research groups in 2014 [20, 21]. Currently, two main methods of Scotch-tape cleavage and liquid exfoliation are used for phosphorene preparation [9, 18, 20–22]. Many other top-down methods
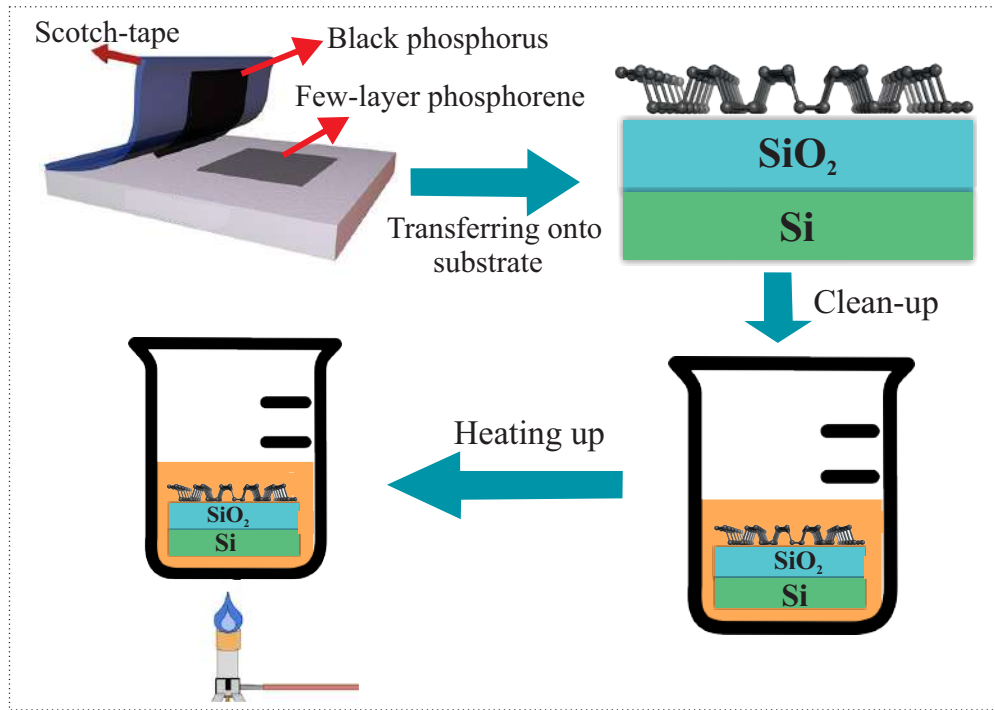
Figure 1.2: Schematic representation of mechanical exfoliation.

are also developing for this purpose [9]. In the following, we will briefly introduce the mentioned two main methods of Phosphorene production.

Scotch-tape cleavage

The schematic representation of phosphorene synthesis by Scotch-tape cleavage method is shown in Fig. 1.2. In this method, first, phosphorene layers are achieved by using tape to repeatedly peel off phosphorene sheets from BBP crystals. After multiple repetitions of this process, few-layers of BP are transfered on a SiO_2/Si substrate [20]. Then, the sample will be cleaned by acetone, isopropyl alcohol and methanol to remove any remaining substances. Finally, the sample will be heated up to 180 to remove the solvents [20]. This method can lead to the formation of good quality monolayer and FLP [9, 20]. However, the most important disadvantage of this method is the failure in large-scale production [9].
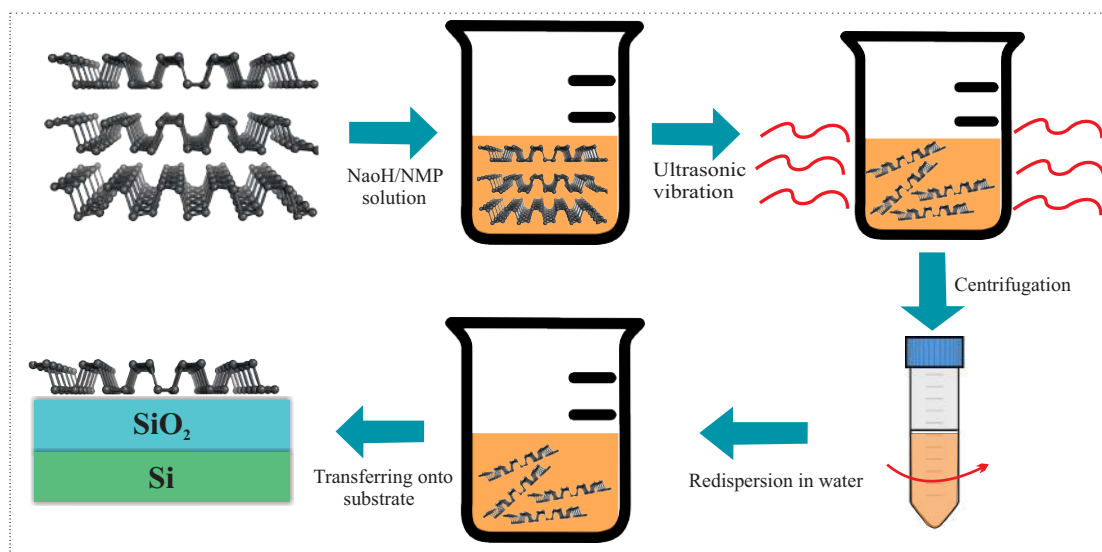
Figure 1.3: Schematic representation of liquid exfoliation methods.

Liquid exfoliation

As schematically illustrated in Fig. 1.3, in the liquid exfoliation method, one way to
achieve FLP is as follows [22]: first, BBP will be immersed into the saturated NaOH/NMP
(sodium hydroxide and N-Methyl-2-pyrrolidone) solution. After four hours of ultrasoni-
cation, it will be centrifuged in several steps. First, the centrifugation will be carried out
for ten minutes to separate any non-exfoliated BP; and then the same procedure will be
repeated at higher speeds to separate thicker layers (5 to 10 layers). In the next step, the
remaining floating substance will be centrifuged at higher speed for the exclusion of thin-
ner layers (1-7 layers). Finally, the samples will be cleaned by deionized water and will
be put on SiO_2 substrate [22].
This method benefits from the ability to produce large-scale exfoliation of few-layer BP
and it is also more controllable [22].

Experimental challenges

One of the main challenges in phosphorene synthesis is its stability in ambient condition
after preparation [23, 24]. Due to the high reactivity of phosphorene surface, the existence
of water vapor and oxygen in ambient condition will result in fast degradation of phos-
phorene. This leads to the formation of a mixture of oxide and phosphoric acid [9]. This
can drastically affect the properties of this structure and is one of the major challenges

for future applications of phosphorene. To overcome this problem, numerous researches have been conducted [23, 24] which are mostly based on sample encapsulation in a neutral material. For instance, few-layers of phosphorene can be passivated using encapsulation with multi-layer hexagonal boron nitride (BN) or aluminum oxide (Al_2O_3) [23, 24]. Although these methods were successful to some extent, but further studies are needed for establishment of a completely reliable method which can protect different properties of phosphorene.

1.2 Physical properties of phosphorene

The unique puckered structure of phosphorene crystal has led to anisotropy in many of its properties which have differentiated it from other 2D structures [9, 10]. In this section we will briefly review some of these special properties.

1.2.1 Electronic band structure of phosphorene

The electronic structure of BBP has been investigated from early 1950s[26]. According to these studies, BP has a direct and narrow band gap ranging from 0.3-0.35 eV [26–28]. Such narrow band gaps have limited its electronic applications. Therefore, till 2014, studies on this material were not very extensive. But immediately after FLP synthesis in
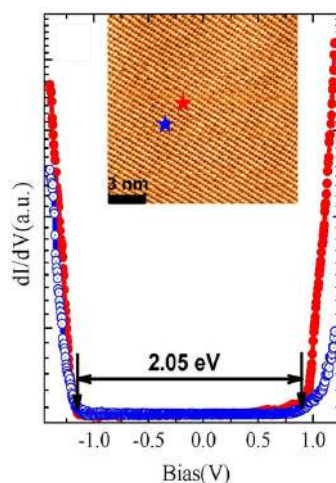
Figure 1.4: Scanning tunneling spectrum in log scale measured at two different locations on the surface of phosphorene as marked by red and blue stars on the figure inset [25]. The measurements gave a band gap of 2.05 eV for MLP. The picture has been taken from [25].

2014 [20, 21], as a new member in the family of 2D materials, extensive and more precise studies have been conducted on this structure. Within a short time, the electronic band properties of monolayer, few-layer and BBP were reported by several research groups both experimentally and theoretically [20, 25, 29–36].

Experimental band gap of phosphorene

Experimental measurements[25] have revealed that unlike its bulk counterpart, monolayer phosphorene has a relatively large band gap. Figure 1.4 represents the results of scanning tunneling spectroscopy (STS) for determination of the band gap of monolayer phosphorene (MLP). Based on this method, a typical tunneling spectrum which provides dI/dV as a function of biased voltage gives a good estimation of the band gap of MLP. These typical U-shaped spectra were measured in log scale at two different locations on a clean surface of phosphorene as marked by red and blue stars on the figure inset. The measurements revealed a band gap of ∼2.05 eV for this structure [25].

Theoretical results

Theoretical calculations have shown that density functional theory (DFT) within the local density approximation (LDA) and semi-local approximations are unable to correctly describe the semiconducting behavior of BBP [29, 31–33]. In other words, LDA and generalized gradient approximations (GGA) generally underestimate band gaps or even yield zero for this structure [29, 31–33].

To resolve this problem, the application of hybrid functionals which consider a non-local contribution for the exact exchange term has been relatively successful [30]. Three main classes of these approximations are PBE (Perdew-Burker-Ernzerhof), B3LYP (Becke-three parameter-Lee-Yang-Par) and HSE06 (Heyd-Scuseria-Ernzerhof) functionals. However, the results of these methods are strongly dependent on the mentioned factors and empirical parameters which determine the screening range and the contribution of exact exchange in the system [30]. On the other hand, having a correct estimation of vdW interactions between layers is crucial in DFT calculations [16]. In this regard, different considerations in the mentioned factors have resulted in a wide range of different results in band gap calculations for this structure.

Among them, the GW approximation results in more compatible and reliable outcomes for electronic properties of this system [29, 33, 35]. This approximation is based on the calculation of the electron self-energy in a many-body system which could be expressed as an expansion of the self-energy in terms of the one-particle Green's function G and the screened Coulomb interaction W. In this approximation, different terms are representative of approximation order. In Table 1.1, the calculated energy band gaps (in eV) at different

Table 1.1: Energy band gaps in unit of eV for monolayer ($n = 1$), few-layer ($n = 2, 3$), and BBP ($n = \infty$) at different levels of DFT and the TB model. The available experimental data are also listed. The table has been taken from [30].

	GW_0@GGA	TB Model	GW_0@HSE	G_0W_0@GGA	HSE	GGA	Expt.
$n = 1$	1.85	1.84	2.41	1.60	1.00–1.91	0.80–0.91	2.05
$n = 2$	1.16	1.15	1.66	1.01	1.23– 1.01	0.45–0.60	—
$n = 3$	0.84	0.85	1.20	0.68	0.73–0.98	0.20–0.40	—
$n = \infty$	0.35	0.40	0.58	0.10	0.18–0.39	0.00–0.15	0.31–0.35

levels of DFT, tight-binding (TB) model, and experimental measurements for MLP, few-layer and BBP are provided based on the number of phosphorene layers n [30]. Moreover, as an example, the electronic band structures of monolayer, 2-layer, 3-layer and BBP calculated with the PBEsol (PBE for solid state and surface systems) functional are shown in Figs. 1.5 [9]. These electronic band structures have interesting characteristics which will be pointed out in the following. As Figs. 1.5 (a)-(c) suggest, the band gap of monolayer and few-layer of phosphorene is located at the Γ point of the BZ. The electronic bands in the vicinity of the Fermi level and along the Γ-Y direction are quasi-flat; while along the Γ-X direction, they are almost linear. These features are more clear for the valence bands (VB) and as we will discuss later, this will result in anisotropy in many of electronic properties of this structure.

Another appealing property of this structure is that by increasing the number of layers, the above mentioned properties of bands remain unchanged and only a modification in the energy gap will be seen due to quantum confinement and vdW forces. Also, the direct
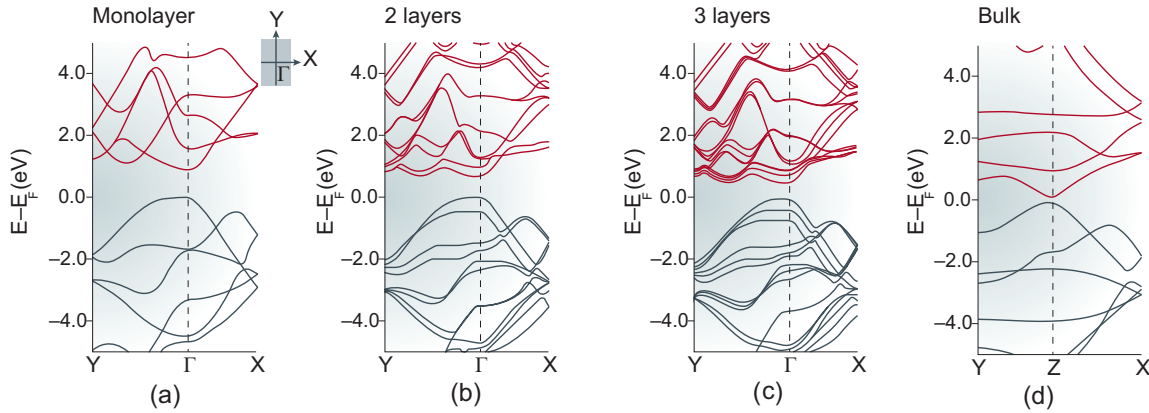
Figure 1.5: Band structures of (a) monolayer, (b) 2-layer, (c) 3-layer and (d) BBP calculated with the PBEsol functional [9]. The picture has been taken from [25].
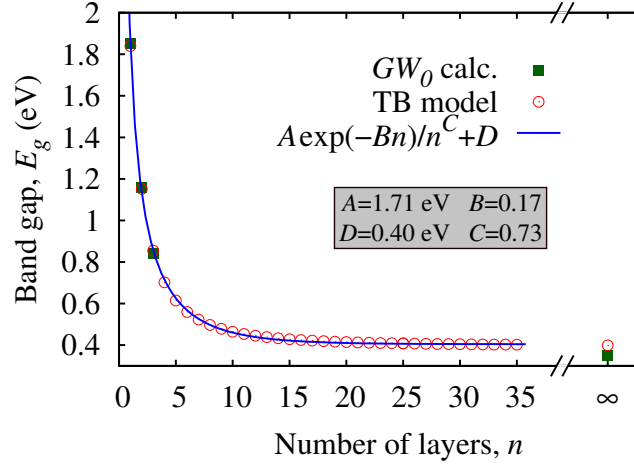
Figure 1.6: The energy gap of few-layer BP as a function of the number of layers using the GW_0 approximation and TB model. Taken from [30].

band gap of its monolayer remains direct for any number of layers and can be considered as one of the advantages of this structure in comparison with MoS_2.

According to theoretical and experimental data, the direct band gap ranges from 0.3 eV for bulk to 2 eV for MLP [30]. Figure 1.6 shows the energy gap of few-layer BP as a function of the number of layers using the GW_0 approximation and TB model [30]. As can be seen, the addition of one layer will result in a rapid decrease of the energy band gap which corresponds to a redshift of the photoluminescence spectra peaks [9]. Using the GW_0 approximation and the TB model [30], the band gap dependence on the number of layers can be fitted by the expression $E_{gap}^{(n)} = A\exp(-nB)/n^C + D$ where $A = 1.71$ eV, $B = 0.17$, $C = 0.73$, and $D = 0.40$ eV. Therefore, when $n \to \infty$, the band gap will reach $E_{gap}^{(\infty)} = 0.4$ eV which is very close to its experimentally value [30]. In fact, the variation of few-layer BP band gap has the fastest variation rate among the layered materials which have been studied so far which makes this structure very interesting [16].

To explain this feature, it must be mentioned that the interlayer coupling has a crucial role [37]. Investigation of differential charge density in few-layers of phosphorene (see Fig. 1.7) reveals that in the interlayer region a covalent-like characteristic is dominant which can be found using the charge reduction (shown by cold colors) near P atoms; while in the space between the two neighbor atoms of two adjacent layers, a charge accumulation (shown by warm colors) can be observed [16, 37]. A simpler explanation can be presented through molecular orbital analysis [16]. In this structure, each atom has four sp^3 hybridized orbitals, three of which form interalayer covalent bonds and the fourth orbital with one electron pair is almost perpendicular to the phosphorene plane [16]. This
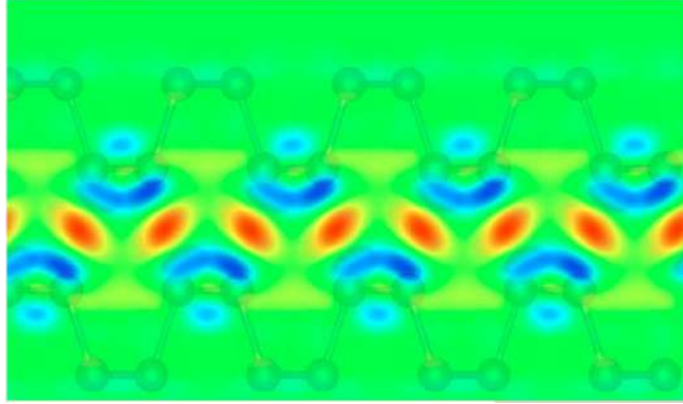
Figure 1.7: Differential charge density in the interlayer region of 6-layer phosphorene. Electronic charge density of the middle layer of 6-layer phosphorene obtained from the difference of three upper and lower layers from the total electron density. Warm colors represent charge accumulation while cold ones reflect decrease of charge around the atoms. Taken from [37].

results in a strong vdW absorption force between phosphorene layers which brings two phosphorene layers close enough so that the hybridized electron pairs of two adjacent P atoms are forced to hybridize, and form bonding and anti-bonding states [16]. These bonding states will result in a sort of covalent-like bond which leads to a fast band gap variation rate [16].

1.2.2 Optical properties

The anisotropy of phosphorene structure results in unique properties in its optical behavior which will be briefly reviewed in the following.

Phosphorene exhibits a drastic anisotropy in its optical absorption [16, 32]. In other words, one can see a dichroism in the optical absorption spectra [32], which means that this structure absorbs polarized light corresponding to the band gap along armchair direction while it is transparent along the zigzag direction [32]. The described anisotropy in the optical absorption is due to the underlying symmetries in the wave functions of valence and conductance bands which determine the type of dipole-allowed transitions [16]. Figure 1.8 (a) shows the schematic band structure of phosphorene near the Γ point which illustrates the dipole-allowed transitions obtained from symmetry considerations [38]. In this figure, P_i represents the ith component of momentum that enters in transitions where red and pink double arrows show dominant and non-negligible transitions, respectively [38], and the gray region is the forbidden band gap. As can be seen, along the $\Gamma - X$ direction, the dominant dipole transition has an energy which corresponds to the system band gap; while
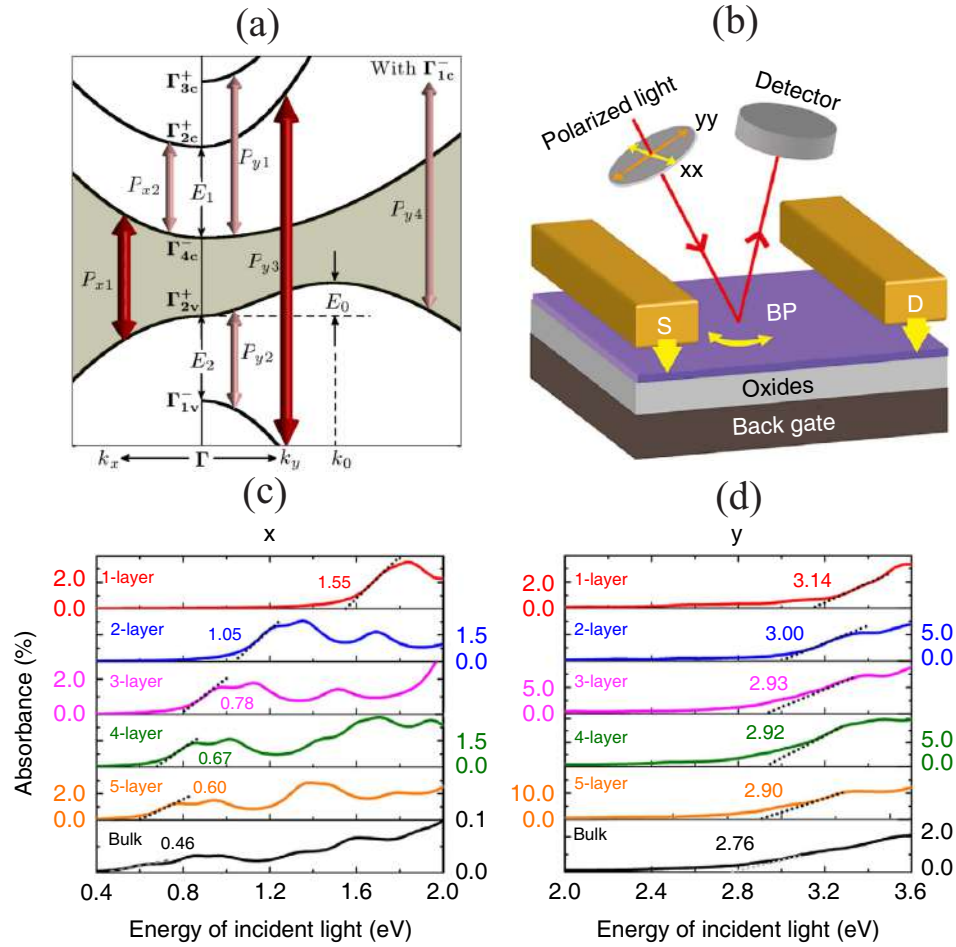
Figure 1.8: (a) Schematic band structure of phosphorene near the Γ point which illustrates dipole-allowed transitions using symmetry considerations (adapted from [38]). (b) Schematic representation of a proposed experimental geometry to use optical absorption spectroscopy to determine the crystallographic orientations in FLP. (c) and (d) Optical absorption spectra of few-layer and BBP due to perpendicular incident light which is linearly polarized along x and y directions, respectively. Figures (b), (c), and (d) have been taken from [32].

along the $\Gamma - Y$ direction, the dominant allowed transition energy is larger than the energy gap and results in transparency toward near-gap energies [38]. Since the optical absorption rate is proportional to the square of the matrix components of dipole transitions between states $|i>$ and $|f>$ [9], this feature manifest itself in optical absorption as well.

The described anisotropy in optical properties of phosphorene can be used to determine its crystallographic axes [32]. Figure 1.8 (b) is a representation of a proposed experimental geometry to use optical absorption spectroscopy to determine the crystallographic orientations in FLP [32]. It is expected that theoretically predicted optical absorption spectra shown in Figs. 1.8 (c) and (d) will be in good agreement with experimental results [32]. These figures show the optical absorption of few-layer and BBP due to the perpendicular incident of light which is linearly polarized along x and y directions, respectively. As seen along the x axis, the band edge (linear fitting) of the first absorption peak is found at the system energy gap which results in the fast reduction with the thickness of the sample [32]. But, along the y axis, the first band edge can be seen at 3.14 eV which is slightly shifted with increasing number of layers and finally, it reaches 2.76 eV for BBP.

1.2.3 Carrier mobility

It is evident that electronic properties of any structure is highly dependent on its carrier mobilities. Therefore, having a correct estimation of carrier mobilities is inevitable for a better understanding of these properties. In addition to the effective masses of electron and hole, there are two other more important factors that determine the carrier mobilities of FLP [32]. The first factor is deformation potential E_1 and the second one is elastic modulus C_{2D} along the propagation direction of the longitudinal acoustic wave [32].

Under experimental conditions, there are a variety of carrier scattering mechanisms such as phonon, impurity, and interface scatterings which can limit carrier mobilities [16]. Phonon scattering is intrinsic in ambient temperature and always exists. But the other factors can be controlled and their negative impacts can be minimized according to sample synthesis condition.

In a study [32], the phonon-limited scattering model was considered at T=300 K and charge carrier mobilities were calculated for monolayer and FLP. Table 1.2 presents the theoretically calculated amounts of these quantities for FLP. The predicted values for carrier mobilities are generally large and are in the range of several hundreds to several thousands of $cm^2V^{-1}s^{-1}$.

Regarding these data, it is clear that except for MLP, the hole mobilities are larger than the electron mobilities. On the other hand, due to the directional anisotropy, the system shows anisotropy in these values along x (armchair) and y (zigzag) directions; in a way that for electrons (holes) the values along x is four times (twice) the values along y [32]. However, the behavior for MLP is different to some extent. For electrons, the mobility along the x direction is about 14 times the value along y, which is similar to that of FLP. While, for holes, the behavior is completely different and their mobility along the x direction is about 16-38 times smaller than the values along y, that is $640 - 700cm^2V^{-1}s^{-1}$, compared with

Table 1.2: Theoretically calculated values of electron and hole masses, deformation potentials, Yang modulus, and carrier mobilities for monolayer and FLP along the x and y directions at 300 K. n denotes the number of layers. The table has been taken from [32].

Carrier type	n	m_x $\Gamma - X$	m_y $\Gamma - Y$	E_{1x} (eV)	E_{1y}	c_{x2D} (Jm^{-2})	c_{y2D}	μ_{x2D} $(10^3$cm^{2}V^{-1}s$^{-1})$	μ_{y2D}
	1	0.17	1.12	2.72	7.11	28.94	101.60	$1.10 - 1.14$	~ 0.08
	2	0.18	1.13	5.02	7.35	57.48	194.62	~ 0.60	0.140.16
Electron	3	0.16	1.15	5.85	7.63	85.86	287.20	$0.76 - 0.80$	$0.20 - 0.22$
	4	0.16	1.16	5.92	7.58	114.66	379.58	$0.96 - 1.08$	$0.26 - 0.30$
	5	0.15	1.18	5.79	7.35	146.58	479.82	$1.36 - 1.58$	$0.36 - 0.40$
	1	0.15	6.35	2.50	0.15	28.94	101.60	$0.64 - 0.70$	$10 - 26$
	2	0.15	1.81	2.45	1.63	57.48	194.62	$2.6 - 2.8$	$1.3 - 2.2$
Hole	3	0.15	1.12	2.49	2.24	85.86	287.20	$4.4 - 5.2$	$2.2 - 3.2$
	4	0.14	0.97	3.16	2.79	114.66	379.58	$4.4 - 5.2$	$2.6 - 3.2$
	5	0.14	0.89	3.40	2.97	146.58	479.82	$4.8 - 6.4$	$3.0 - 4.6$

$10,000 - 26,000$cm^{2}V^{-1}s^{-1} [32].

Such a larger mobility along the y direction occurs despite the rather high mass of holes ($6.35m_0$) along y [32]. This is due to deformation potential for MLP along y axis. As seen in Table 1.2, the value of deformation potential for holes in MLP along y axis is $\sim E_{1y} = 0.15$ eV, which is very small in comparison with its typical values for FLP and other structures such as graphene, MoS$_2$, and BN [32].

1.2.4   Excitons in phosphorene

Excitonic effects occur due to the attractive Coulomb interaction between electrons and holes. A larger exciton binding energy is expected for a system with stronger Coulomb interaction. It has been shown that in 2D materials, reduced screening of the Coulomb attraction and weak dielectric screening result in a drastic enhancement in the exciton binding energy [39]. In phosphorene, photoluminescence excitation spectroscopy revealed a quasi-particle bandgap of 2.2 eV, which leads to an estimation of $\sim$900 meV for exciton binding energy [40]. This measurement is consistent with theoretical results based on first principle calculations [40]. The experimental observation of highly anisotropic and bright excitons with large binding energy not only opens avenues for future explorations of many-electron physics in this unusual 2D material, but also suggests its promising future applications in optoelectronic devices [40].

1.2.5 Mechanical properties of MLP

One of the captivating features of the 2D family of materials is their high stretchability which provides the possibility of strain engineering [41]. Controlled strain engineering is an interesting pathway to tune the optical and electronic properties of these materials which give good grounds for the realization of straintronic devices that are engineered through the introduction of mechanical deformations [41].

Owing to the puckered structure of phosphorene, it demonstrates superior flexibility with an order of magnitude smaller Young's modulus in comparison with other 2D materials [42]. Also, unlike graphene and MoS_2, the Young's modulus in phosphorene shows an anisotropic behavior and depends on the direction [42]. For example, the Young's modulus for graphene, MoS_2, and BN, are 1.0 TPa, 0.33 TPa, and 0.25 TPa, respectively, compared to 0.166 TPa (zigzag) and 0.044 TPa (armchair) for phosphorene [42]. As a result, MLP can sustain strain very well specially in the zigzag direction up to about 30% [42]. This makes phosphorene promising for possible applications using strain engineering.

Another interesting mechanical behavior of phosphorene is its negative poisson's ratio along the perpendicular direction [43]. This means that tensile strain along a specific direction inside the plane will result in the expansion of BP in the z direction. This unusual property has been reported for the first time in a 2D structure [43].

The role of uniaxial and biaxial strain in manipulating the electronic structure of FLP has been investigated via DFT [44–46] and TB approaches [47–49]. Applying tensile or compressive strain in different directions results in different modifications of the electronic bands. One can observe a direct to indirect gap transition, or a prior direct band gap closing, depending on the type of applied strain [45, 46, 50].

1.3 Topological properties of phosphorene

An important goal that is pursued by condensed matter physicists is the classification of the states of matters and identifying their phases. Before 1980, most of our understanding in this field rested on Landau's paradigm that classifies the states of matters by order parameters and the concept of spontaneously broken symmetry [51]. Subsequently a new way of classifying the states of matter based on the mathematical notion of topology was created. In fact, that was the early days that the mathematical concept of topology became relevant in condensed matter physics. This new class is beyond Landau's theory, which classifies the phases of a matter by topological order parameters instead of an ordinary order parameter [52–55]. That progress was seen as a big boost to material science, and it led to awarding the 2016 Nobel prize in physics to David J. Thouless, F. Duncan M. Haldane, and J. Michael Kosterlitz for the theoretical discovery of topological phase transitions and

topological phases of matters.

In a topological phase, the states are topologically protected in the sense that there exists a certain invariant quantity which does not change easily with smooth deformations of the physical parameters of the system. Indeed, this manner of classification of materials is one of the hallmarks in condensed matter physics, as it provides a new way to discovery and better understanding many phenomena in material science, and actually can smooth the path toward future applications.

The integer quantum Hall effect (IQHE), discovered in 1980 [52] is the first example of a topologically non-trivial quantum state of matter which is induced by a perpendicular magnetic field [56]. In this effect, the topological invariant is the number of filled Landau levels (LLs) which is independent of material details [56]. Over the past two decades, condensed matter theorists realized that the QHE is just one member of a very larger family of topologically non-trivial quantum states known as topological insulators (TIs) [56]. Some examples of this family are the quantum spin Hall (QSH) effect which occurs in a 2D material [57, 58], (3D) TIs [59], topological crystalline insulators (TCIs) [60], and recently identified new class of TIs known as higher order topological insulators (HOTIs) [61]. This relatively new field of research is of great importance not only from a practical point of view, but because of its role in clarifying fundamental properties of matter. Mele, one of the pioneers in this field says that "although topological insulators may improve technology, they're even more important as a tool for probing quantum electronic properties, and hence elucidating fundamental properties of matter itself" [62].

As stated before, the strong anisotropy in the crystal structure of phosphorene results in highly anisotropic electrical, thermal, and optical properties. This provides a new playground for investigating topological properties in this structure that may show distinct characteristics. In what follows, we proceed by giving a brief introduction of the topological properties of monolayer and FLP.

1.3.1 Quantum Hall effect in phosphorene

The quest for samples with higher mobility has motivated the researchers to investigate the QHE as a prototypical 2D phenomenon in monolayer and few-layer of phosphorene [63]. The LLs and the QHE has been studied both theoretically and experimentally in few-layer BP [63–73]. The scaling of cyclotron gap in magnetic field B depends on the behavior of band structure [74]. For example, it was shown that in a system with linear-quadratic spectrum, the dependence of LLs on the magnetic field is neither linear in the conventional limit nor as $(nB)^{1/2}$ in the Dirac limit [68, 74]. For such a dispersion, the LL energies scale as $[(n + 1/2)B]^{3/2}$ where n is the LL index [68, 74]. The highly anisotropic physics in many properties of phosphorene are closely related to its band structure which is Dirac-

like in one direction and Schrödinger like in the other direction [44, 72, 75, 76]. Therefore, one might expect to observe a behavior as $B^{2/3}$ in the Landau-level energies. But, there exist other theories arguing that such behavior is not correct [63, 69–71, 73]. Within the framework of the effective $k \cdot p$ Hamiltonian and TB model, they have shown that LLs in phosphorene behave like conventional semiconductor 2D electron gases [69–71, 73] which results in an the usual QHE. It has been also argued that the emergence of the mentioned LLs field dependence can be observed in the presence of large strain or electric field [44, 71]. However, due to the mentioned highly anisotropic electronic structure, determining the LLs field dependence is still under theoretical debate.
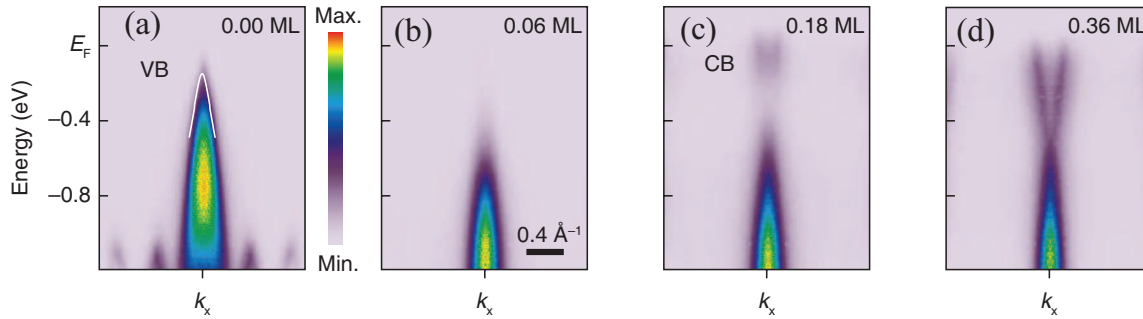
Figure 1.9: (a)-(d) Experimental dispersions for K-doped BP films taken at 15K near E_F along k_x. The density of dopants is shown at the upper right of each panel. Taken from [77].
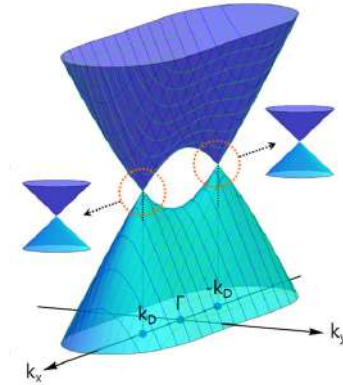
Figure 1.10: Calculated conduction and valence bands of K-doped 4-layer phosphorene beyond the critical dopant density N_c. Taken from [78].

1.3.2   Topological phase transitions in phosphorene

There exist several works pertinent to the observation of different phases in bulk and mul-
tilayer BP by tuning the lowest energy bands [46, 77–85]. For instance, it was shown that
using an in situ surface doping technique one can tune the band gap in few-layer BP [77].
This report demonstrates that potassium atoms as dopant induce a strong electric field due
to the giant Stark effect [77]. As a result, the vertical induced electric field modulates the
band gap of few-layer BP and eventually gives rise to a band-inverted semimetal which
is Dirac-like in armchair and Schrödinger like in zigzag directions [77]. Figures 1.9 (a)-
(d) show the experimental dispersions of K-doped BP films taken at 15K near E_F along
k_x for some dopant densities [77]. As seen, at the critical density $N_c = 0.36$ monolayer
(ML), a band inversion occurs, giving rise to a semimetal phase [77]. In addition, first-
principle calculations showed [78] that beyond this critical dopant density, 2D massless
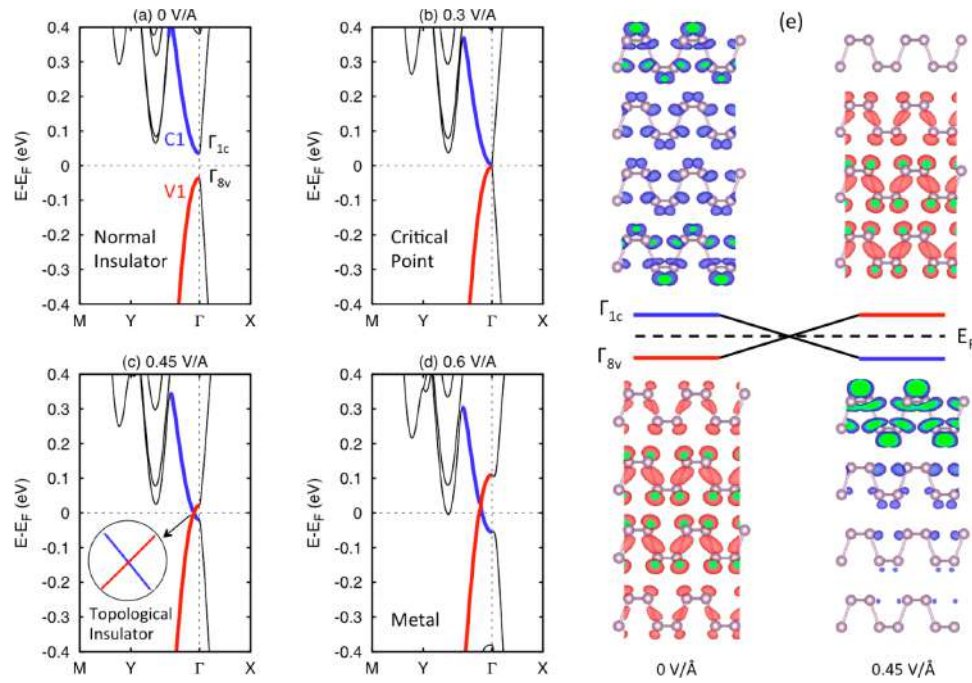
Figure 1.11: Calculated band structures of 4-layer BP for applied electric field of (a) 0 V/Å, (b)
0.3 V/Å, (c) 0.45 V/Å, and (d) 0.6V/Å. (e) The schematic diagram of the mechanism of band
inversion for energy levels Γ_{1c} and Γ_{8v} and the corresponding magnitude of squared wavefunction
of 4-layer BP. Taken from [79].
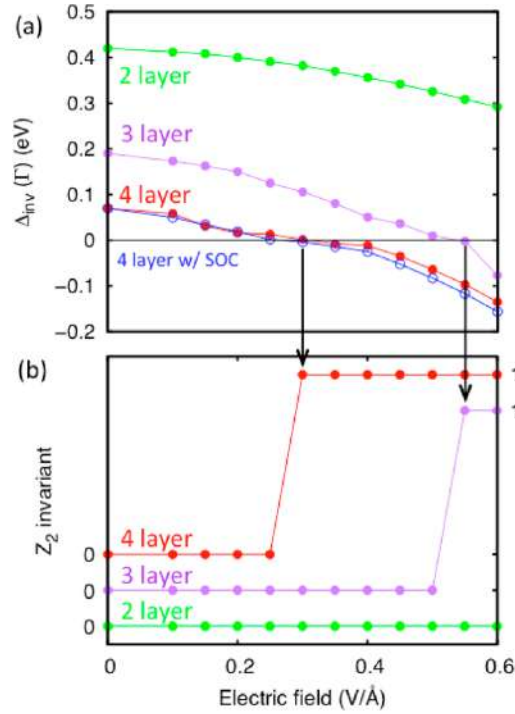
Figure 1.12: (a) The inversion energy Δ_{inv} as a function of applied electric field. (b) Calculation of the $\mathbb{Z}_2$ invariant as a function of applied electric field. Taken from [79].

Dirac Fermions appear in all momentum directions as shown in Fig. 1.10.

The sensitivity of the energy gap to the number of layers and external perturbations make this material a potential candidate for the investigation of various electronic phases. For example, the possibility of converting FLP from a normal insulator to a topological phase using external factors such as strain, electric field, and optical pumping has been explored [46, 79, 82, 85].

Using DFT calculations it was shown that a thin film of phosphorene experiences a phase transition from the normal insulator (NI) to a TI and then to a topological metal (TM) by applying a perpendicular electric field [79]. In this system, the mechanism of band inversion is entirely explained by the applied electric field rather than by spin-orbit coupling (SOC) [79]. Figures 1.11 (a)-(d) show the band structures of 4-layer phosphorene for applied perpendicular electric field of (a) 0 V/Å, (b) 0.3 V/Å, (c) 0.45 V/Å, and (d) 0.6V/Å [79]. A schematic diagram of the mechanism of band inversion for energy levels Γ_{1c} and Γ_{8v} and the corresponding magnitude of squared wavefunctions are illustrated in

Fig. 1.11 (e) [79]. Here, the inversion energy at Γ point is defined as $\Delta_{\mathrm{inv}} = \Gamma_{1c} - \Gamma_{8v}$ [79]. Figure 1.12 (a) shows the inversion energy Δ_{inv} as a function of applied electric field for 2-, 3-, and 4-layer BP. As seen, by increasing the applied electric field, inversion energies decrease monotonically and at a critical field the energy gaps become zero [79]. Further increasing the field makes the inversion energies negative which correspond to the change in the symmetries of the shown wavefunctions. The negative inversion energies which monitor the band inversion are signatures for the existence of nontrivial topological phases. For 4-layer phosphorene, including the SOC induces a band gap of $\sim$5meV and at the critical field of $\sim$0.30 V/Å the material converts to a TI [79]. This topological phase transition has been confirmed using the $\mathbb{Z}_2$ formalism [79] as shown in Fig. 1.12 (b).

Further increasing the electric field to 0.6V/Å leads to the downward shift of another valley of conduction bands as shown in Fig. 1.11 (d) and thus the system becomes metallic [79]. Since the nature of band inversion does not change, the system converts to a topological metal [79].

In a different DFT study [46] such phase transitions for various stacked bilayer phosphorene under in-plane strain has been explored. The study has reported a strain-induced topological phase transition from a trivial to QSH state in bilayer phosphorene, accompanied by band-inversion that changes the $\mathbb{Z}_2$ invariant from 0 to 1, which is highly dependent on interlayer stacking [46].

1.3.3   Phosphorene as a higher-order TI

Recently a distinctive new family of topological materials has been added to the conventional TIs [61, 86–88]. These materials are called higher-order topological insulators (HOTIs) and are an extended notion of the conventional TIs [88]. They are called topologically higher-order because the conventional bulk-boundary correspondence is no longer applicable for characterizing their topological features [61, 88]. An nth order d-dimensional TI is topological because unlike those of conventional TIs does not have gapless edge states at $d-1$ boundaries. Instead, it has $(d-n)$-dimensional boundary states. For example, in two dimensions, a second-order TI exhibits gapless corner states which is a manifestation of nontrivial topology in the bulk [61, 88].

In a recently published paper [88] M. Ezawa predicted that MLP is indeed a perturbed second-order Wannier-type HOTI. It has been shown that the topological corner states will appear in the rhombus structure of phosphorene near the Fermi energy around -0.16 eV as shown in Fig. 1.13 [88].
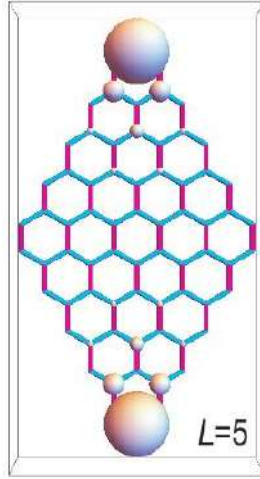
Figure 1.13: The square root of the local density of states for a rhombus structure of MLP. Taken from [88].

1.4 Structure of the thesis

The existence of the previously reviewed unusual properties of monolayer and FLP necessitate further research on phosphorene and phosphorene nanostructures. This motivated us to dedicate the present thesis on the study of some electronic properties of this material. In this doctoral thesis, within the framework of TB model, we investigate the electronic properties of phosphorene and phosphorene nanoribbons (PNRs) mainly from the topological point of view. For this rather new emerged 2D material, analyzing the band structure, the characterization of the electronic states, the electronic transport of phosphorene zigzag and armchair nanoribbons, and the scaling laws of the band gaps versus ribbon width are interesting subjects that we will deal with. Investigation of the LLs field dependence in this 2D material which determines the behavior of corresponding QHE as a topological phenomenon, is another subject of this work. Using the TB approximation with inclusion of the spin-orbit interaction, we also investigate the possible topological phase transition in the electronic band structure of phosphorene in the presence of axial strains.

The thesis is organized as follows: In chapter 2, we will briefly review the main aspects of the QHEs as purely topological phenomena. The different types of field dependence Landau levels (LLs) and their consequences in the QHE will be discussed. This chapter will give the reader the basic knowledge to treat the QHE and the LLs field dependence in phosphorene as a highly anisotropic system.

In chapter 3, a short overview of the physics behind topological band insulators with time-reversal symmetry will be given. Next, we will proceed by giving a brief overview of

the ways to distinguish a TI from a NI. Then, we will introduce an efficient algorithm for lattice computation of the $\mathbb{Z}_2$ invariant which provides a numerical method to quantitatively distinguish a TI from a NI. The experimental signatures of 2D and 3D TIs will be addressed at the end of this chapter.

In chapter 4, we start by introducing the TB model of MLP. The band structure and effective masses of MLP near the gap are presented based on the TB model, and it is shown that the dispersion is relativistic along the armchair direction and the corresponding Fermi velocities will be calculated. Then, numerical data for this model are presented for zigzag phosphorene nanoribbons (zPNRs) and armchair phosphorene nanoribbons (aPNRs), and the emergence of flat bands in zPNRs are discussed. The scaling behavior of band gaps with ribbon width is presented and the obtained results are compared with those of the other methods. In addition, the effect of transverse electric field on the band gap in aPNRs and the transistor effect in zPNRs are investigated.

In chapter 5, the behavior of MLP in the presence of a perpendicular magnetic field which breaks the time-reversal symmetry is discussed. The behavior of the system in the QH regime is in close relation with the characteristics of LLs. The primary goal of this chapter is to address the debating field dependence of LLs in MLP. Using a simple approach, we will demonstrate that the LLs dependence on magnetic field is indeed as for conventional 2D semiconductor electron gases. We show that the results are valid up to very high field regime. Then, we will discuss the conditions for which such a dependence can continuously evolve into another field dependences.

In chapter 6, the effective low-energy TB model Hamiltonian including the SOC terms for MLP is obtained. Then, we will study the effect of axial strains on the band structure produced by this model and our results are compared with DFT results. Demonstration of a topological phase transition in the electronic properties of phosphorene when particular types of strain are applied and the characteristics of corresponding edge states in zPNRs are presented in the final part of this chapter.

Finally, a summary of the thesis is given in chapter 7.

CHAPTER 2

Chern insulators

Today's knowledge about topological quantum matter was first encountered around 1980 with the experimental observation of the integer [52] and then fractional [53] quantum Hall effects (IQHE and FQHE). In order to realize these effects, the key is to break time-reversal symmetry (TRS). This can be done by applying strong magnetic fields to a 2D electron gas at low temperatures.Though, the most important application the QHE is to provide very precise standards in the field of metrology [89], a topological approach to treat this phenomenon is very useful for a better understanding of the issue of topological insulators (TIs).

Herein, we concentrate on broken TRS systems, and the goal is to provide a succinct background which opens the way toward understanding the subject of TIs.

In what follows, we will briefly discuss the main aspects of the QHEs as purely topological phenomena and introduce the different types of field dependence Landau levels (LLs) and their consequences for the QHE. An outstanding question that may arise here is the functional dependence of Landau level (LL) gaps of phosphorene on magnetic field that we will answer in chapter 5. Then, we will end the chapter with the answer to the question how one can define a relevant topological quantity to identify the topology of a system with broken TRS. To this end, we will introduce an efficient method for computing this relevant topological invariant, the so-called first Chern number in a discretized BZ [90] which is very useful for complicated band structures.

2.1   Quantum Hall effects

One of the most beautiful physical phenomena in the area of condensed matter physics is the QHE. The phenomenon takes place in a very thin layer of electron gas in the presence of a very high magnetic field when the system is cooled down near absolute zero. It was discovered [52] that the values of the Hall resistivity are independent of all the macroscopic details such as size, shape of the sample, what it is made of, and what kind of impurities are present in the system. Applying a certain current through the sample leads to the Hall voltage V_H so that the ratio of V_H/I is a universal value [52]. This ratio is called the quantized Hall resistivity and the phenomenon is known as IQHE. Such a completely universal and fundamental phenomenon which occurs in a dirty, not very perfect, and human-made system, was a big surprise especially from the experimental point of view.

Then, there was a second big surprise: in this system, one can see fractional quantum numbers [53] under special circumstances where electron interactions are important. This phenomenon, which is called FQHE was first explained theoretically by Laughlin [55] using an incompressible quantum state which originates from the strong correlation between the position of the electrons. These attempts led to a huge advancement in the theoretical understanding of the mechanism that a large system of interacting electrons form their rather complex ground states [91].

Further progress after that, led to the realization that these complicated quantum states may contain some types of quantum vortices that are flowing around each other [92, 93], and researchers realized that they could be used to form quantum bits. These objects are topologically protected and thus, are not destroyed by usual perturbations in the system. Therefore, it would be a promising candidate for quantum computers called topological quantum computers [94]. This theory [94] uses these objects and braids them around to do an operation [92, 93]. As mentioned above, the most important reason for using this idea is that quantum systems are very sensitive to small perturbations, noises and imperfections; but this particular type of state is very robust against these factors [92, 93]. For example, if we make a local perturbation at any spot in the system, nothing happens to the quantum state and no local perturbation can destroy that information. So, the hope is that they would be very robust against quantum decoherence, and make them great candidates for application in quantum computing [92, 93].

Since the physics behind the QHE is very important to better understand the subject of TIs, in the following, we will briefly discuss the main properties of the phenomenon.

2.1.1   Integer quantum Hall effect

In the classical picture, to drive current through an ordinary piece of metal sheet, one needs to apply an electric field to push electrons along the sample. This requires having a volt-
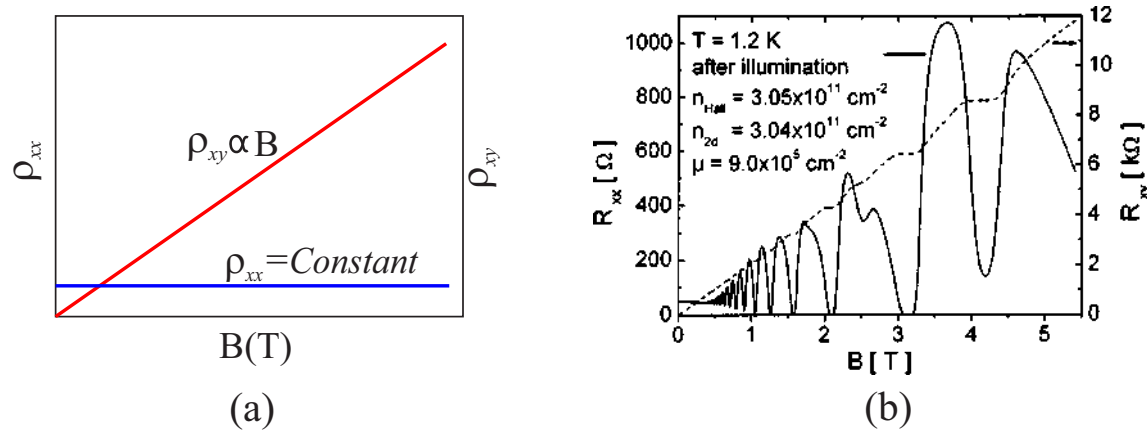
Figure 2.1: (a) The classical Hall resistivity ρ_{xy} and the longitudinal resistivity ρ_{xx} as a function of the applied magnetic field B. (b) The experimental measured Hall and longitudinal resistance, ρ_{xx} and ρ_{xy} as a function of magnetic filed B in a GaAs/Al$_x$Ga$_{1-x}$ heterostructure. Adapted from [95].

age drop along the metal sheet, and the electric field points in the direction the current I is flowing. Edwin Hall discovered that if we apply a strong magnetic field perpendicular to the direction of current flow and the plane of the sheet, the electrons would get pushed sideways by the Lorentz force. Therefore, a voltage drop V_H appears at right angles to the current direction. This voltage is proportional to the applied magnetic field B, and thus the Hall resistivity $\rho_{xy} = V_H/I$ is expected to be linearly proportional to B. The longitudinal resistivity ρ_{xx} is independent of the applied magnetic field. The behaviors of the classical Hall resistivity ρ_{xy} and the longitudinal resistivity ρ_{xx} as a function of the applied magnetic field are shown in Fig. 2.1 (a). This classical phenomenon has a number of practical uses such as Hall sensors.

Now, if we have a two dimensional (2D) sample of high mobility electron gas that is cooled down near absolute zero, one can see from Fig. 2.1 (b) that it starts to deviate from the Drude model in both the Hall and the longitudinal resistance. The figure shows a typical experimental measured Hall and longitudinal resistances, ρ_{xx} and ρ_{xy} as a function of magnetic filed in an inverted selectively doped GaAs/Al$_x$Ga$_{1-x}$ heterostructures fabricated by molecular-beam epitaxy [95]. As seen, the Hall resistance starts to develop plateaus, and the longitudinal one drops down and starts to show a series of drastic oscillations, which are the signature of what is called the quantized Hall effect. This means that by varying the strength of the magnetic field, the system experiences a phase transition from a metal to an insulator, then another metal to the other insulator, and so forth. An important feature here is that the Hall resistance seems to favor certain magical values where the magnetic field alters in a series of special intervals. This feature was first observed by von

Klitzing [52] and he immediately deduced the formula of $\rho_{xy} = h/ne^2$ to describe this behaviour. This phenomenon which is called IQHE led to his Nobel prize in 1985 for the recognition of this steps in the unit of the ratio of fundamental constants h and e^2.

The IQHE can be understood in the frame of a one-electron picture [96]. The physics behind the mentioned insulating phases and the corresponding quantized Hall conductances is the formation of Landau levels (LLs) [96]. The quantum mechanical treatment of a 2D electron gas in the presence of magnetic fields gives rise to the explanation of LLs formation. In a 2D lattice, electrons or holes feel the periodic potential of the lattice that gives rise to the formation of energy bands. Therefore, the field dependent LLs and thus the corresponding quantized Hall conductances may show different behaviors. Hence, in what follows we briefly introduce the various types of field dependent LLs and the corresponding Hall conductances which are important from both the theoretical and experimental points of view.

2.1.2   Conventional QHE

Consider a sample of electrons that are free to move in only a 2D plane. When these electrons are subjected to a strong perpendicular magnetic field B, their continuous energy spectrum

$$E(k) = \frac{\hbar^2}{2m_0}k^2, \tag{2.1}$$

is transformed into discrete LLs [96] as

$$E_n(k) = \hbar\omega_c(n + \frac{1}{2}), \qquad n = 0, 1, 2, ... \tag{2.2}$$

where the latter spectrum is a bunch of equidistant flat bands and each level is highly degenerate (see Fig. 2.2). In the above equations m_0 and k, are electron mass and the magnitude of in-plane wave vector $\boldsymbol{k}$, respectively, and $\omega_c = eB/m_0$ is the cyclotron frequency. In absence of disorder or phonon scattering, the corresponding density of states (DOS) of this spectrum is a series of delta functions

$$D(E_n) = \sum_n \delta(E - E_n). \tag{2.3}$$

However, disorders are ubiquitous in any sample of 2D electron gas (2DEG). For weak disorders that are small compared to the splitting of LLs, perturbation theory can be applied. Including such perturbations as random potentials in the corresponding Hamiltonian of the system decrease its symmetries and leads to the lifting of the degeneracies. Thus, the mentioned levels of DOS broaden to give extended and localized states [96] as shown
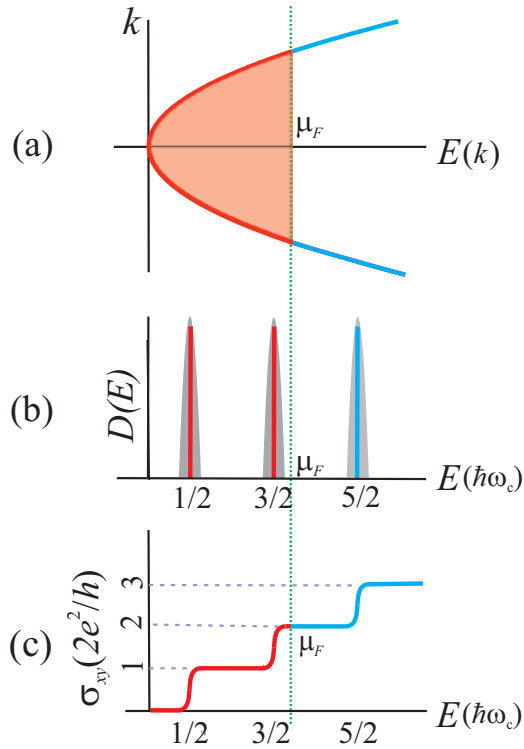
Figure 2.2: (a) Schematic energy spectrum of a 2DEG. (b) The discretized levels of DOS in Eq. (2.3) broadened to give extended and localized states. (c) The corresponding Hall conductivity as a function of the chemical potential.

in Fig. 2.2(b). The one-particle states near the exact energy levels $(n + 1/2)\hbar\omega_c$ are extended because they spread throughout the whole system and contribute to conductivity. In contrast, the one-particle states in the LL tails are localized because they cannot contribute to conductivity [91, 97]. The corresponding Hall conductivity of this 2DEG is shown in Fig. 2.2 (c). As seen, when the chemical potential lies between Landau level centers, the Hall conductivity is exactly quantized as $\sigma_{xy} = n2e^2/h$ where n is the number of filled LLs [97]. One can also see that, when the chemical potential moves through the corresponding energy of current carrying states, a transition from a plateau to the other occurs [97]. This is because the population of these current carrying states is changed.

2.1.3 QHE in an usual 2D semiconductor

In the preceding subsection, we consider the case of free electrons where no lattice potential is considered. In a 2D lattice, electrons or holes suffer from the periodic potential of

the lattice that gives rise to the formation of energy bands. Based on the effective mass theory [98], in an usual semiconductor with parabolic low-energy electronic spectrum, the effect of lattice potential can be fed into an effective mass. Then, one can use the free electron model by replacing the electron mass m_0 with the effective mass m. In most cases, this approximation is sufficient to describe the low-energy properties of the system. Since the electron-hole symmetry is generally absent in semiconductors (see Fig. 2.3 (a)), on can write the energy of electrons and holes in the vicinity of the conduction band minimum
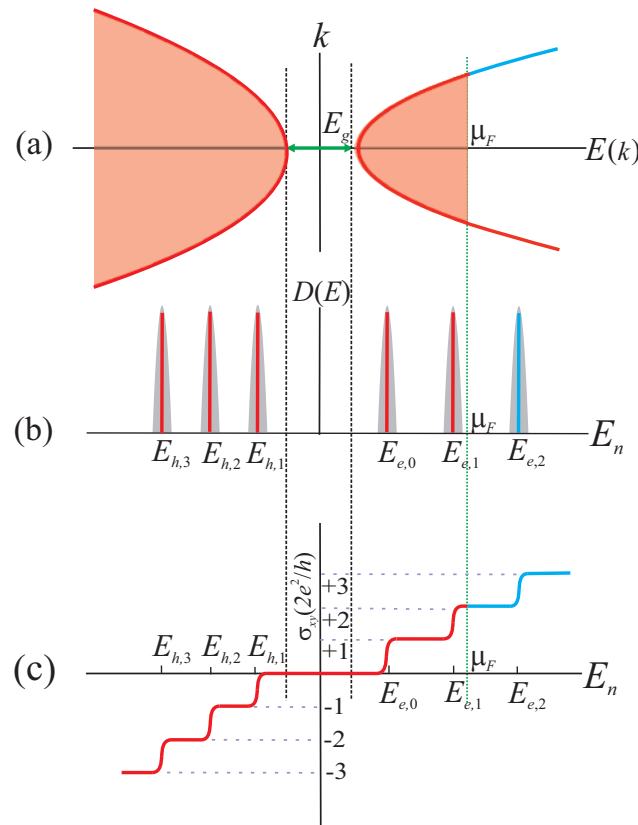
Figure 2.3: (a) Schematic of low-energy band structure for an usual semiconductor without electron-hole symmetry. (b) DOS of an usual semiconductor without electron-hole symmetry in the presence of a strong magnetic field and weak disorders. The two sets of LLs have different cyclotron frequencies due to the lack of electron-hole symmetry. (c) The corresponding Hall conductivity as a function of the chemical potential. There are two sets of equidistant ladder of quantum Hall plateaus with different lengths due to the different cyclotron frequencies ω_c^e, and ω_c^h.

(CBM) and the valence band maximum (VBM) as

$$
\begin{aligned}
E_e(k) &= \quad \frac{E_g}{2} + \frac{\hbar^2}{2m_e}k^2, \\
E_h(k) &= \quad -\frac{E_g}{2} - \frac{\hbar^2}{2m_h}k^2,
\end{aligned}
\tag{2.4}
$$

where m_e (m_h) is the effective mass of electron (hole) and E_g is the electronic energy gap of the semiconductor.

Now, we consider the case that a strong magnetic field is present in the system. Again, a simple quantum mechanical treatment as in the case of free electron model gives rise to the LLs as

$$
\begin{aligned}
E_{e,n}(k) &= \quad \frac{E_g}{2} + \hbar\omega_c^e(n + \frac{1}{2}), \quad n = 0, 1, 2, ..., \\
E_{h,n}(k) &= \quad -\frac{E_g}{2} - \hbar\omega_c^h(n + \frac{1}{2}), \quad n = 1, 2, ...,
\end{aligned}
\tag{2.5}
$$

where $\omega_c^e = eB/m_e$ and $\omega_c^h = eB/m_h$ are cyclotron frequencies of electrons and holes, respectively. The obtained sets of LLs are separated by the energy gap of E_g as shown in Fig. 2.3 (b). As seen, these two sets of LLs have different cyclotron frequencies due to the lack of electron-hole symmetry. As shown in Fig. 2.3 (c), this leads to two sets of equidistant ladders of quantum Hall plateaus with different lengths as a result of the mentioned different cyclotron frequencies. The quantized values of the Hall conductivity are again $\sigma_{xy} = \pm n e^2/\hbar$.

2.1.4 QHE in monolayer graphene

Graphene is the most famous allotrope of carbon. It consists of a single layer of carbon atoms forming a honeycomb lattice. The corresponding lattice constants and the unit cell of graphene are shown in Fig. 2.4. Each unit cell includes two carbon atoms that belong to the A and B sub-lattices, respectively. We choose nearest neighbor vectors $\boldsymbol{\delta}_1 = a(-\sqrt{3}/2, 1/2)$, $\boldsymbol{\delta}_2 = a(\sqrt{3}/2, 1/2)$, and $\boldsymbol{\delta}_3 = a(0, -1)$, to define the translation vectors as $\boldsymbol{a}_1 = \boldsymbol{\delta}_1 - \boldsymbol{\delta}_3$, and $\boldsymbol{a}_2 = \boldsymbol{\delta}_2 - \boldsymbol{\delta}_3$. The corresponding reciprocal lattice vectors are given by $\boldsymbol{b}_1 = 2\pi/3a(\sqrt{3}, 1)$, and $\boldsymbol{b}_2 = 2\pi/3a(-\sqrt{3}, 1)$. Some special points with high symmetry in the BZ are shown with the wave vectors $\mathbf{K'} = 4\pi/3\sqrt{3}a(1, 0)$, $\mathbf{K} = 2\pi/3a(1/\sqrt{3}, 1)$, and $\mathbf{M} = \pi/3a(\sqrt{3}, 1)$.

The symmetry of the hexagonal lattice of graphene is a key element for determining many of the unusual electronic properties not seen in conventional materials [99]. One of the most important features is its linear energy dispersion in the vicinity of K and K′ in
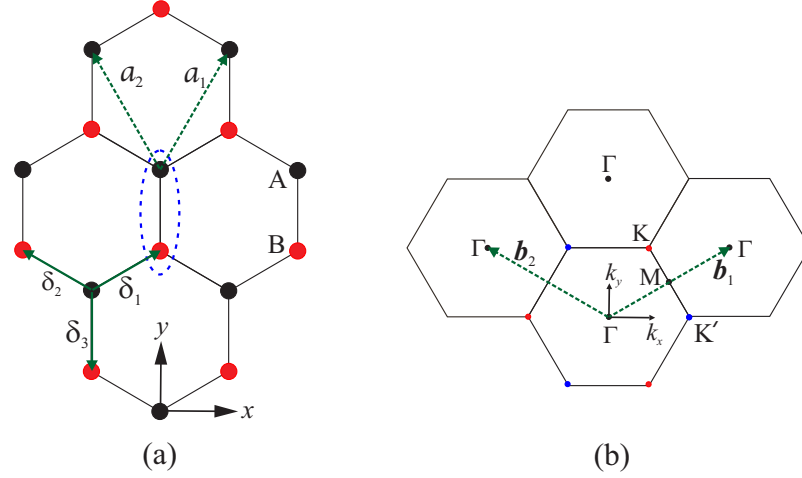
Figure 2.4: (a) The honeycomb lattice of graphene with a two-atom basis A (black symbols) and B (red symbols). Also shown are the basis vectors $\boldsymbol{a}_{1,2}$, and the space vectors $\boldsymbol{\delta}_{1,2,3}$. (b) The corresponding reciprocal lattice of graphene. Also shown are reciprocal lattice vectors $\boldsymbol{b}_{1,2}$ and high symmetry points in the BZ.

which many of graphene's properties have origin in it [3]. This implies that the masses of the formed 2D electron and hole gas are hidden by their interaction with the lattice of graphene. In other words, electrons and holes in graphene mimic relativistic particles in which their behaviors are determined by the Dirac equation [3]. Therefore, the experimental discovery of graphene [1] paved the ground to test some relativistic effects in the realm of condensed matter physics.

The experimentally observed QHE in monolayer graphene [100] shows a quite different unconventional character which was a striking phenomenon that is a manifest demonstration of the relativistic character of charge mobility carriers. Let us briefly discuss the influence of a strong magnetic field on the electronic properties of graphene.

As we will discuss in Sec 3.2.2, the nearest-neighbor TB approximation of graphene provides a very good description for its low-energy bands [3]. By expanding the elements of the TB Hamiltonian 3.8 around the K or K$'$ points, one can rewrite it as [3]

$$H_{\text{K,K}'}(k) = \hbar v_F \begin{pmatrix} 0 & k_x \mp ik_y \\ k_x \pm ik_y & 0 \end{pmatrix}, \tag{2.6}$$

where $v_F \approx 10^6 m/s$ is the Fermi velocity of Dirac fermions, and k is the distance to the valley points K or K$'$. This gives rise to the low-energy spectrum [3]

$$E(k) = \pm \hbar v_F k, \tag{2.7}$$
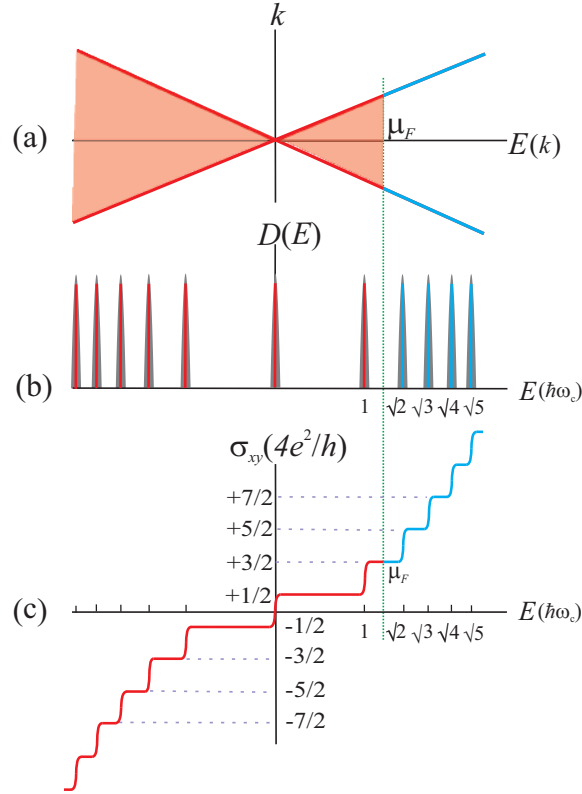
Figure 2.5: (a) Schematic view of the low-energy band dispersion of monolayer graphene. (b) DOS of graphene in the presence of a strong magnetic field and weak disorder. (c) The corresponding Hall conductivity as a function of the chemical potential.

as shown schematically in Fig. 2.5 (a).

Now, let us consider the effect of applying a uniform perpendicular magnetic field to the plane of monolayer graphene. Using the Landau gauge $\mathbf{A} = (0, Bx, 0)$, and the substitution $k_y \to k_y + \ell_B^{-2}x$, where $\ell_B = eB/\hbar$ is the magnetic length, one has to solve the Dirac-like equations [3]

$$\hbar v_F \begin{pmatrix} 0 & k_x \mp i k_y + \ell_B^{-2}x \\ k_x \pm i k_y + \ell_B^{-2}x & 0 \end{pmatrix} \begin{pmatrix} \psi_{\mathrm{A}} \\ \psi_{\mathrm{B}} \end{pmatrix} = E \begin{pmatrix} \psi_{\mathrm{A}} \\ \psi_{\mathrm{B}} \end{pmatrix} \qquad (2.8)$$

to obtain the energy spectrum of the system. Solving this equation gives the spectrum as [3]

$$E_{n,\pm} = \pm \hbar \omega_c \sqrt{n}, \quad n = 0, 1, 2, \cdots, \qquad (2.9)$$

which is exactly the same as the well known relativistic LLs [101].

The corresponding DOS of this spectrum is shown in Fig. 2.5 (b) . One can see an im-

portant difference compared to the case of conventional QHE, where there exists a zero energy mode which is related to both electron and hole excitations [102]. This led to the theoretical prediction [103] and then the experimental observation [104, 105] of the unconventional form of the quantized Hall conductivity

$$\sigma_{xy} = \pm(n + \frac{1}{2})\frac{4e^2}{h}, \quad n = 0, 1, 2, \cdots, \tag{2.10}$$

which is a set of half-integer plateaus as shown in Fig. 2.5 (c).

2.1.5 QHE in bilayer and multilayer graphene

After introducing a distinct type of IQHE in monolayer graphene [106] which is the relativistic counterpart of a conventional semiconductor system, a third type of QHE was observed experimentally [106] that was different from the two previously known cases. The new character of the IQHE in bilayer graphene adds interesting features [106].
It has been shown [106] that the low-energy spectrum of Bernal stacked bilayer graphene near the K and K' points is known to be a parabolic (see Fig. 2.6 (a))

$$E(k) = k^2. \tag{2.11}$$

Further analysis showed that [107] the corresponding effective Hamiltonian of this dispersion can be described as

$$H = -\frac{1}{2m}\begin{pmatrix} 0 & (\pi^\dagger)^2 \\ \pi^2 & 0 \end{pmatrix}, \tag{2.12}$$

where $\pi = p_x + ip_y$. When a fermion which its properties are determined by this Hamiltonian encircles a closed path in the momentum space, it gains a Berry's phase of 2π [106]. In fact, this Berry's phase leads to an extra two-fold degeneracy of the zero-energy LL [106]. A similar treatment with Eq. (2.12) as in the case of monolayer graphene results in the energy spectrum of

$$E_{n,\pm} = \pm\hbar\omega_c\sqrt{n(n-1)}, \quad n = 0, 1, 2, \cdots, \tag{2.13}$$

for bilayer graphene when it is subjected to a perpendicular uniform magnetic field [106]. This equation shows that for bilayer graphene the two lowest states with zero-energy come from the LLs of $n = 0$, and $n = 1$, which creates an extra two-fold degeneracy [106]. This two-fold degeneracy emerges in the corresponding DOS as schematically shown in Fig. 2.6 (b). On the other hand, there exist a four-fold degeneracy in all of the LLs due to the spin and valley degrees of freedom [106]. This form of Landau quantization leads
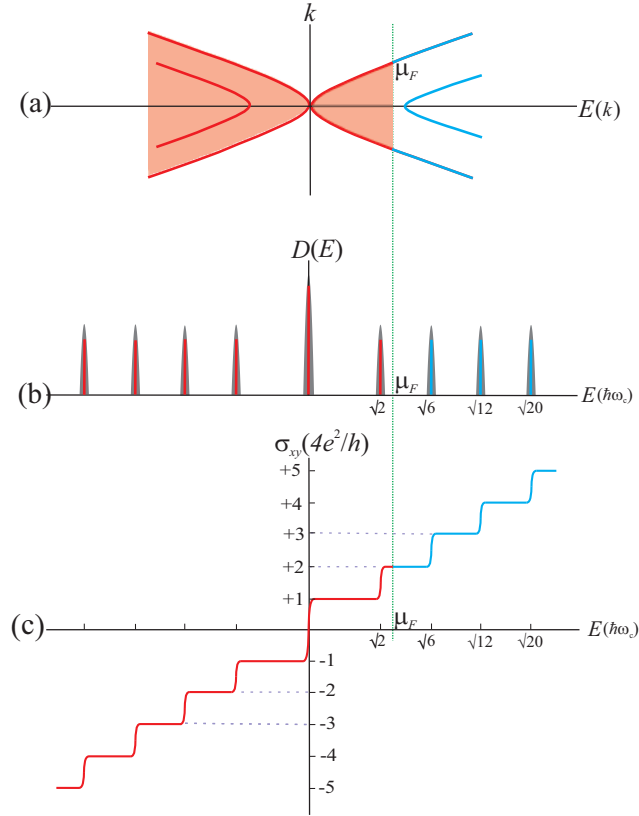
Figure 2.6: (a) Schematic view of the low-energy dispersion of bilayer graphene. (b) DOS of bilayer graphene in the presence of a strong magnetic field and weak disorder. There exists an extra two-fold degeneracy at zero-energy mode. (c) The corresponding Hall conductivity as a function of the chemical potential.

to the standard integer position of Hall plateaus except for zero energy states [106]. At zero energy, one can see the missing plateau and a double step in the Hall conductivity as shown in Fig. 2.6 (c). Note that this eight-fold degeneracy is a manifestation of the one-electron picture analysis [106], and if one takes into account the Coulomb interaction as a many-body effect, then the zero-energy level will split into eight non-degenerate sub-levels [102].

We now comment on the IQHE in multilayer graphene. It has been shown that the unconventional QHE in j-layer graphene [102] has the same general trend as in the case of bilayer except for the zero energy level. Similar to the bilayer case, when a low-energy quasi-particle of j-layer graphene encircles a closed contour in reciprocal space, it gains a Berry's phase of $j\pi$. This leads to an extra j-fold degeneracy [106] in the zero-energy
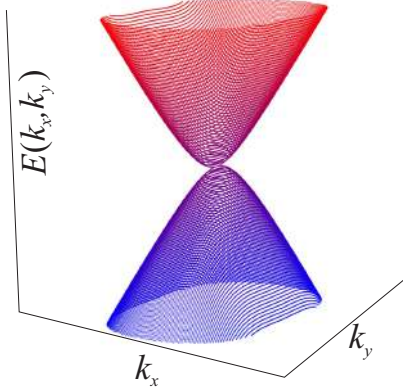
Figure 2.7: Low-energy spectrum for a graphene-like structure with linear dispersion in one direction and parabolic in the other.

.

level, though for all other levels the degeneracy is 4-fold as in monolayer and bilayer cases. Again, one can see directly this extra j-fold degeneracy by applying a perpendicular uniform magnetic field to a sheet of j-layer graphene where its LLs are given by [102]

$$E_{n,\pm} = \pm\hbar\omega_c\sqrt{n(n-1)(n-2)...(n-j)}, \quad n = 0, 1, 2, \cdots. \tag{2.14}$$

Equation 2.14 explicitly shows that the states $E_0 = E_1 = ... = E_j$ lie at zero energy. The corresponding Hall conductivity is quantized as [102]

$$\sigma_{xy} = \pm(n + \frac{j}{2})\frac{4e^2}{h}. \quad n = 0, 1, 2, \cdots. \tag{2.15}$$

2.1.6   LLs for a highly anisotropic band dispersion

We examined in the previous sections the field dependence of the LLs in conventional semiconductors and j-layer graphene. Dietl et al. [74] put forward a new example where the dependency of LLs on the magnetic field was neither linear nor has the behavior as in the case of j-layer graphene. They considered a graphene-like structure in which its dispersion relation is linear in one direction and parabolic in the other [74] (see Fig. 2.7). Using the TB method as well as the continuum approximation [74] they showed that this type of energy spectrum reveals LLs with a different magnetic field dependence

$$E_n \propto [(n + \frac{1}{2})B]^{2/3} \quad n = 0, 1, 2, \cdots. \tag{2.16}$$
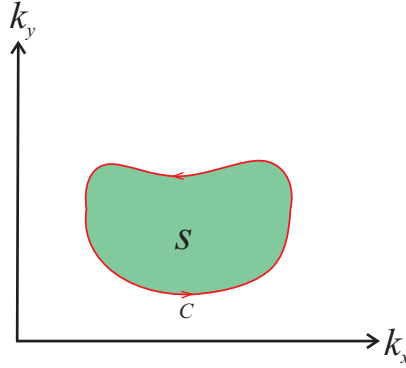
Figure 2.8: A schematic representation of the parallel transport on a closed path C in the k space. S is the corresponding enclosed area.

2.2 The role of topology

As many phenomena in both classical and quantum mechanics, the QHE is an example that topological features play an essential role in explaining the physics behind it [108]. The experimental observation of this topological effect [52] provided extra motivation for researchers and led to a new paradigm in the way of thinking about the phenomenon. Therefore, during the last four decades, the condensed matter physics community has encountered a great increase in using the geometrical phase concept and the corresponding appeared topological phases [108]. These topological characteristics emerge as topological invariants which remain unchanged under weak continuous perturbations [108].

2.2.1 Berry's phase

It is well known that the Berry's phase occupy a special place in quantum mechanics and solid state physics [109, 110]. Particularly, it plays the key role in topological band theory [110]. Let us consider an adiabatic evolution of non-degenerate Bloch state $|u_n(\boldsymbol{k})\rangle$ under parallel transport in momentum space (see Fig. 2.8). The differential displacement of $\boldsymbol{k} \longrightarrow \boldsymbol{k} + d\boldsymbol{k}$ gives

$$|u_n(\boldsymbol{k} + d\boldsymbol{k})\rangle \longrightarrow |u_n(\boldsymbol{k})\rangle + \nabla_{\boldsymbol{k}}|u_n(\boldsymbol{k})\rangle \cdot d\boldsymbol{k} . \tag{2.17}$$

Using the parallel projection operator $\boldsymbol{P}_{||} = |u_n(\boldsymbol{k})\rangle\langle u_n(\boldsymbol{k})|$, the parallel component is given by

$$\boldsymbol{P}_{||}|u_n(\boldsymbol{k} + d\boldsymbol{k})\rangle = |u_n(\boldsymbol{k})\rangle + \langle u_n(\boldsymbol{k})|\nabla_{\boldsymbol{k}}|u_n(\boldsymbol{k})\rangle \cdot d\boldsymbol{k} . \tag{2.18}$$

We define the Berry connection of nth band as

$$\boldsymbol{\mathcal{A}}_n(\boldsymbol{k}) = \langle u_n(\boldsymbol{k})|\nabla_{\boldsymbol{k}}|u_n(\boldsymbol{k})\rangle, \tag{2.19}$$

and link the two Bloch states $|u_n(\boldsymbol{k})\rangle$ and $|u_n(\boldsymbol{k} + d\boldsymbol{k})\rangle$ as

$$\langle u_n(\boldsymbol{k})|u_n(\boldsymbol{k} + d\boldsymbol{k})\rangle = 1 + \boldsymbol{\mathcal{A}}_n(\boldsymbol{k}) \cdot d\boldsymbol{k} \ . \tag{2.20}$$

It is straightforward to show that finite parallel transport from $\boldsymbol{k}_i$ to $\boldsymbol{k}_f$ gives the connection between the corresponding Bloch states as

$$\langle u_n(\boldsymbol{k}_i)|u_n(\boldsymbol{k}_f)\rangle = e^{\int_{\boldsymbol{k}_i}^{\boldsymbol{k}_f} \boldsymbol{\mathcal{A}}_n(\boldsymbol{k}) \cdot d\boldsymbol{k}} \ . \tag{2.21}$$

Therefore, the Bloch state $|u_n(\boldsymbol{k})\rangle$ acquires a geometrical phase on a closed path in k space as

$$e^{i\gamma_n(c)} = e^{\oint_c \boldsymbol{\mathcal{A}}_n(\boldsymbol{k}) \cdot d\boldsymbol{k}} \tag{2.22}$$

where the corresponding Berry's phase $\gamma_n(c)$ of nth band is given by [110]

$$\gamma_n(c) = -i \oint_c \boldsymbol{\mathcal{A}}_n \cdot d\boldsymbol{k} \ . \tag{2.23}$$

One can easily check that under the transformation

$$|u_n(\boldsymbol{k})\rangle \longrightarrow e^{i\phi_n(\boldsymbol{k})}|u_n(\boldsymbol{k})\rangle, \tag{2.24}$$

the Berry connection $\boldsymbol{\mathcal{A}}_n(\boldsymbol{k})$ transforms as

$$\boldsymbol{\mathcal{A}}_n(\boldsymbol{k}) \longrightarrow \boldsymbol{\mathcal{A}}_n(\boldsymbol{k}) + \nabla_{\boldsymbol{k}}\phi_n(\boldsymbol{k}). \tag{2.25}$$

This suggests that $\boldsymbol{\mathcal{A}}_n(\boldsymbol{k})$ behaves very much like electromagnetic vector potentials and is therefore called Berry potential. Equation (2.25) means that the Berry connection is not gauge invariant, but the corresponding magnetic flux (2.23) is gauge invariant. This motivates us to define the analog Berry field strength or Berry curvature of nth band as

$$\mathcal{F}_{xy}^{(n)} = (\nabla_{\boldsymbol{k}} \times \boldsymbol{\mathcal{A}}_n(\boldsymbol{k}))_z, \tag{2.26}$$

which is explicitly gauge invariant. Hence, using Stokes theorem, the Berry phase can be rewritten as

$$\gamma_n(c) = \oint_S \mathcal{F}_{xy}^{(n)} d^2k. \tag{2.27}$$

Note that in the above equation we have limited ourselves to a 2D band.
Our goal in the next subsection is to derive an important formula that provides a general link between the quantum Hall conductivity and a topological invariant which originates from the topology of the electronic bands.

2.2.2 Chern number and Hall conductance

As stated before, the geometrical phase of the system provides the topological features of the QHE. The first analytical derivation for the quantized Hall conductance in terms of a topological invariant was given by Thouless, Kohmoto, Nightingale, and den Nijs (TKNN) [54] which is known as the first Chern number c_n. This invariant is in close relation with the Berry phase of the system. They used the Kubo formula approach for the electrical conductivity in the context of the QHE [54]. Using time-dependent perturbation theory, and within the linear response regime, the Kubo formula for zero frequency can be written as [54].

$$\sigma_{xy} = -i\hbar \int_{\text{BZ}} \frac{d^2k}{(2\pi)^2} \sum_{E_n < E_F, E_m > E_F} n_F(E_n) \frac{j^\alpha_{nm} j^\beta_{mn} - j^\beta_{nm} j^\alpha_{mn}}{(E_n - E_m)^2}, \tag{2.28}$$

where E_F and n_F denote the Fermi energy and the Fermi distribution function, respectively, and E_n shows the eigenvalue of the corresponding eigenvector $|u_n(\boldsymbol{k})\rangle$ of the unperturbed Hamiltonian H_0. Here, the integration is taken over the entire BZ of the system and the summation runs over all the states below and above the Fermi energy. Also, $j^\alpha = e/\hbar \partial H_0/\partial k_\alpha$ is the αth component of the current operator with the element of $j^\alpha_{nm} = \langle u_n(\boldsymbol{k})|j^\alpha|u_m(\boldsymbol{k})\rangle$. Using [111]

$$j^\alpha_{nm} = \frac{e}{\hbar}\langle u_n(\boldsymbol{k})|\frac{\partial H_0}{\partial k_\alpha}|u_m(\boldsymbol{k})\rangle = \frac{e}{\hbar}(E_n - E_m)\langle \frac{\partial u_n}{\partial k_\alpha}|u_m(\boldsymbol{k})\rangle, \tag{2.29}$$

and the identity condition $\sum_{E_n < E_F} |u_n\rangle\langle u_n| + \sum_{E_m > E_F} |u_m\rangle\langle u_m| = 1$ one can rewrite Eq. (2.28) in the zero temperature limit as

$$\sigma_{xy} = -\frac{ie^2}{\hbar} \int_{\text{BZ}} \frac{d^2k}{(2\pi)^2} \sum_{E_n < E_F} \left(\langle \frac{\partial u_n}{\partial k_x}|\frac{\partial u_n}{\partial k_y}\rangle - \langle \frac{\partial u_n}{\partial k_y}|\frac{\partial u_n}{\partial k_x}\rangle \right), \tag{2.30}$$

where the summation runs over only the occupied bands. Using Eqs. (2.19) and (2.26) we can rewrite Eqs. (2.30) into the form

$$\begin{aligned} \sigma_{xy} &= \frac{e^2}{h} \sum_{E_n < E_F} \int_{\text{BZ}} \frac{d^2k}{2\pi i}(\partial_{k_x}\mathcal{A}^{(n)}_y - \partial_{k_y}\mathcal{A}^{(n)}_x) \\ &= \frac{e^2}{h} \sum_{E_n < E_F} \frac{1}{2\pi i} \int_{\text{BZ}} \mathcal{F}^{(n)}_{xy} d^2k \\ &= \frac{e^2}{h} \sum_{E_n < E_F} c_n, \end{aligned} \tag{2.31}$$

where we have defined the first Chern number assigned to the nth band as

$$c_n = \frac{1}{2\pi i} \int_{\mathrm{BZ}} \mathcal{F}_{xy}^{(n)} d^2 k. \tag{2.32}$$

This implies that when the Fermi energy lies in the gap of an insulating system, the Hall conductivity is quantized in units of e^2/h due to the quantization of the assigned total Chern number [54, 90]. Note that the generalization of Eq. (2.32) to the case of partially filled bands is given by [112]

$$\sigma_{xy}(E_F) = \frac{e^2}{h} \sum_\alpha \mathfrak{C}_\alpha, \tag{2.33}$$

with

$$\mathfrak{C}_\alpha(E_F) = \frac{1}{2\pi i} \int_{\mathrm{BZ}} \mathcal{F}_{xy}^{(\alpha)} \Theta(E_F - E_\alpha(\boldsymbol{k})) d^2 k, \tag{2.34}$$

where Θ and α denote the Heaviside function and the band index, respectively. Here, the Hall conductivity does not show plateaus because there exists a non-quantized contribution of the partially filled bands in the Chern number [112].

2.3 Lattice computation of the Chern number

From a numerical point of view, the construction of a numerical algorithm to calculate the Chern number requires to do calculations on a set of discrete points chosen appropriately within the BZ [90]. Fukui *et al.* [90] proposed an efficient method of calculating the Chern numbers to compute the Hall conductivity even on a coarsely discretized BZ. This method provides a manifestly gauge-invariant description of Chern numbers which is applicable to the non-Abelian Berry connection [90]. To see how this approach is implemented, we consider the corresponding BZ of a rectangular lattice as shown in Fig. 2.9. We then mesh the BZ so that each site of the lattice is defined by

$$\boldsymbol{k}_l = \frac{1}{2}(\frac{j_1}{N_1} G_1, \frac{j_2}{N_2} G_2), \qquad (j_{1(2)} = -N_{1(2)}, \ldots, N_{1(2)}), \tag{2.35}$$

where $G_{1(2)}$ is the reciprocal lattice constant in the direction x (y), $N_{1(2)}$ is a positive integer, and l specifies the lth plaquette. Therefore, the lattice version of Eq. (2.32) can be written as

$$c_n = \frac{1}{2\pi i} \sum_{\boldsymbol{k}_l \in \mathrm{BZ}} \mathcal{F}_{xy}^{(n),l}, \tag{2.36}$$
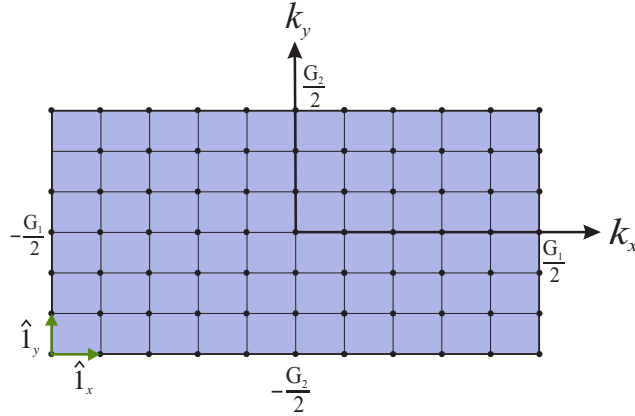
Figure 2.9: The lattice mesh on the BZ of a rectangular lattice with reciprocal lattice constants G_1 and G_2.

where

$$\mathcal{F}_{xy}^{(n),l} = \int_{\text{plaquette}} \mathcal{F}_{xy}^{(n)} d^2 k, \tag{2.37}$$

is the Berry curvature contribution of the lth plaquette in the nth band and can be approximated for small plaquettes as

$$\mathcal{F}_{xy}^{(n),l} \approx \mathcal{F}_{xy}^{(n)}(\boldsymbol{k}_l)|\hat{\boldsymbol{1}}_x||\hat{\boldsymbol{1}}_y|, \tag{2.38}$$

where $\hat{\boldsymbol{1}}_x$ and $\hat{\boldsymbol{1}}_y$ are vectors in the directions of x and y, respectively, which define the size of a plaquette with dimension $G_1/2N_1 \times G_2/2N_2$.

Using the non-degenerate Bloch state $|u_n(\boldsymbol{k})\rangle$ which is periodic on the lattice, we define the corresponding link variables of nth band at the lth plaquette as [90]

$$U_{x(y)}(\boldsymbol{k}_l) = \langle u_n(\boldsymbol{k}_l)|u_n(\boldsymbol{k}_l + \hat{\boldsymbol{1}}_{x(y)})\rangle. \tag{2.39}$$

This allows us to define a lattice field strength as [90]

$$\tilde{F}_{xy}(\boldsymbol{k}_l) = \ln \frac{U_x(\boldsymbol{k}_l)U_y(\boldsymbol{k}_l + \hat{\boldsymbol{1}}_x)}{U_y(\boldsymbol{k}_l)U_x(\boldsymbol{k}_l + \hat{\boldsymbol{1}}_y)}. \tag{2.40}$$

It has been shown [90] that even for not very large mesh sizes the admissibility condition $|\tilde{F}_{xy}(\boldsymbol{k}_l)| < \pi$ is satisfied. Therefore, the lattice gauge theory is equivalent to the continuous gauge theory [113, 114] and we have

$$\mathcal{F}_{xy}^{(n)}(\boldsymbol{k}_l)|\hat{\boldsymbol{1}}_x||\hat{\boldsymbol{1}}_y| \approx \tilde{F}_{xy}(\boldsymbol{k}_l). \tag{2.41}$$

Hence, the discretized BZ version of Eq. (2.32) for numerical computing the Chern number of nth band can be rewritten as [90]

$$c_n = \frac{1}{2\pi i} \sum_{\boldsymbol{k}_l} \tilde{F}_{xy}(\boldsymbol{k}_l), \tag{2.42}$$

where each plaquette $\boldsymbol{k}_l$ in the summation is determined by the counters j_1 and j_2 which now run from $-N_1$ to $N_1 - 1$ and $-N_2$ to $N_2 - 1$, respectively to cover all plaquettes in the BZ.

It is worth mentioning that Eq. (2.42) is applicable for an insulating case with non-degenerate bands where the corresponding highest occupied energy band is completely filled. The generalized Eq. (2.33) for cases of partially filled bands can be estimated using the lattice version as [112]

$$\mathfrak{C}_\alpha(E_F) \approx \frac{1}{2\pi i} \sum_{\boldsymbol{k}_l} \mathcal{F}_{xy}^{(\alpha),l} \, p_l^\alpha(E_F), \tag{2.43}$$

where $p_l^\alpha(E_F)$ are weighting factors which determine the contribution of a given plaquette in the corresponding Chern number of αth band. To numerically compute the Chern number Eq. (2.43), we first calculate the contribution $\mathcal{F}_{xy}^{(\alpha),l}$ using the numerical formula Eq. (2.42). Then, one can generate uniform distribution of random points in the lth plaquette to estimate the weights $p_l^\alpha(E_F)$ with known and controllable statistical error bars [112] as

$$p_l^\alpha(E_F) = \frac{1}{n_r} \sum_{\boldsymbol{k}_r} \Theta(E_F - E_\alpha(\boldsymbol{k_r})), \tag{2.44}$$

where n_r is the number of generated random points $\boldsymbol{k}_r$.

On the other hand, it is very important to note that wherever bands cross or degeneracies are present in the energy spectrum, the Berry connection and the Berry curvature must be extended to non-Abelian gauge field analogies [115] associated with a ground state multiplet $|\psi(\boldsymbol{k})\rangle = (|u_1(\boldsymbol{k})\rangle, ..., |u_{2M}(\boldsymbol{k})\rangle)$ in the equation $\mathcal{H}(\boldsymbol{k})|u_n(\boldsymbol{k})\rangle = E_n(\boldsymbol{k})|u_n(\boldsymbol{k})\rangle$. Based on this extension, the modified non-Abelian Berry connection and Berry curvature are given by [115, 116]

$$A(\boldsymbol{k}) = \mathrm{Tr}\,\psi(\boldsymbol{k})^\dagger \mathrm{d}\psi(\boldsymbol{k}), \tag{2.45}$$

$$F = \mathrm{d}A, \tag{2.46}$$

where A is an $M \times M$ matrix. In this extension, we substitute the link variable in Eq. (2.39) by [90]

$$U_{x(y)}(\boldsymbol{k}_l) = \frac{\det\psi^\dagger(\boldsymbol{k}_l)\psi(\boldsymbol{k}_l + \hat{\boldsymbol{1}}_{x(y)})}{|\det\psi^\dagger(\boldsymbol{k}_l)\psi(\boldsymbol{k}_l + \hat{\boldsymbol{1}}_{x(y)})|}. \tag{2.47}$$

It was shown that the described lattice prescription is valid for computing the associated field strength and the Chern number on the lattice [90]. Note that the Berry field strength is defined within the branch of $F_{xy}(\boldsymbol{k}_l)/i \in (-\pi, \pi]$ [90].

2.3.1   The Haldane model

As an example, we consider the Haldane model [117] to show that the described lattice prescription for computing the Chern number and the Hall conductivity successfully predicts the realization of both topological and trivial phases in this model. The Haldane model is a two-band TB Hamiltonian of spinless fermions on a honeycomb lattice [112] as we introduced its geometrical parameters in Fig. 2.4. The Hamiltonian reads as follows

$$H = t_1 \sum_{\langle ij \rangle} c_i^\dagger c_j + it_2 \sum_{\langle\langle ij \rangle\rangle} \nu_{ij} c_i^\dagger c_j + M \sum_i s_i c_i^\dagger c_i, \tag{2.48}$$

where $c_i^\dagger$ and c_j are the creation and annihilation operators of spinless fermions at sites i and j, respectively. t_1 is the real nearest-neighbor hopping integral in which its corresponding term gives rise to the massless Dirac fermions [112]. The second term introduces an imaginary next-nearest neighbor hopping term with the magnitude of t_2 which breaks the time-reversal symmetry [117]. Here ν_{ij} takes the value of $+1$ (-1) if going from the site i to the next-nearest-neighbor site j be anticlockwise (clockwise) with respect to the positive z axis. The third term is a staggered sub-lattice potential ($s_i = \pm 1$) with the strength of M which breaks the inversion symmetry.

The Fourier transform of the Hamiltonian Eq. (2.48) gives the Bloch Hamiltonian in momentum space as

$$H = \sum_{\boldsymbol{k}} \psi_{\boldsymbol{k}}^\dagger H_{\boldsymbol{k}} \psi_{\boldsymbol{k}}, \tag{2.49}$$

where we have used the basis spinor $\psi_{\boldsymbol{k}}^\dagger = \{\psi_A^\dagger, \psi_B^\dagger\}$, and $H_{\boldsymbol{k}}$ is given by

$$H_{\boldsymbol{k}} = \begin{pmatrix} M + g(\boldsymbol{k}) & f(\boldsymbol{k}) \\ f^*(\boldsymbol{k}) & -M - g(\boldsymbol{k}) \end{pmatrix}, \tag{2.50}$$

where

$$\begin{aligned} f(\boldsymbol{k}) &= t_1[e^{i\boldsymbol{k}\cdot\boldsymbol{a_1}} + e^{i\boldsymbol{k}\cdot\boldsymbol{a_2}} + 1], \\ g(\boldsymbol{k}) &= 2t_2[-\sin(\boldsymbol{k}\cdot\boldsymbol{a}_1) + \sin(\boldsymbol{k}\cdot\boldsymbol{a}_2) - \sin(\boldsymbol{k}\cdot(\boldsymbol{a}_2 - \boldsymbol{a}_1))]. \end{aligned} \tag{2.51}$$

One can simply diagonalize this Hamiltonian to obtain the two-band energy spectrum

$$E(\boldsymbol{k}) = \pm\sqrt{|f(\boldsymbol{k})|^2 + (M - g(\boldsymbol{k}))^2}, \tag{2.52}$$
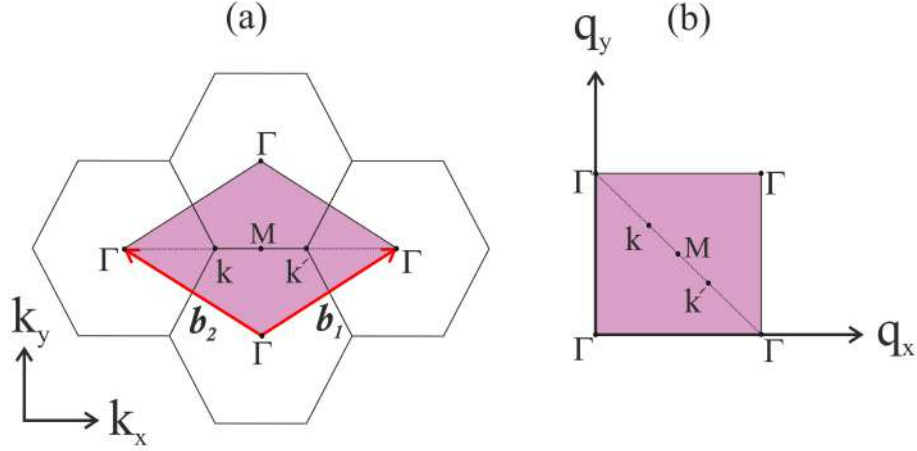
Figure 2.10: Conversion of the equivalent (a) rhombus shape of the honeycomb BZ in k space into a (b) unit square in q space.

which results in the energy gap

$$E_g = 2|M - 3\sqrt{3}t_2|, \tag{2.53}$$

at K and K' points. For $M = 3\sqrt{3}t_2$, a band closure occurs which divides the plane M-t_2 into two regions. The induced gap by the time-reversal breaking hopping term t_2 is topologically non-trivial which signals a possible phase transition [112]. To determine the topology of each region, we proceed by numerical calculation of the Chern number and the Hall conductivity for the Haldane model Eq. (2.48) at various Hamiltonian parameters M and t_2 in the unit of t_1 as the energy scale.

Equation (2.42) is the formula for computing the Chern numbers in a rectangular lattice. Therefore, in order to use this formula for the Haldane model with a honeycomb lattice, one can simply convert the equivalent rhombus shape of the honeycomb BZ in k space as shown in Figs. 2.10(a) and (b) into a unit square in q space by the following change of variables

$$k_x = \frac{2\pi}{a}(q_x - q_y), \quad k_y = \frac{2\pi}{\sqrt{3}a}(q_x + q_y). \tag{2.54}$$

This, allows us to rewrite Eq. (2.42) as

$$c_n = \frac{1}{2\pi i} \sum_{\boldsymbol{q}_l} \tilde{F}_{xy}(\boldsymbol{q}_l), \tag{2.55}$$

where the lattice sites of the BZ are labeled by $\boldsymbol{q}_l$. The unimodular link variable U and the lattice field strength $\tilde{F}_{xy}$ are rewritten in the q_x-q_y plane, and the numerical calculation is
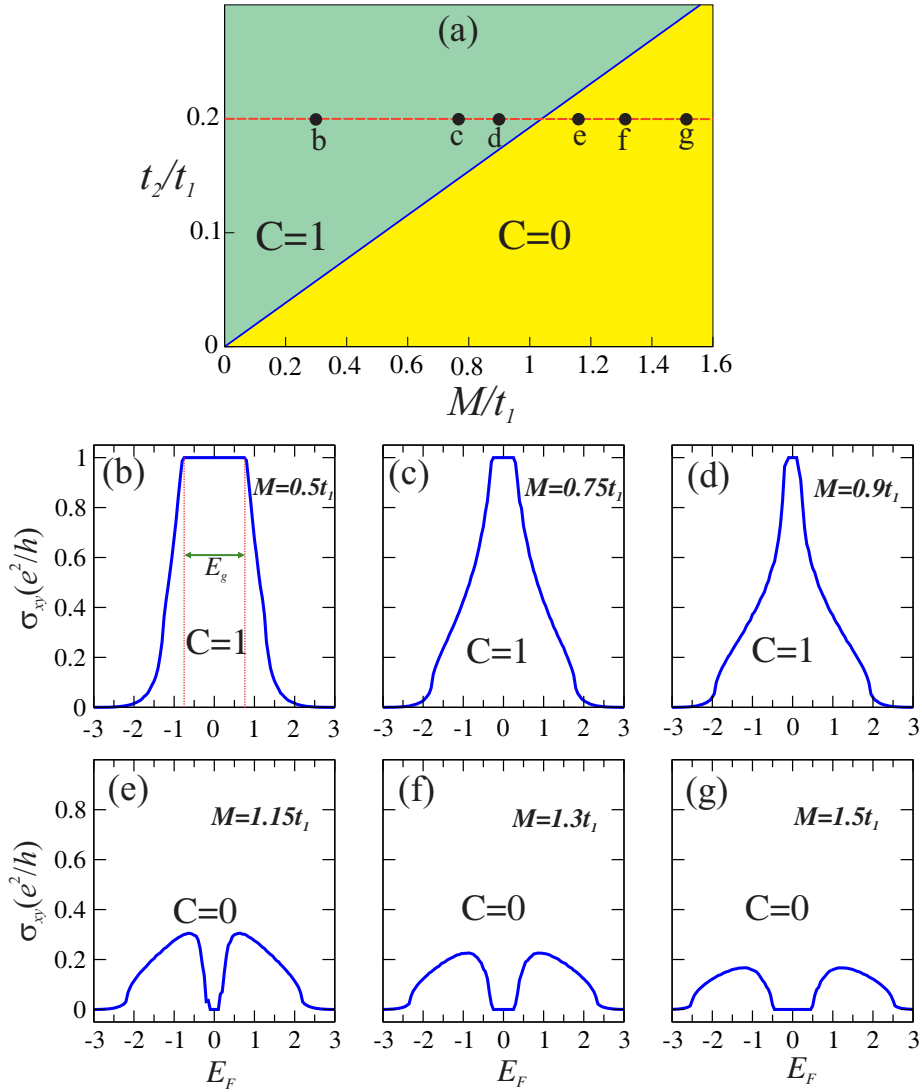
Figure 2.11: (a) The equation $t_2 = 1/(3\sqrt{3})M$ divides the M-t_2 plane in the Haldane model into two topologically different regions. (b)-(g) The numerically obtained Berry connection in the Haldane model as a function of the Fermi energy E_F for the fixed Hamiltonian parameter $t_2 = 0.2t_1$, and some increasing values of the Hamiltonian parameter M.

done over the lattice version of square BZ in Fig. 2.10 (b).

Now, we discretize this BZ and fix the resolution of the grid ($n_B = 20$) to compute the associated field strength $\tilde{F}_{xy}$ of each plaquette. Next, we fix the Fermi energy at $E_F = 0$ and compute the Chern number (2.55) for Hamiltonian parameters M and t_2 so that

$M \neq 3\sqrt{3}t_2$. As shown in Fig. 2.11(a), the M-t_2 plane is divided into two topologically different phases $C = 0$ and $C = 1$. Here, $C = 0$ corresponds to a normal insulating phase whereas $C = 1$ demonstrates a topologically non-trivial phase which is known as anomalous quantum Hall effect [112]. We have also shown in Figs. 2.11(b)-(g), the numerically obtained Berry connection (2.31) in the Haldane model as a function of the Fermi energy E_F for the fixed Hamiltonian parameter $t_2 = 0.2t_1$, and some increasing values of the Hamiltonian parameter M to clearly show the transition from the non-trivial phase $C = 1$ to the trivial phase $C = 0$. Note that, by varying the Fermi energy, one encounters with partially filled bands. Therefore, one needs to use Eqs. (2.43) and (2.44) to correctly consider their contributions. Here, we have chosen $n_r = 20$ to estimate the contribution of each plaquette in determining the Chern number of αth band. As seen, in the topological phase and for the the Hamiltonian parameters where the Fermi energy lies in the gap, the obtained Berry conductivities show plateaus of conductance in which their widths follow the analytical relation $E_g = 2|M - 3\sqrt{3}t_2|$.

Topological insulators with time-reversal symmetry

So far, we have been dealing with the topological properties of systems with broken time-reversal symmetry (TRS). We showed that the topologically non-trivial nature of such systems manifests as the quantum Hall states at the boundaries of the sample. However, in practice, the observation of the usual IQHE requires very low temperature and high magnetic field. This leads to a rather complex experimental setup that makes it difficult to control and manipulate the chiral edge modes. This puts a limit on the actual applications of the IQHE and restricts it usually to fundamental research. These limitations imposed by the breaking of TRS due to applying an external magnetic field raised the fundamental question: is there any other topologically non-trivial phase which preserves the TRS?

This question was first theoretically answered by Kane and Mele [57] and Bernevig and Zhang [58] in two independent works, and soon after was verified experimentally in mercury telluride (HgTe) quantum well systems [118]. This new phase of matter in two dimensions is referred to as the 2D topological insulator or the quantum spin Hall effect (QSHE). Even though both suggestions of Kane and Mele [57] and Bernevig and Zhang [58] are excellent proposals for theoretical prediction of the QSHE, however they cannot be realized experimentally. Kane and Mele proposed their model in a sample of graphene including spin-orbit (SO) interaction. However, the induced gap due to SOC in graphene is only of the order of μeV [119] which makes the realization of the QSHE rather unrealistic. The suggestion of Bernevig and Zhang for experimental realization of the QSH phase in conventional semiconductors in the presence of a strain gradient is also difficult to be achieved [120]. In 2006, Bernevig, Hughes, and Zhang [121] proposed that the QSH ef-

fect can be experimentally observed in a sample of inverted type-III HgTe/CdTe quantum well. They showed that a phase transition from a normal insulator (NI) to a TI can occur in this particular system depending on the thickness of the quantum well [121]. Their prediction was verified one year later by the group of Molenkamp [118] using quantum transport measurements. These experimental observations quickly caught the attention of the scientific community during the last decade which resulted in an explosion of studies on new topological materials.

The growing amount of attention devoted to this field is due to the fact that the physics behind the topic of TIs is very deep which can give rise to many potential applications in device technology. There exists already a considerable body of literature on the subject, [92, 122–132]. The goal of this chapter is to provide a short but comprehensive overview of the physics behind topological band insulators with TRS. In the first section, we describe shortly the main characteristics of TIs. The next section will introduce the QSHE in graphene as a basic example to explain the salient features of TIs starting with an introduction of the TRS and its consequences on the energy spectrum of a periodic system. In Sec. 3.3, we proceed by giving a brief overview of the different ways to distinguishing a TI from an NI. Then, in Sec. 3.4 we will review an algorithm to compute the $\mathbb{Z}_2$ invariant. This provides a numerical method to quantitatively distinguish a TI from an NI. Finally, in Sec. 3.5 we will address the experimental signatures of TIs by introducing the most important methods used in demonstrating the realization of 2D and 3D TIs.

3.1   What makes TIs interesting?

TIs are new quantum states of matter which have attracted a lot of interest within the condensed matter physics community during the past decade [121–128]. They possess a bulk insulating gap and conducting edge/surface states [121–128]. These states are protected by TRS against backscattering which makes them robust against disorder and non-magnetic defects. In what follows, I will describe shortly the main characteristics of TIs that makes them interesting for advanced photodetectors, magnetic devices, field effect transistors and lasers [133, 134].

Low-power electronics

All of us have experiences heating of today's electronic devices. This is due to the fact that when electrons are moving through the electronic components, they scatter. They scatter by lattice atoms, impurities, and phonons, giving rise to resistance. This resistance leads to heating of the device. Moreover, the complementary metal oxide semiconductors (COMS) scaling theory is coming to an end [135]. The reason originates from physical

and technological limitations [135]. One of the most important limitations is the restriction of operating voltage reduction [135]. Without voltage reduction, the scaling will lead to very high power consumption and heat generation [135].

Therefore, the advent of a new revolution in electronics industry to overcome the mentioned limitations is urgently needed. So, the important question is: what will be the next generation of potential materials to power the next electronics revolution?

An important direction lies in the topological property of new potential materials, what are known as TIs. Taking into account the possibility that these states of TIs can have high carrier mobilities, it is important to consider another excellent feature that can be utilized to realize low-power dissipating transistors [135, 136]. This feature is the existence of topologically protected edge/surface states, a fundamental property of TIs that makes them immune to non-magnetic perturbations [135, 136]. In fact, this feature has been used as a basis for designing TI-based devices with high-performance and low-power electronic circuits [135, 136].

Photon-like electrons with higher mobility

Usually, the dispersion relation in an ordinary conductor is non-linear [136]. In contrast, the conducting edge/surface states of TIs are usually characterized by linear-like dispersion relation which are like the dispersion relation of photons [136]. This feature leads to improvement in the performance of semiconductor devices by providing higher carrier mobilities. As a result, the larger the carrier mobilities, the larger the speed of the carrier [136]. So, the research field of TIs has a great potential to tailor the mentioned favorable properties which finally leads to enhancement of semiconductor devices.

Intrinsic spin-polarized electrons

Another salient feature of TIs generated by SOC is the emergence of steady-state spin-polarized edge/surface electrons at their border [133, 134]. These states obey the massless Dirac equation which gives rise to unusual spin-momentum locking feature [133, 134]. As a result, one expects novel spintronics effects that can pave the way toward producing ultralow-power dissipation spintronic memory and logic devices [133, 134].

3.2   Quantum spin Hall effect

We start this section with an introductory to the TRS and its consequences on the energy spectrum of a periodic system. Then, we will proceed with the introduction of the concept of band inversion and its role in the appearance of flat-band edge states at the boundary
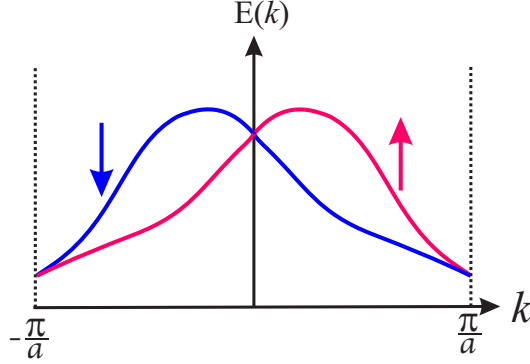
Figure 3.1: Part of a typical energy spectrum for a TR invariant system with spin $1/2$ which forms a Kramers pair. For a fixed energy level, $+\boldsymbol{k}$ state and $-\boldsymbol{k}$ state having the same energy. The special degenerate points are called TR invariant momenta.

of the sample. We then discuss the QSHE in a simple model Hamiltonian as the first theoretical example of a TI with TRS [57].

3.2.1   Time-reversal symmetry

The TR operator involves a transformation as

$$\Theta: \quad t \longrightarrow -t. \tag{3.1}$$

For a system of spin $1/2$, the only possible representation to satisfy the necessary conditions is

$$\Theta = -i\sigma_y K, \tag{3.2}$$

where σ_y is the y component of Pauli matrices and K is the complex conjugate operator. The important property of this operator is that two consecutive operations of Θ do not restore the system to its original configuration; but in fact, for a spin $1/2$ particle, it picks-up a minus sign as $\Theta^2 = -1$. For a TR invariant Hamiltonian H, the corresponding Bloch Hamiltonian $\mathcal{H}(\boldsymbol{k})$ satisfies [137, 138]

$$\mathcal{H}(-\boldsymbol{k}) = \Theta\mathcal{H}(\boldsymbol{k})\Theta^{-1}. \tag{3.3}$$

This identity implies that for any Bloch state $|\psi_{n,I}(\boldsymbol{k})\rangle$ with band index n, there exist at least another independent Bloch state $\Theta|\psi_{n,I}(\boldsymbol{k})\rangle = |\psi_{n,II}(-\boldsymbol{k})\rangle$ which has the same energy [138] i.e. $E_{n,I}(\boldsymbol{k}) = E_{n,II}(-\boldsymbol{k})$. This leads to the property that energy bands come in pairs which are called Kramers pairs. Figure 3.1 shows part of a typical energy spectrum for a TR invariant system with spin $1/2$. As seen, for a fixed energy level, $+\boldsymbol{k}$ state and

$-\boldsymbol{k}$ state have the same energy which requires that one half of the BZ is a mirror image of the other half. To show that these states are independent, one can rewrite the product $\langle\Theta\psi_{n,I}(\boldsymbol{k})|\psi_{n,I}(\boldsymbol{k})\rangle$ as

$$
\begin{aligned}
\langle\Theta\psi_{n,I}(\boldsymbol{k})|\psi_{n,I}(\boldsymbol{k})\rangle &= \langle\Theta\psi_{n,I}(\boldsymbol{k})|\Theta^{-1}|\psi_{n,II}(-\boldsymbol{k})\rangle \\
&= -\langle\Theta\psi_{n,I}(\boldsymbol{k})|\Theta\psi_{n,II}(-\boldsymbol{k})\rangle \\
&= -\langle\psi_{n,I}(\boldsymbol{k})|\psi_{n,II}(-\boldsymbol{k})\rangle^* \\
&= -\langle\Theta\psi_{n,I}(\boldsymbol{k})|\psi_{n,I}(\boldsymbol{k})\rangle \\
&= 0,
\end{aligned}
\tag{3.4}
$$

where we have used the identity $\langle\Theta\alpha|\Theta\beta\rangle = \langle\alpha|\beta\rangle^*$ for anti-unitary operator Θ. These features imply an important property of Kramers pairs that there is no scattering between them. In other words, by adding a TR invariant term V with $V^\dagger = V$ into the Hamiltonian, it follows

$$
\begin{aligned}
\langle\Theta\psi_{n,I}(\boldsymbol{k})|V|\psi_{n,I}(\boldsymbol{k})\rangle &= \langle\Theta V\psi_{n,I}(\boldsymbol{k})|\Theta^{-1}|\psi_{n,II}(-\boldsymbol{k})\rangle \\
&= -\langle\Theta V\psi_{n,I}(\boldsymbol{k})|\Theta\psi_{n,II}(-\boldsymbol{k})\rangle \\
&= -\langle V\psi_{n,I}(\boldsymbol{k})|\psi_{n,II}(-\boldsymbol{k})\rangle^* \\
&= -\langle\Theta\psi_{n,I}(\boldsymbol{k})|V|\psi_{n,I}(\boldsymbol{k})\rangle \\
&= 0.
\end{aligned}
\tag{3.5}
$$

This equality guarantees that if the two corresponding states of a Kramers pair show the edge modes of a 1D strip, then the single particle elastic backscattering between these states is forbidden.

Note that, the corresponding cell-periodic eigenfunctions of the Bloch states for a Kramers pair which are denoted as $|u_{n,I}(\boldsymbol{k})\rangle$ and $|u_{n,II}(-\boldsymbol{k})\rangle$ are related to each other as [138]

$$
\begin{aligned}
|u_{n,I}(-\boldsymbol{k})\rangle &= e^{i\chi(\boldsymbol{k},n)}\Theta|u_{n,II}(\boldsymbol{k})\rangle \\
|u_{n,II}(-\boldsymbol{k})\rangle &= -e^{i\chi(-\boldsymbol{k},n)}\Theta|u_{n,I}(\boldsymbol{k})\rangle,
\end{aligned}
\tag{3.6}
$$

where χ is a phase.

Moreover, there exist special points in which the Kramers pairs are always degenerate due to TRS protection. These points are known as TR invariant momenta (TRIM). Applying Θ on these points map them onto themselves due to the periodicity relation $-\boldsymbol{k} = \boldsymbol{k} + \boldsymbol{G}$, where $\boldsymbol{G}$ is a reciprocal lattice vector. For example, there are four (eight) distinct TRIM in the BZ of a rectangular lattice (simple orthorhombic lattice) as shown in Fig. 3.2 (a) ((b)). The QSHE can be understood from its close relation with QH states. Here, unlike the case of an usual QH system, we take into account the spin of electrons. Figure 3.3(a) shows
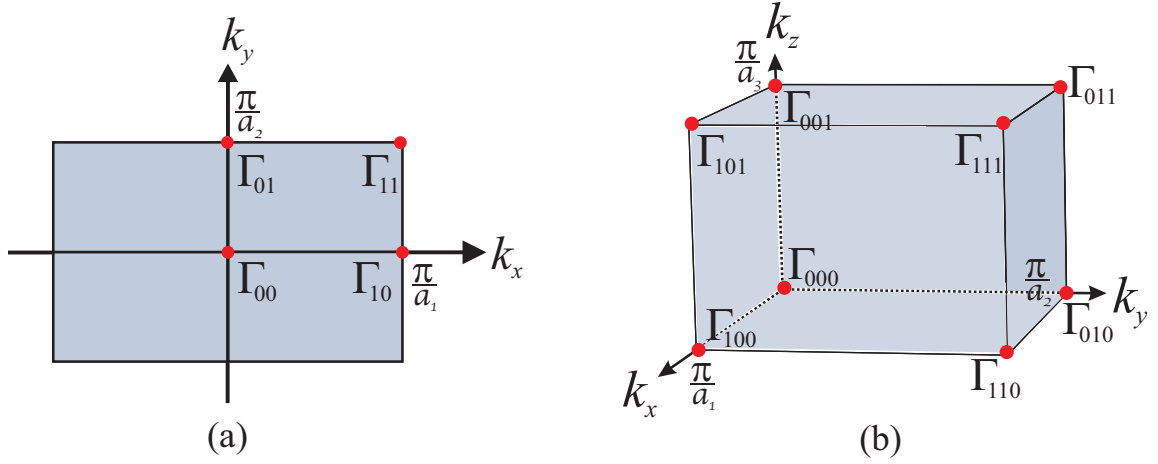
Figure 3.2: TRIM in the corresponding BZs of (a) a rectangular lattice and (b) a simple orthorhombic lattice. There are four (eight) distinct TRIM in the BZ of the rectangular lattice (the orthorhombic lattice) as indicated by the red dots.

a QH system corresponding to spin-up electrons at both edges of the sample. If one has another QH system with electrons that are moving in the opposite direction, then, they have spin-down (see Fig. 3.3(b)). In these systems, the direction of electron motion is determined by the direction of the magnetic field. The counterclockwise (clockwise) motion of spin-up (spin-down) electrons corresponds to magnetic field pointing up (down), as schematically illustrated in Fig. 3.3(a) (Fig. 3.3(b)). Putting these two QH systems together gives rise to the existence of a net spin current, but no charge current, as shown in Fig. 3.3(c). The existence of the net spin current is due to the forward motion of the spin-up electrons along one edge and their backward motion along the other edge. The corresponding conducting edge states are called helical because the propagation direction depends on the spin of the electrons. Under time reversal operation, the currents reverse direction and the spin of the electrons is flipped. Thus, as is clear in Fig. 3.3(c), applying the time reversal operator to the system keeps it unchanged. This implies that there exists no net magnetic field in the system. In other words, the spin-up and spin-down electrons exhibit QH effect without applying external magnetic field which is called a QSH system [92, 122–132]. Then, important question is whether such a situation can be realized?
  In order to respond to this question, it is useful to note that in the case of QH states the mechanism of separate lanes of electron propagation is provided by applying an external magnetic field. But, in a QSH system, one has to take into account another reason in order to have such separation. Kane and Mele [57] and then, Bernevig and Zhang [58] independently put forward respectively, in 2005 and 2006 the proposal that these separate lanes of
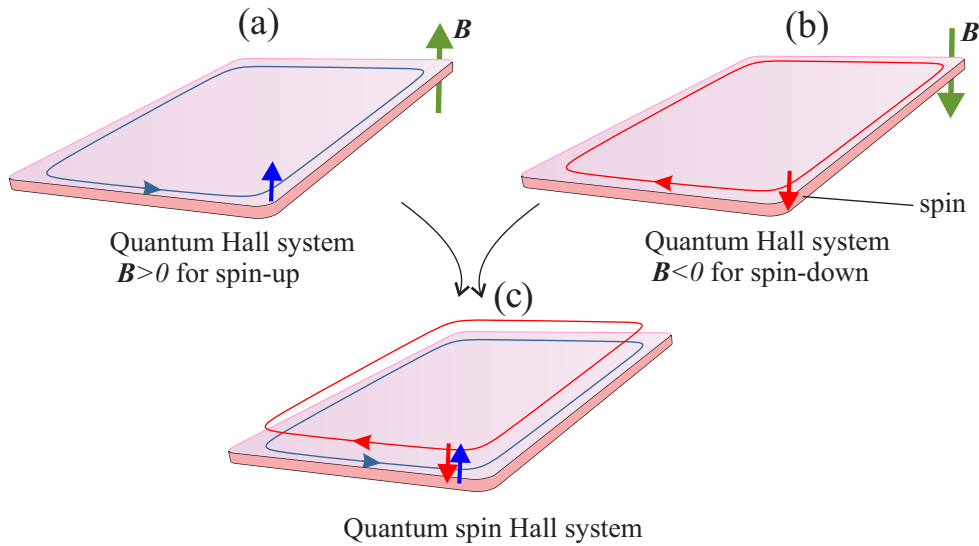
Figure 3.3: The QSH system (c) can be imagined as a superposition of two QH systems (a) and (b) which are related by the time-reversal operator.

electron propagation, and thus the QSH state can be realized in a model including SOC. They showed that the role of external magnetic fields in a QSH system is indeed played by SOC. In that sense, the spin-up and spin-down electrons feel opposite magnetic fields which is produced by an orbiting proton at their sites. Thus, the mentioned scenario of having two QH system together happens in the same matter, and therefore it can be found in a real material.

As seen, we have both backward and forward motion of electrons at each edge of a QSH system. Thus, in order to have dissipationless conducting edge states like in the case of a QH system, one can raise the question: is there any protection which prevents the mixing of these states and makes them robust against backscattering?. Fortunately, the answer is yes, provided that we have no magnetic impurity in the sample. This protection is provided by TRS.

To better understand the physics behind this protection, in the following we will briefly introduce the theoretical model proposed by Kane and Mele [57, 139] in order to show the formation of QSH sates in garphene.

3.2.2 Kane and Mele model

Kane and Mele [57] used graphene as an ideal model which has a rather simple analytical energy spectrum. They showed the first theoretical realization of QSH state in graphene

using a TB model including SOC. They proved [139] that in such a system a special protection can be defined by a different topological invariant. This invariant which corresponds to a topological protection must be something like the Berry phase which is defined in a Chern insulator as discussed in the previous chapter. Thus, one may ask whether the Berry phase is again a relevant quantity to identify the corresponding topological phases of such systems? Unfortunately, the answer is no! The reason is that the calculation of the Berry phases of spin-up and spin-down electrons gives $+\pi$ and $-\pi$, respectively. Hence, the total Berry phase of the system vanishes or is an integer multiple of 2π. This means that the Chern number does not work well for QSH systems. In Sec. (3.3.3), we will introduce the alternative topological invariant which is suitable for the classification of a time-reversal symmetric system.

In the previous chapter we introduced the lattice structure and the low-energy Hamiltonian of graphene without taking into account the spin degree of freedom. Here, we consider the Kane and Mele model which is a four-band TB model for a honeycomb lattice containing the following terms [57, 139]:

$$
\begin{aligned}
H =& t \sum_{\langle ij \rangle \sigma} c_{i\sigma}^{\dagger} c_{j\sigma} + i\lambda_{so} \sum_{\langle\langle ij \rangle\rangle \sigma\sigma'} \nu_{ij} c_{i\sigma}^{\dagger} s^z c_{j\sigma'} \\
&+ i\lambda_r \sum_{\langle ij \rangle \sigma\sigma'} c_{i\sigma}^{\dagger} (\mathbf{s} \times \hat{\mathbf{d}}_{ij})_z^{\sigma\sigma'} c_{j\sigma'} + \lambda_v \sum_{i\sigma} \xi_i c_{i\sigma}^{\dagger} c_{i\sigma},
\end{aligned}
\tag{3.7}
$$

where $c_{i\sigma}^{\dagger}$ is the creation operator of an electron with spin σ at site i. The first term is the usual nearest-neighbor interaction with hopping integral t where the summation runs over all the nearest-neighbor sites. The second term is the usual mirror symmetric SOC with the effective strength of λ_{SO} which involves the summation over the second neighbors as denoted by $\langle\langle ij \rangle\rangle$. Here ν_{ij} takes the value of $+1$ (-1) if going from site i to the next-nearest-neighbor site j be anticlockwise (clockwise) with respect to the positive z axis. In this term, s^z is the Pauli matrix that describes the z component of electron's spin. The third term is a nearest neighbor Rashba term with the strength of λ_R that is induced by a perpendicular electric field or interaction with a substrate [139]. The last term is a staggered sublattice potential ($\xi_i = \pm 1$) with the strength of λ_v which breaks the inversion symmetry.

To proceed, we start with the concept of band inversion and its consequences on the energy spectrum of a system. Next, we return to Eq. (3.7) to explain the role of SOC in the formation of QSH states in graphene.
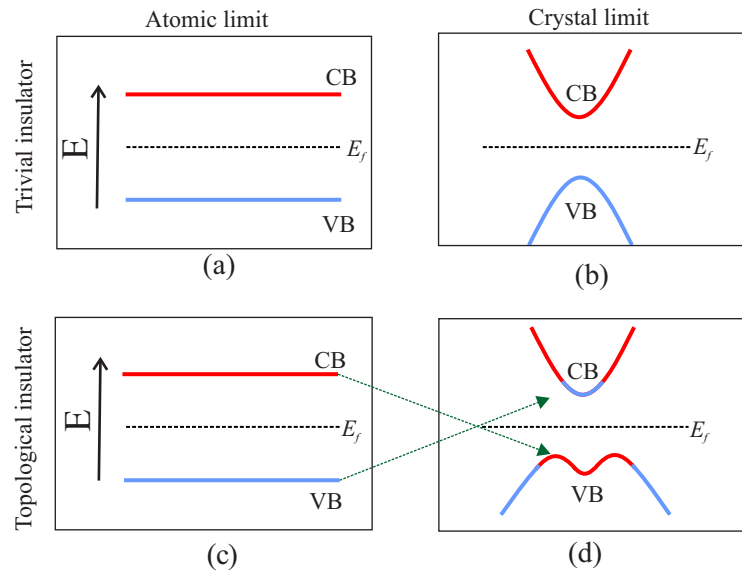
Figure 3.4: (a) and (c) show schematically the energy spectrum of insulators in the atomic limit in the absence of any band inversion. (b) and (c) represent the schematic spectrums of two topologically different band insulators. The deformation of the flat bands (a) to the spectrum (b) requires no change in the order of bands whereas for having the spectrum (d) one has to reverse the order of the VB and the CB in a range of k points.

Band inversion and its consequences

Let's start with the energy spectrum of atoms or ions of an insulator apart from each other into the atomic limit which is the simplest example of a trivial insulator. Figures 3.4(a) and (c) show schematically the corresponding narrow and flat VB and CB of these atoms or ions. We have also shown schematically the band structure of an insulator in Figs. 3.4 (b) and (d). Based on group theory arguments [140], these VB and CB may have different symmetries. This property also holds for the VB and CB of many crystalline materials. The basic idea behind the classification of topological insulators is that the band structure of two systems are said to be topologically equivalent if one can deform one band structure smoothly into another without closing the band gap [137, 141, 142]. Now, let's deform continuously the corresponding Hamiltonian of atomic insulators with the spectrums in Figs. 3.4(a) and (c) by changing the inter-atomic distances. As seen, in the crystal limit, these flat bands start to show dispersion. However, taking the symmetries of VB and CB into account, one can see that there exist a fundamental difference between the spectrums in Figs. 3.4(b) and (d). We have shown schematically the symmetries of the bands with different colors. As seen, the deformation from the flat bands in the atomic limit to the spectrum in Fig 3.4(b) requires no change in the order of bands. Hence, the resulting insulator is topologically equivalent to atomic insulator. Therefore, in this case, we have a conventional insulator. On the other hand, going from the atomic limit to the crystal limit of Fig. 3.4(d) requires that the order of the VB and the CB in a range of k points get reversed. This process is called band inversion. In this way, one can not do this deformation smoothly without closing the band gap. In other words, in order to have such a situation, one has to close and again open the band gap. Thus, the result is a band inverted insulator which is not topologically equivalent with a conventional insulator. In this sense, one can understand the underlying role of the topology and thus has to define a different class of band insulators, what we previously called TIs.

We proceed by explaining the details of the process of band inversion for the pristine honeycomb lattice of graphene. A carbon atom has four valence electrons with the configuration $2s^2 2p^2$ (see Fig. 3.5). Let's see what will happen after putting carbon atoms together into a hexagonal lattice. It is energetically favorable to excite electrons from $2s$ state to the $2p$ state. Then, the valence orbitals of the carbon atom are able to hybridize to form sp^2 orbitals. As shown in Fig. 3.5, after bringing them close to each other, they broadened to bonding and anti-bonding bands. Some of the valence electrons occupy strong in-plane σ bonds. This leads to the corresponding very low bonding and high anti-bonding of σ and σ^* bands as illustrated schematically in Fig. 3.5. The remaining p_z orbitals are perpendicular to the plane of graphene and are occupied by the other valence electrons to form π bonds. These p_z orbitals have two types of ordering. As shown in Fig. 3.6, the
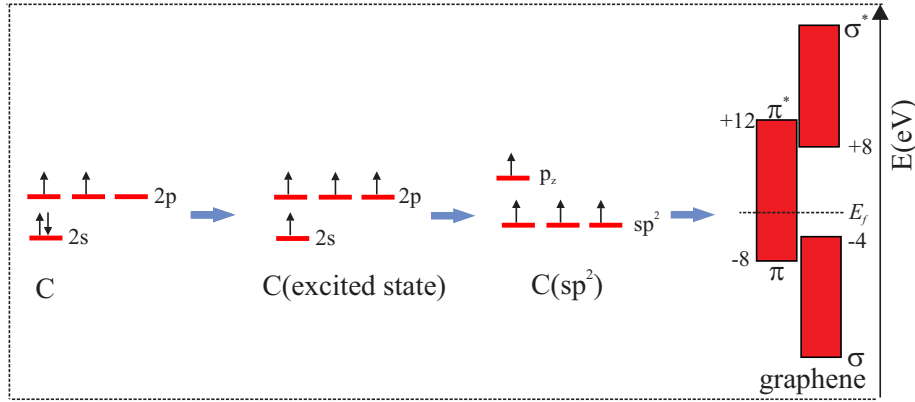
Figure 3.5: The procedure of forming bonding bonding and anti-bonding bands in graphene. Numerical values for the energy of bonding and anti-bonding bands have been taken from [143].

hybridization with lower energy is the weak π state, and the hybridization with higher energy corresponds to the weak π^* bond.

We now proceed to study the band structure of graphene given by the nearest-neighbor TB model. We rewrite the first term of Eq. (3.7) in the first quantization form as [144]

$$H = t \sum_{\langle ij \rangle} (|\phi_j^{\mathrm{A}}\rangle \langle \phi_i^{\mathrm{B}}| + h.c), \tag{3.8}$$

where $|\phi_j^{\mathrm{A}}\rangle$ and $|\phi_i^{\mathrm{B}}\rangle$ stand for the electronic states at the two nearest-neighbors of (j, A) and (i, B) that belong to different sub-lattices of A and B (see Fig. 3.7 (a)). Here, $t = -2.67$ eV is the nearest-neighbor hopping integral of the π bonds [144]. Now, lets examine the evolution of the energy bands along the high-symmetry directions as shown in Fig. 3.7(b) starting from the Γ point. Fourier transforming, one can easily obtain the energy spectrum of graphene as

$$E(\boldsymbol{k}) = \pm |f(\boldsymbol{k})|, \tag{3.9}$$

where the function f is given by

$$f(\boldsymbol{k}) = t(e^{i\boldsymbol{k} \cdot \boldsymbol{a_1}} + e^{i\boldsymbol{k} \cdot \boldsymbol{a_2}} + 1). \tag{3.10}$$

The corresponding eigenfunctions of the above TB Hamiltonian is found to be as [144]

$$\Psi^{\boldsymbol{k}}(\mathbf{r}) = \frac{1}{\sqrt{2N}} \sum_j e^{i\boldsymbol{k} \cdot \mathbf{R}_j} \left[\phi(\mathbf{r} - \mathbf{R}_j^A) \pm e^{-i\theta(k)} \phi(\mathbf{r} - \mathbf{R}_j^B) \right], \tag{3.11}$$
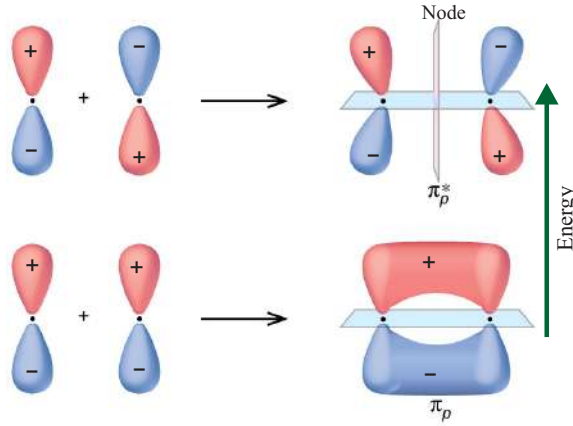
Figure 3.6: Formation of two types of π bonds. The hybridization with lower energy is the weak π state, and the hybridization with higher energy corresponds to the weak π^* bond.
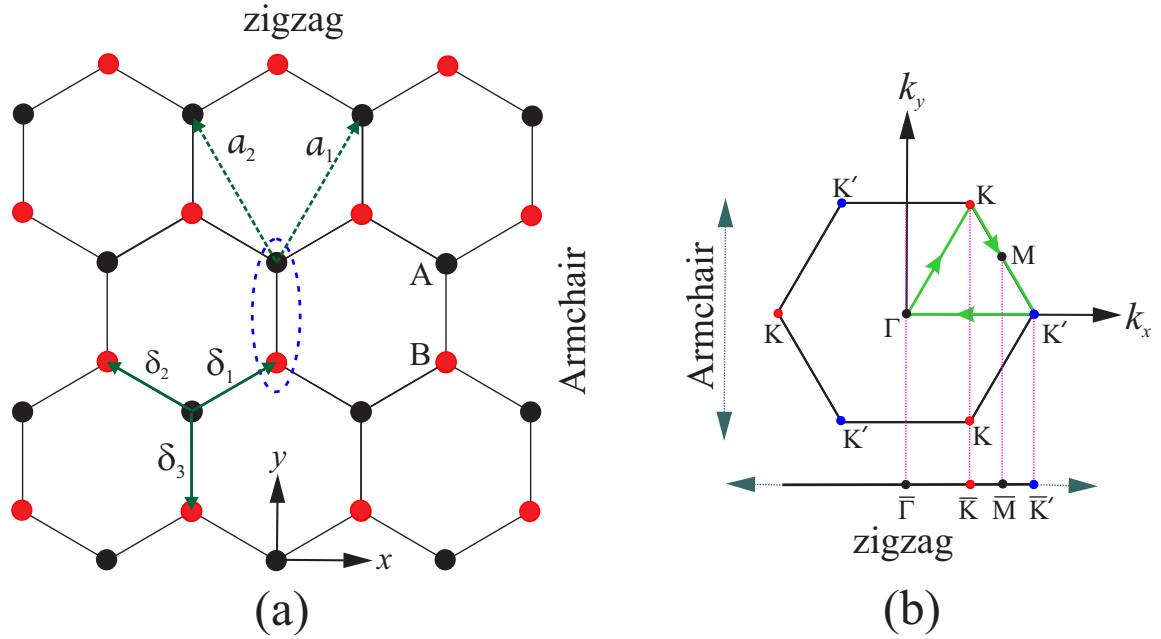
Figure 3.7: (a) The honeycomb lattice of graphene with a two-atom basis A (black sites) and B (red sites). Also shown are the basis vectors $\boldsymbol{a}_{1,2}$, the space vectors $\boldsymbol{\delta}_{1,2,3}$, and the two types of edge terminations armchair and zigzag (b) The corresponding BZ of graphene. A high-symmetry direction containing the Γ, K', M and K points is shown. Construction of 1D BZ from the 2D BZ of graphene along the zigzag edge.
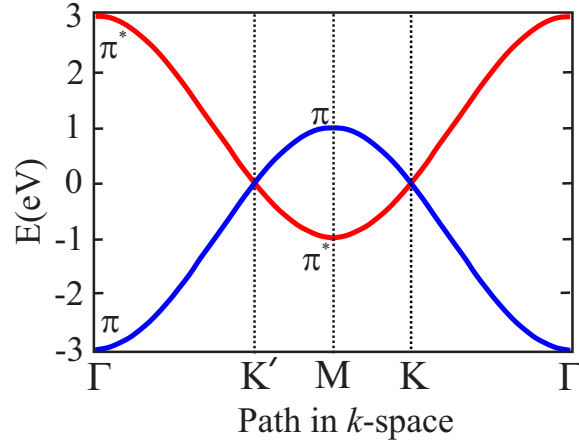
Figure 3.8: TB band structure of graphene along the high-symmetry path $\Gamma K'MK\Gamma$.

where N is the number of unit cells, $\phi(\mathbf{r} - \mathbf{R}_j^{A/B}) = \langle \phi_j^{A/B} | \mathbf{r} \rangle$ is the p_z atomic orbitals located at $\mathbf{R}_j^{A/B}$, and $\theta(\boldsymbol{k}) = -arg[f(\boldsymbol{k})]$. The $+ (-)$ sign corresponds to the eigenfunction describing the VB (CB). Thus, these eigenfunctions can be interpreted as bonding and anti-bonding states at a special $\boldsymbol{k}$ point. At Γ point, $\boldsymbol{k}$ is zero. Therefore, the eigenfunction Ψ is formed from two p_z orbitals with no relative phase so that the $+$ and $-$ signs correspond to bonding and anti-bonding states (see Fig. 3.8), respectively.

  Now, if we move from the Γ point to the boundary of the BZ, at M point, the second p_z orbital gains a π phase and actually, it flips. Therefore, as shown in Fig. 3.8, it becomes an anti-bonding case and thus a change of band ordering occurs. As seen, the corresponding bonding (π) and anti-bonding (π^*) bands disperse up and disperse down, respectively, in an opposite way. Thus, this trend of band evolution tells us that they should cross somewhere because of the above-mentioned changes in the symmetries of the eigenfunctions. These crossing points are the so-called Dirac points K and K' that are topologically different, because they are characterized by opposite Berry phases [144, 145]. As shown in Fig. 3.8 the interval between these two points is a band inverted region.

What we considered here, is actually a typical case of band inversion process. This band inversion gives rise to some consequences even without the inclusion of the spin degree of freedom. To see this, we look at the boundary where graphene is cut into nanoribbons with different edges. Now, let's project the dispersion along these edges [146]. Figure 3.7 (b) shows the construction of 1D BZ from the 2D BZ BZ of graphene. Due to the reduced dimensionality of the system, we show the corresponding points in the new BZ with an overbar. The corresponding 1D bands for two typical ribbons with zigzag and armchair edges are illustrated in Figs. 3.9(a) and (b), respectively. We first consider the zigzag case.

As shown in Fig. 3.9(b), an important consequence of the occurrence of band inversion is the appearance of some flat-band edge states in the interval of $\overline{K}$ and $\overline{K'}$ where it is a band inverted region. In the other words, the existence of metallic edge states is in close relation with the band inversion. Here, we have described the existence of zero-energy edge states qualitatively. However, the standard method to predict the existence of zero-energy edge states at different boundaries of a 2D system is the calculation of a 1D winding number [147–149].

Now, let's see what will happen for the case of an armchair edge. As shown in Fig. 3.7(b), after projecting the 2D BZ onto 1D BZ, the two K and K' points project to the same point. This results in the formation of a single Dirac cone as illustrated in Fig. 3.9(b). In fact, moving along the armchair 1D BZ does not change the bands order. Therefore, there exist no flat-band edge states.

Now, we include the SOC to see what will happen for these zero-energy bands. We solve Eq. (3.7) for a strip geometry with zigzag edges. Let's first set $\lambda_{so} = \lambda_r = \lambda_v = 0$. Due to the inclusion of the spin degree of freedom, one has spin degeneracy everywhere in the 1D energy spectrum especially for flat bands (see Fig. 3.10(a)). As shown in Fig. 3.10(b), when the SOC term λ_{so} is turned on, it induces a gap and thus the degeneracy of bands is lifted except for the points that are TRIM. Therefore, at the Γ point as a TRIM, the edge bands must touch. This means that they are protected by TRS [124–126, 128, 129]. Note that, in this system, we have two zigzag boundaries. At each edge there exist two helical edge modes. Because the system has inversion symmetry, each helical edge band is doubly degenerate as shown in Fig. 3.10(b).
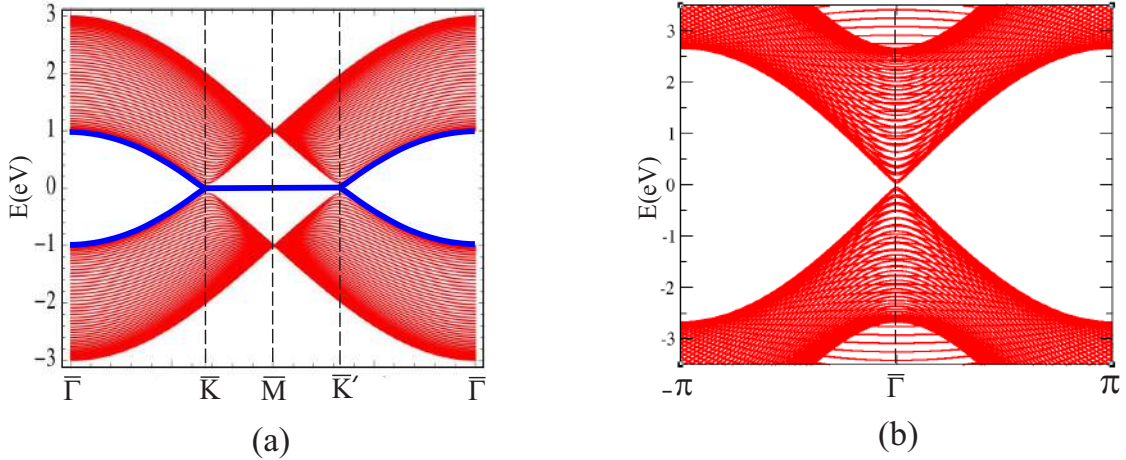
Figure 3.9: 1D energy bands for typical graphene nanoribbons with (a) zigzag and (b) armchair edges without the inclusion of spin degree of freedom.

Here, we introduced the first example for the theoretical prediction of the QSH phase pro-
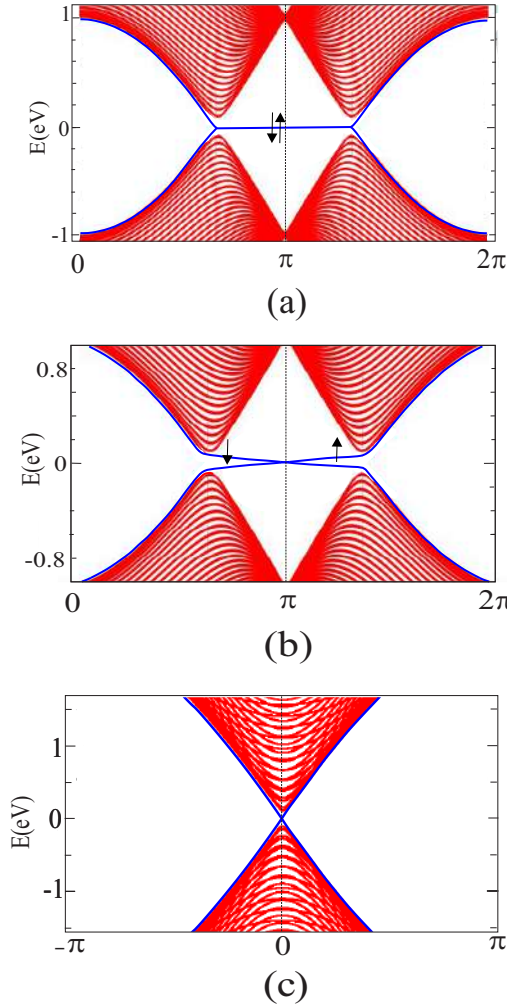
Figure 3.10: (a) 1D energy bands of a zigzag nanoribbon for $\lambda_{so} = \lambda_r = \lambda_v = 0$. There exists spin degeneracy everywhere especially for flat bands. (b) 1D energy bands of a zigzag nanoribbon for $\lambda_{so} \neq 0$ and $\lambda_r = \lambda_v = 0$. The SOC strength λ_{so} induces a gap and thus the degeneracy of bands is lifted except for the points that are TRIM. (c) 1D energy bands of an armchair nanoribbon whose bulk bands correspond to the insulating case. The appearance of helical edge states due to turning on the λ_{so} term is a purely topological effect.

posed in the initial paper of Kane and Mele on TIs with TRS [57]. The emergence of these metallic edge states is a consequence of the topology of the bulk band structure of graphene which theoretically is classified as a TI [139].

Now, we consider the case of a strip where the edges are along the armchair direction. As we know, in the absence of the SOC, the 1D spectrum of a strip geometry with an armchair edge can be either metallic or insulating depending on the width of the ribbon [150]. Here, we consider widths which correspond to the insulating case as shown in Fig. 3.9(b). Note that the reason for having the band gap in the 1D spectrum of armchair nanoribbons is the effect of quantum confinement.

As stated, we believe that graphene is a TI [139]. Thus, we expect that the helical edge states should appear at every boundary. So, the armchair edge should not be a kind of exception. If we turn on the SOC, a gap is induced at the Dirac points in the bulk spectrum. However, as shown in Fig. 3.10(c), by increasing the strength of the SOC, one can see the appearance of edge states in the corresponding armchair spectrum. This is a purely topological effect which is another demonstration for the existence of the QSH phase in graphene.

A question that might be raised here is how can we make sure that these states really have edge nature? In order to check this, one can simply plot the corresponding wavefunction in real space. Then, the behavior of the wavefunctions can show the localization of the states near the boundaries and thus establish their edge nature.

So far we have set the parameters λ_r and λ_v to be zero. This actually reduced the Kane-Mele model to two independent copies of the Haldane model [117]. However, varying these parameters allows us to define different types of phases which gives rise to the phase diagram of the Kane and Mele model [139]. The exact calculation of such phase diagrams require to define the topology of bulk bands in a quantitative manner. To this end, in what follows, we will shortly introduce the different ways to determine the topology of a band insulator. Then we will return to the Kane and Mele model in the last section of this chapter and obtain the corresponding phase diagram using the numerical method that we have utilized in this thesis.

3.3   How to distinguish a TI from a normal insulator?

In the previous section, we shortly introduced the QSHE in graphene as a basic example. However, a short yet comprehensive description of quantitative classification of TIs is desirable. On the other hand, as a first step toward paving the way for practical applications, the material realization of TIs with desired physical properties is of crucial importance [92, 122–132]. Thus, the search for theoretical prediction of new candidate materials for TIs is of great significance. As stated, there exist several ways to determine the band topology of a crystal, and to predict whether it is a TI. In what follows, we proceed by giving a brief review of the ways to distinguish a TI from a normal insulator.

3.3.1 Bulk-boundary correspondence

Previously we used the appearance of helical edge states at the boundaries of graphene nanoribbons to demonstrate the QSH phase in graphene. This is related to a concept which is called bulk-boundary correspondence [128, 129]. The bulk-boundary correspondence establishes a connection between the topology of bulk bands and the multiplicities of gapless edge states at the boundary of the system [128, 129]. The classical example of bulk-boundary correspondence is the existence of gapless chiral edge states at the interface between an IQH system and vacuum [151]. We also conclude from this correspondence that a 2D/3D TR invariant TI has topologically protected edge/surface states [125]. Therefore, based on this correspondence, one way to determine whether an insulator has non-trivial topology is to check the existence of gapless edge/surface states in the spectrum associated with the boundary of a TR invariant system [125]. To be more explicit, we now consider a generic TR-invariant 2D insulator and show the distinct non-trivial bulk insulating phases by looking at different possible configurations of edge states at the boundary of the system. TRS as a fundamental symmetry leads to some consequences in the energy spectrum of the system. As shown in Fig. 3.2(a), there are four TRIM in the corresponding BZ of a simple rectangular lattice. Since the degeneracy at these special points is protected by TRS, a perturbation that preserves this symmetry, can not break the degeneracy.

Schematic representations of the energy spectrum for a 1D TR invariant strip are shown in Figs. 3.11. The shown edge states belong to only one boundary. As seen, the points $k = 0$ and $k = \pi/a$ are TRIM where the energy levels must be degenerate (see Figs. 3.11(a)). If we look at mid-gap states, by going away from TRIM points, the degeneracy is lifted due to SOC. There are three options to connect the mid-gap states at $k = 0$ and $k = \pi/a$: The first way is to connect the two Kramers degenerate edge states at $k = 0$ to the same Kramers pairs at $k = \pi/a$ (Fig. 3.11(b)). In this case, there are even number of Kramer pairs at every energy within the mid-gap region. One can easily check that using an edge potential or TR invariant perturbation which does not close the bulk energy gap, these edge modes are pushed completely into the bulk spectrum. So, this case corresponds to a topologically trivial insulator. The second way of pairing is shown in Fig. 3.11(c). Since there exists no fundamental symmetry to protect the level crossing at point s, a small TR invariant perturbation can lift its degeneracy and reduce it to the first type of pairing. Thus, this case also corresponds to a trivial insulator. The third case is a zigzag way. One can connect the two Kramers degenerate edge states at $k = 0$ to two different Kramers pairs at $k = \pi/a$ from the valence band to the conduction band (Fig. 3.11(d)). In this case, if one count the number of the right moving states and the left moving states within the energy gap, it always gives an odd number. These edge states are robust and can not be eliminated using an edge potential or any other TR invariant perturbation that does not close the bulk
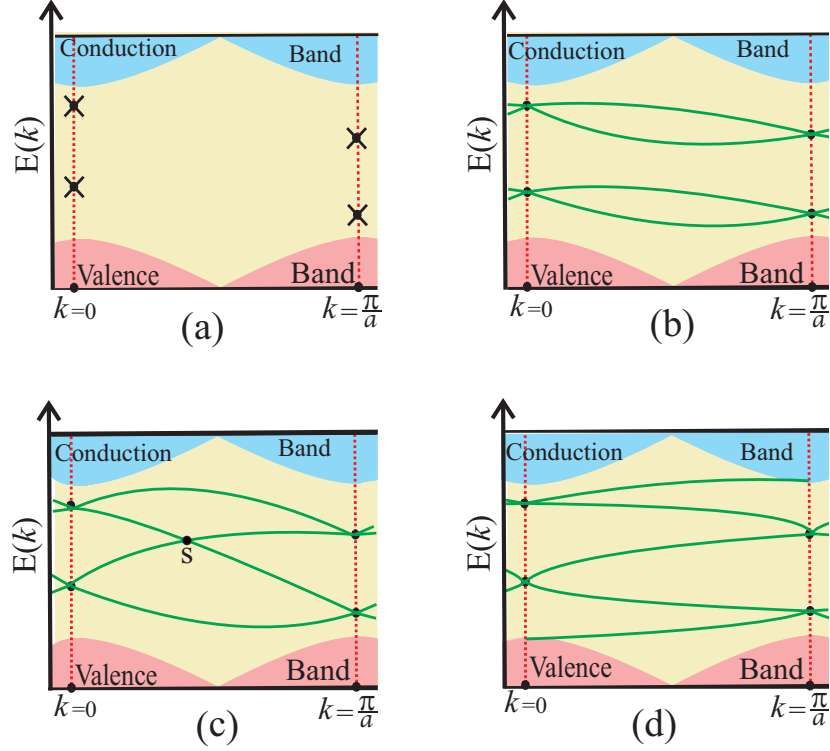
Figure 3.11: Schematic edge spectrum of a 2D band insulator. The bulk-boundary correspondence provides a way for understanding the $\mathbb{Z}_2$ classification of band insulators. (a) The points $k = 0$ and $k = \pi/a$ are TRIM where the energy levels must be degenerate. Away from these points the degeneracy is lifted due to SOC. There are three options to connect the mid-gap states: (b) The first way is to connect the two Kramers degenerate edge states at $k = 0$ to the same Kramers pairs at $k = \pi/a$. (c) The second way of pairing. Since there exists no fundamental symmetry at point s, it is topologically equivalent with the first way of pairing. (d) The third way is a zigzag method. One can connect the two Kramers degenerate edge states at $k = 0$ to two different Kramers pairs at $k = \pi/a$ going from the valence band to the conduction band.

energy gap. So, this case corresponds to a topologically non-trivial phase which is called a QSH phase.

Therefore, the existence of two and only two topologically different ways to connect the two Kramers degenerate edge states at $k = 0$ and $k = \pi/a$, implies the existence of two distinct topological phases in a 2D insulating system which are called even or odd $\mathbb{Z}_2$ class. Since 2006, independent theoretical studies [59, 152, 153] discovered that there exists a natural generalization from a QSH insulator to a 3D counterpart which is called 3D TI.

This is different from the QHE, which is limited only to 2D systems. The existence of surface states on a surface of a 3D TI is the higher-dimensional analogy of 1D edge states at the border of a 2D TI. We shall exemplify this subject by considering the case of a BZ with cuboid shape. As shown in Fig. 3.2(b), there are eight distinct TRIM in the BZ of a simple orthorhombic lattice, which are defined by reciprocal lattice vectors as $\mathbf{\Gamma}_{i=(n_1 n_2 n_3)} = (n_1 \mathbf{G}_1 + n_2 \mathbf{G}_2 + n_3 \mathbf{G}_3)/2$, with $n_j = 0, 1$ [59]. Similarly, at these points, the energy spectrum must be degenerate due to Kramers theory. This gives rise to the formation of Dirac-like 2D states at a surface of a 3D band insulator. To characterize the non-trivial topology of a 3D TI, a similar manner to the bulk-boundary correspondence is useful [154]. Suppose that we consider the corresponding surface sates in the (k_x, k_y)-plane. This corresponds to open boundary conditions perpendicular to the z-axis. As shown in Fig. 3.12(a), four TRIM points $\mathbf{\Gamma}_{000}$, $\mathbf{\Gamma}_{100}$, $\mathbf{\Gamma}_{010}$, $\mathbf{\Gamma}_{110}$ lie in the (k_x, k_y)-plane. Figures 3.12(b) and (c) show the previously described two topologically non-equivalent ways of connecting edge states along the k_x and k_y axes. Clearly, to have a surface state one needs to make a connection for both k_x and k_y directions. Therefore, the ways that (b) and (c) types of connections are used for both directions lead to three general classifications: If one connects both directions via (c) type, it leads to a strong TI. If the connection is done via both (b) and (c) types, then one gets a weak topological insulating phase. Finally, when a (c)-type of connection is used for both directions, we obtain a trivial insulating phase.

It is very important to note that, there exist an odd number of surface Dirac cones for a strong TI, while in the case of a weak TI, one always see an even number of surface Dirac cones [59]. This is a direct consequence of the number of band inversions in the bulk energy spectrum [155].

3.3.2 Adiabatic continuity

Adiabatic continuity principle is a possible approach to characterize a topological phase transition [137, 141, 142]. Based on this principle, two band insulator systems belong to distinct topological classes, if there exists no adiabatic path to connect the Hamiltonian of a band insulator into one another without closing the band gap [137, 141, 142]. Therefore, if one can slowly change the band structure of a band insulator to that of another by some controlling parameters, then they are topologically equivalent. For example, one can show using the adiabatic continuity that, a material is a band insulator [137]. Because the atomic limit is a known topological state, finding an adiabatic connection between the Hamiltonian of the material and this known phase establishes that it is an ordinary band insulator [137]. Figure 3.4 shows the schematic band structure of a band insulator obtained by continuous deformation of the corresponding energy levels of atomic level. However,
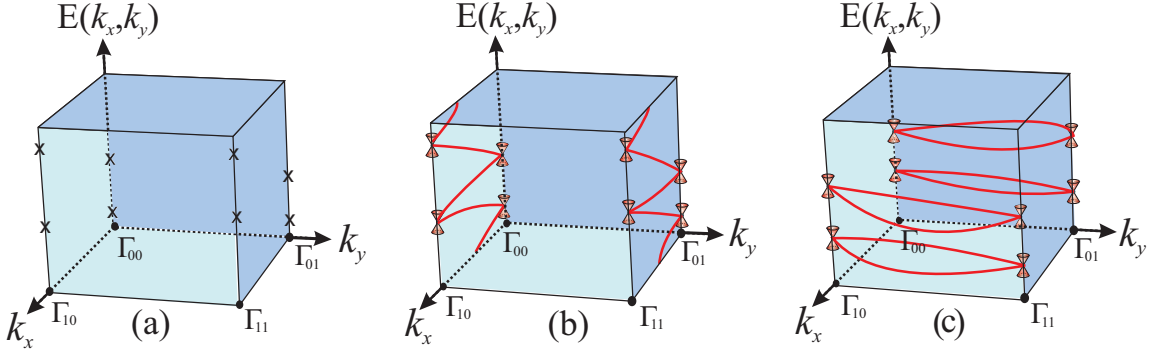
Figure 3.12: Schematic surface spectrum of a 3D band insulator in the mid-gap region assuming open boundary conditions is perpendicular to the z-axis. A similar manner to the bulk-boundary correspondence provides a way for understanding the $\mathbb{Z}_2$ classification of 3D band insulators. (a) four TRIM points $\mathbf{\Gamma}_{000}$, $\mathbf{\Gamma}_{100}$, $\mathbf{\Gamma}_{010}$ and $\mathbf{\Gamma}_{110}$ lie in the (k_x, k_y)-plane. (b) and (c) show the previously described two topologically non-equivalent ways of connecting edge states along the k_x and k_y axes. The ways that (b) and (c) types of connections are used for both directions can lead to a NI, a weak TI, or a strong TI.

continuously deforming of the topologically known spectrum Fig. 3.4 (a) to the topologically unknown spectrum Fig. 3.4 (b), requires many intermediate calculations. Therefore, this approach is computationally demanding, which limits most of its applications [141].

3.3.3 Computing the $\mathbb{Z}_2$ invariant

As previously discussed, in the presence of the TRS, the Hall conductance is zero. This means that the Chern number is not a suitable invariant for dividing systems with TR symmetry class [139]. In 2005, Kane and Mele proposed a new way for the classification of a time reversal symmetric system by introducing a new topological invariant (ν) [139]. They showed that this topological classification which is called a $\mathbb{Z}_2$-classification, is used to distinguish a QSH insulator from a normal insulator. Based on this classification, we find that all time reversal invariant 2D band insulators can be divided into two distinct categories: $\nu = 0$ for a normal insulator and $\nu = 1$ for a QSHI [139]. According to this classification, a 3D band insulator falls into three general categories: an ordinary insulating phase, a weak topological insulating phase, and a strong topological insulating phase [59]. Therefore, the most straightforward method for determining the topological nature of a TR band insulator is computing the $\mathbb{Z}_2$ invariant. Note that, this invariant characterizes the topology of the bulk band structure, and the calculations are done over the corresponding BZ.

There are several equivalent ways of computing the $\mathbb{Z}_2$ invariant [126, 128, 129, 156]. Here, we briefly review the most commonly used ways to determine the $\mathbb{Z}_2$ invariant in 2D and 3D band insulators.

2D band insulators

We start with introducing the sewing matrix [157]

$$w_{mn}(\boldsymbol{k}) = \langle u_m(-\boldsymbol{k})|\Theta|u_n(\boldsymbol{k})\rangle. \tag{3.12}$$

By using equation

$$|u_m(-\boldsymbol{k})\rangle = \sum_n w^*_{mn}(\boldsymbol{k})\,\Theta\,|u_n(\boldsymbol{k})\rangle, \tag{3.13}$$

one can easily show that

$$\sum_m w^\dagger_{lm}(\boldsymbol{k})w_{mn}(\boldsymbol{k}) = \langle u_n(\boldsymbol{k})|u_l(\boldsymbol{k})\rangle = \delta_{nl}. \tag{3.14}$$

This equation implies that $w_{mn}(\boldsymbol{k})$ is a unitary matrix [157]. Equations (3.13) and (3.14) lead to the following property

$$w_{nm}(-\boldsymbol{k}) = -w_{mn}(\boldsymbol{k}), \tag{3.15}$$

which means that at a TRIM Γ_i, w matrix becomes antisymmetric, i.e.

$$w_{nm}(\boldsymbol{\Gamma_i}) = -w_{mn}(\boldsymbol{\Gamma_i}). \tag{3.16}$$

We consider $2N$ occupied bands which form N Kramers pairs. Therefore the matrix w can be divided into N pairs whose elements are denoted by $w^{I,II}_{mn}(\boldsymbol{k})$. Using relations (3.36) we have

$$
\begin{aligned}
w^{I,II}_{mn}(\boldsymbol{k}) = & \quad \langle u_{m,I}(-\boldsymbol{k})|\Theta|u_{n,II}(\boldsymbol{k})\rangle = \delta_{mn}e^{-i\chi(\boldsymbol{k},n)} \\
w^{II,I}_{mn}(\boldsymbol{k}) = & \quad \langle u_{m,II}(-\boldsymbol{k})|\Theta|u_{n,I}(\boldsymbol{k})\rangle = -\delta_{mn}e^{-i\chi(-\boldsymbol{k},n)}.
\end{aligned} \tag{3.17}
$$

Therefore, the representation of matrix w at Γ_i is

$$
w(\boldsymbol{\Gamma}_i) = \begin{pmatrix}
0 & e^{-i\chi(\boldsymbol{\Gamma}_i,1)} & 0 & 0 & \cdots \\
-e^{-i\chi(\boldsymbol{\Gamma}_i,1)} & 0 & 0 & 0 & \cdots \\
0 & 0 & 0 & e^{-i\chi(\boldsymbol{\Gamma}_i,2)} & \cdots \\
0 & 0 & -e^{-i\chi(\boldsymbol{\Gamma}_i,2)} & 0 & \cdots \\
\vdots & \vdots & \vdots & \vdots & \ddots
\end{pmatrix}. \tag{3.18}
$$

This is a $2N \times 2N$ skew-symmetric tridiagonal matrix, which allows us to define Pfaffian for it [157]. The Pfaffian of such matrices are related to the determinant by

$$\mathrm{Pf}[w]^2 = \mathrm{Det}[w], \tag{3.19}$$

and for matrix (3.18) is obtained as follows [157]

$$\mathrm{Pf}[w(\mathbf{\Gamma}_i)] = w_{11}^{I,II}(\mathbf{\Gamma}_i) w_{22}^{I,II}(\mathbf{\Gamma}_i) \dots w_{N-1N-1}^{I,II}(\mathbf{\Gamma}_i) w_{NN}^{I,II}(\mathbf{\Gamma}_i) = e^{-i \sum_{n=1}^{N} \chi(\mathbf{\Gamma}_i, n)}. \tag{3.20}$$

By using the modern theory of charge polarization [158], Fu and Kane [138] showed that the topological invariant ν is related to the Pfaffian of matrix w as

$$(-1)^\nu = \prod_{i=1}^{4} \frac{\mathrm{Pf}[w(\mathbf{\Gamma}_i)]}{\sqrt{\mathrm{Det}[w(\mathbf{\Gamma}_i)]}}. \tag{3.21}$$

We define the function $\delta(\mathbf{\Gamma}_i)$ at these four TRIM as

$$\delta(\mathbf{\Gamma}_i) = \frac{\mathrm{Pf}[w(\mathbf{\Gamma}_i)]}{\sqrt{\mathrm{Det}[w(\mathbf{\Gamma}_i)]}}, \tag{3.22}$$

which using relation (3.19) only takes values ± 1. Thus we rewrite the topological invariant (3.21) for a 2D system as

$$(-1)^\nu = \prod_{i=1}^{4} \delta(\mathbf{\Gamma}_i), \tag{3.23}$$

which classifies 2D band insulators into topological ($\nu = 1$) and trivial ($\nu = 0$) ones.

Although this equation seems to require only a knowledge of the occupied cell-periodic eigenfunctions at four TRIM, it also needs a globally smooth gauge choice throughout the whole BZ, which makes it usually inappropriate for computational implementation [125, 156, 159]. Therefore, developing (almost) gauge-independent methods to calculate the $\mathbb{Z}_2$ invariant is more favorable [156]. However, the derivation of this formulation had a central role, since it paved the way for the extension to higher dimensions [59].

It was shown that the problem of globally smooth gauge choice can be avoided if the system has an extra symmetry [125]. For example, if perpendicular spin s_z is a good quantum number, then one can define the independent first Chern numbers $c_\uparrow$ and $c_\downarrow$. Since the system has TRS, we have $c_\uparrow + c_\downarrow = 0$. However, the spin-Chern number $c_\sigma = c_\uparrow - c_\downarrow$ is quantized and gives the $\mathbb{Z}_2$ invariant via [160].

$$\nu = c_\sigma \,\mathrm{mod}2. \tag{3.24}$$

It is to be noted that, though $c_\uparrow$ and $c_\downarrow$ become meaningless in the presence of spin non-conserving Rashba terms, the spin-Chern number c_σ is well defined [160–162].

In a system with inversion symmetry, computing the $\mathbb{Z}_2$ invariant becomes a greatly simplified procedure [137]. Fu and Kane [137] showed that there exists a simple formula to calculate $\delta(\boldsymbol{\Gamma}_i)$ as

$$\delta(\boldsymbol{\Gamma}_i) = \prod_{m=1}^{N} p_{2m}(\boldsymbol{\Gamma}_i), \tag{3.25}$$

where $p_{2m}(\boldsymbol{\Gamma}_i)$ is the eigenvalue of the parity of states at TRIM $\boldsymbol{\Gamma}_i$ for mth Kramers partner. Hence, Eq. (3.32) can be rewritten as

$$(-1)^\nu = \prod_{i=1}^{4} \prod_{m=1}^{N} p_{2m}(\boldsymbol{\Gamma}_i). \tag{3.26}$$

As proposed in the early work of Fu and Kane [138], the $\mathbb{Z}_2$ invariant can also be formulated as an obstruction against defining a globally smooth gauge. They showed that an equivalent method to calculate the $\mathbb{Z}_2$ invariant is as an integral over half the BZ which is given by

$$\nu = \frac{1}{2\pi i} \left[\oint_{\partial \text{HBZ}} d\boldsymbol{k} \cdot \boldsymbol{\mathcal{A}}(\boldsymbol{k}) - \int_{\text{HBZ}} d^2 k \mathcal{F}(\boldsymbol{k}) \right] (\text{mod } 2), \tag{3.27}$$

where HBZ denotes half the BZ. The central quantities are the Berry gauge potential

$$\boldsymbol{\mathcal{A}}(\boldsymbol{k}) = \sum_{n} \langle u_n(\boldsymbol{k}) | \nabla_n u_n(\boldsymbol{k}) \rangle, \tag{3.28}$$

and the Berry field strength

$$\mathcal{F} = \nabla_{\mathbf{k}} \times \mathcal{A}(\boldsymbol{k}) \mid_z, \tag{3.29}$$

where $u_n(\boldsymbol{k})$ is the periodic part of the Bloch state with band index n and the summation runs over all occupied states. According to Stoke's theorem, it is obvious that if $\boldsymbol{\mathcal{A}}$ and $\mathcal{F}$ have the same gauge which is smooth over HBZ, the result will vanish [138]. Therefore, one needs to fix the gauge with some additional constraints [138, 163]. Starting from Eq. (3.27), Fukui *et al.* derived an efficient formula for computing the $\mathbb{Z}_2$ invariant for a lattice BZ which is (almost) gauge-independent, though it requires a TR adapted gauge at the boundary of half of the BZ [115, 156]. By choosing a gauge, in which the corresponding states fulfills the TRS constraints in addition to the periodicity of the k points, that are related by a reciprocal lattice $\boldsymbol{G}$, the gauge fixing procedure is complete and the returned results of $\nu = 0$ and $\nu = 1$ represents the trivial and topological phases, respectively.

3D band insulators

The introduced generalization of a QSH insulator to a 3D TI in Sec. (3.3.1) is a milestone in the development of TIs. As noted, the extension to three dimension defines an insulating bulk and conducting surface states. Fu, Kane and Mele [59] first made the connection between the topology of the mentioned insulating bulk and surface states by generalizing the $\mathbb{Z}_2$ invariant to three dimensions. In a 3D band insulator with TRS, there are eight distinct TRIM in the BZ, which define six planes with corresponding $\mathbb{Z}_2$ invariants. However, since some planes share two TRIMs, the corresponding topological $\mathbb{Z}_2$ invariants are not independent [152]. As a generalization, they [59] suggested that the topological nature of a 3D band insulator can be characterized by four independent topological invariants $(\nu_0; \nu_1\nu_2\nu_3)$. Again, similar to Eq. (3.22) the function $\delta(\mathbf{\Gamma}_{n1,n2,n3})$ at eight TRIM is defined as

$$\delta(\mathbf{\Gamma}_{n1,n2,n3}) = \frac{\text{Pf}[w(\mathbf{\Gamma}_{n1,n2,n3})]}{\sqrt{\text{Det}[w(\mathbf{\Gamma}_{n1,n2,n3})]}}. \tag{3.30}$$

Using this definition, the four independent $\mathbb{Z}_2$ invariants are given by

$$(-1)^{\nu_0} = \prod_{n1,n2,n3=0,1} \delta(\mathbf{\Gamma}_{n1,n2,n3}) \tag{3.31}$$

$$(-1)^{\nu_i} = \prod_{n_j \neq n_i = 0,1; n_i = 1} \delta(\mathbf{\Gamma}_{n1,n2,n3}) \quad (i = 1, 2, 3). \tag{3.32}$$

It follows from these equations that a 3D band insulator falls into three general categories [59]: if all four topological invariants are zero, then the system is a trivial insulator. The system is called a strong TI when $\nu_0 = 1$, where there are an odd number of Dirac cones on all surface of the system. And it is called a weak TI when $\nu_0 = 0$ and at least one of the invariants $\nu_i(1, 2, 3)$ is nonzero. In this case there is an even number of Dirac cones on the surfaces [59, 129].

3.3.4 Topological quantum chemistry: the most recent approach

The approaches of quantum physics and quantum chemistry to treat the electronic band structure of a material are different. The physics approach is based on the extended electronic states, while chemistry deals with the problem via locally looking at the orbital bonds in real space. However, finding an interface between chemistry and physics can provide a better understanding of electronic properties of materials. In other words, the answer to the question what chemistry does tell us about the universal properties of the

system, can remedy the disconnection between chemistry and physics. There are some properties that can be universal due to the existence of a fundamental symmetry. For example, the number of energy bands and the ways that they are connected to each other at special momenta can be universal properties. So, the point in question is that how can we derive directly these properties using real space chemistry?

The connection between chemical orbitals of elements in real space and the band theory in momentum space was proposed first by Zak in 1980 [164]. Utilizing the elementary band representations as mathematical vehicles [165], Zak made the link between the orbital representation of electrons that sit in lattice sites and the corresponding energy bands in momentum space [165, 166]. He introduced his theory for spinless systems, with and without TR symmetry.

A recent seminal paper by Bradlyn *et al.* [167], has extended the Zak's theory to the double spinful groups in the presence of TR. The theory exploits the concept of elementary band representations to provide criteria for determining the topological nature of band structures. In other words, it classifies the universal global properties of all possible band structures and materials using group theory [167]. Indeed, their work is a revolutionary theory for topological quantum chemistry which is the newest formalism to predict novel topological phases of materials. For all 230 crystal symmetry groups, they classified the possible energy spectra that arise from local atomic orbitals, and showed which are topologically non-trivial [167]. This is a very strong theory that tells one how materials can exist from the topological point of view.

Since the novelty of the approach, it is out of the scope of this thesis. We refer to a series of related papers [166–170] that will allow the reader to obtain the latest information in the field.

3.4 Lattice computation of $\mathbb{Z}_2$ invariant

From a numerical point of view, finding the $\mathbb{Z}_2$ invariant requires to do calculations on a set of discrete points chosen appropriately within the BZ [115]. As mentioned in Sec. (3.3.3), Fukui *et al.* derived an efficient formula for lattice computation of $\mathbb{Z}_2$ invariant which is (almost) gauge-independent [115, 156]. That is to say, it only requires a TR adapted gauge at the boundary of half of the BZ [115, 156]. This numerical method is very convenient to implement in TB models even in realistic models of 3D systems [115, 159].

To see how this algorithm is implemented, we consider the corresponding BZ of a rectangular lattice as shown in Fig. 3.13. We then mesh the BZ so that each site of the lattice is defined by

$$k_l = \frac{1}{2}(\frac{j_1}{N_1}G_1, \frac{j_2}{N_2}G_2), \qquad (j_{1(2)} = -N_{1(2)}, \ldots, N_{1(2)}), \qquad (3.33)$$

where $G_{1(2)}$ is a reciprocal lattice constant, $N_{1(2)}$ is a positive integer, and l specifies the lth plaquette. As stated before, the Berry field strength $\mathcal{F}$ is gauge-invariant, but the Berry potential $\mathcal{A}$ is not [90]. Therefore, any arbitrary choice of gauge for $\mathcal{F}$ is relevant and the gauge fixing procedure should only be done for $\mathcal{A}$. In other words, the formula 3.27 for ν is made meaningful when a choice of gauge for the corresponding eigenfunctions at the boundary of half of the BZ is considered.

The gauge fixing procedure is as follows: we have divided the boundary of half of the BZ into six segments as labeled from 1 to 6, where each segment is separated from others by TRIM as shown in Fig. 3.13. Since the points on the segment 6 ($\boldsymbol{k}_l' \in 6$) are the periodic image of those on the segment 5 ($\boldsymbol{k}_l' = \boldsymbol{k}_l + \boldsymbol{G}_1$, $\boldsymbol{k}_l \in 5$), the periodic gauge [137] implies

$$|u_n(\boldsymbol{k}_l + \boldsymbol{G}_1)\rangle = e^{-i\boldsymbol{G}_1 \cdot \boldsymbol{r}}|u_n(\boldsymbol{k}_l)\rangle. \tag{3.34}$$

Therefore, the contributions of the segments 5 and 6 to the integral of $\mathcal{A}$ over HBZ cancel out. We accept an arbitrary gauge choice along the segments 1 and 3, for example, the output of our numerical calculations for Bloch eigenfunctions [163]. Then, according to the TR constraint, the corresponding states of a Kramers pairs along the segments 2 and 4 are constructed, and the translational phase factors must be properly considered. The points on the segment 2 ($-\boldsymbol{k}_l \in 2$) are directly the TR partners of those on the segment 1 ($\boldsymbol{k}_l \in 1$). Then the states at $-\boldsymbol{k}_l$ are constrained as

$$\begin{aligned} |u_{n,I}(-\boldsymbol{k}_l)\rangle &= \quad \Theta|u_{n,II}(\boldsymbol{k}_l)\rangle \\ |u_{n,II}(-\boldsymbol{k}_l)\rangle &= \quad -\Theta|u_{n,I}(\boldsymbol{k}_l)\rangle. \end{aligned} \tag{3.35}$$

The points on the segment 4 ($\boldsymbol{k}_l' \in 4$) are the periodic image of the points which are the TR partners of those on the segment 3 ($\boldsymbol{k}_l' = -\boldsymbol{k}_l + \boldsymbol{G}_2$, $-\boldsymbol{k}_l \in 4'$, $\boldsymbol{k}_l \in 3$). Thus, the states at $\boldsymbol{k}_l' \in 4$ are constrained as

$$\begin{aligned} |u_{n,I}(-\boldsymbol{k}_l + \boldsymbol{G}_2)\rangle &= \quad e^{-i\boldsymbol{G}_2 \cdot \boldsymbol{r}}\Theta|u_{n,II}(\boldsymbol{k}_l)\rangle \\ |u_{n,II}(-\boldsymbol{k}_l + \boldsymbol{G}_2)\rangle &= \quad -e^{-i\boldsymbol{G}_2 \cdot \boldsymbol{r}}\Theta|u_{n,I}(\boldsymbol{k}_l)\rangle. \end{aligned} \tag{3.36}$$

Finally, at the special points Γ_1, Γ_2, Γ_3 and Γ_4, we accept an arbitrary gauge for state $|u_{n,I}(\Gamma_i)\rangle$ and enforce the constraint

$$|u_{n,II}(\Gamma_i)\rangle = -\Theta|u_{n,I}(\Gamma_i)\rangle, \tag{3.37}$$

and the states at Γ_5 and Γ_6 are constructed via

$$|u_n(\Gamma_{5(6)})\rangle = e^{i\boldsymbol{G}_1 \cdot \boldsymbol{r}}|u_n(\Gamma_{3(2)})\rangle. \tag{3.38}$$
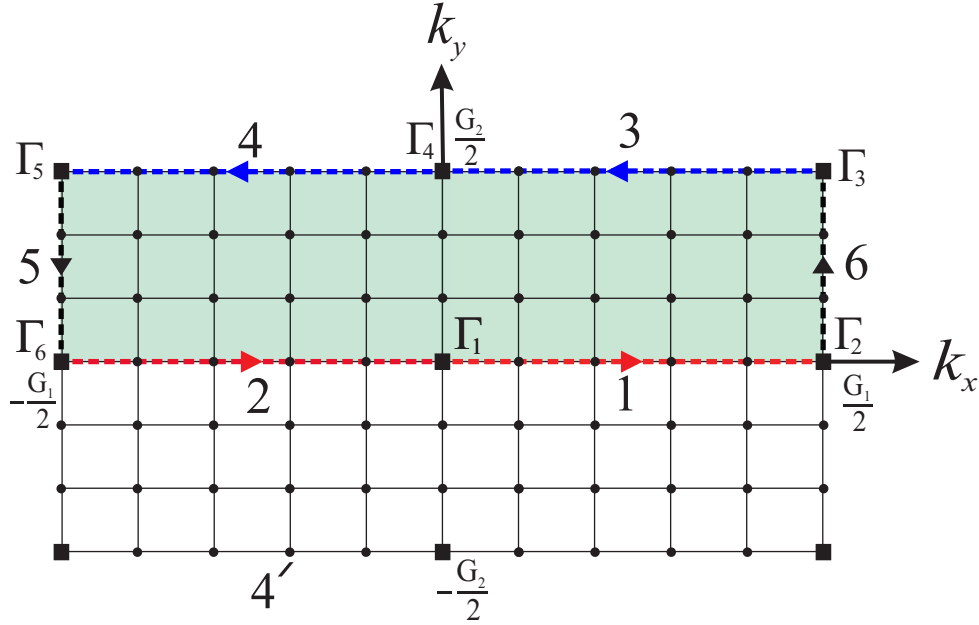
Figure 3.13: The lattice mesh on the BZ of a rectangular lattice. The division of the boundary of half of the BZ into six segments as labeled from 1 to 6.

Now we can use the new obtained set of eigenfunctions to compute the $\mathbb{Z}_2$ invariant. The discretized BZ version [115] of Eq. (3.27) for numerical computing the $\mathbb{Z}_2$ invariant, is written as

$$\nu = \frac{1}{2\pi i} \left[\sum_{k_l \in \partial \text{HBZ}} A_x(k_l) - \sum_{k_l \in \text{HBZ}} F_{xy}(k_l) \right] (\text{mod } 2), \tag{3.39}$$

where $A_x(k_l)$ and $F_{xy}(k_l)$ are the modified non-Abelian Berry connection and Berry curvature in Eqs. (3.28) and (3.29), respectively. These modified quantities are defined as

$$A_x(k_l) = \ln U_x(k_l), \tag{3.40}$$

$$F_{xy}(k_l) = \ln \frac{U_x(k_l)U_y(k_l + \hat{x})}{U_y(k_l)U_x(k_l + \hat{y})}, \tag{3.41}$$

where the so-called unimodular link variable $U_\mu(k_l)$ is given by [115]

$$U_\mu(k_l) = \frac{\det \psi^\dagger(k_l)\psi(k_l + \hat{\mu})}{|\det \psi^\dagger(k_l)\psi(k_l + \hat{\mu})|}. \tag{3.42}$$

Here, $\hat{\mu}$ denotes a unit vector in x-y plane as shown in Fig. 3.13. Note that the Berry potential and Berry field strength are both defined within the branch of $A_x(k_l)/i \in (-\pi, \pi)$

and $F_{xy}(k_l)/i \in (-\pi, \pi)$ [115].

In what follows, we compare some results obtained by the numerical implementation of this method with analytic results in order to demonstrate the validity of our algorithm.

3.4.1 $\mathbb{Z}_2$ invariants for the Kane and Mele Model

Let us again start with the Kane and Mele model Hamiltonian (3.7). The Fourier transform of the preceding Hamiltonian gives the general Bloch Hamiltonian in momentum space as

$$H = \sum_{\boldsymbol{k}} \psi_{\boldsymbol{k}}^{\dagger} H_{\boldsymbol{k}} \psi_{\boldsymbol{k}}, \tag{3.43}$$

where we have used the basis spinor $\psi_{\boldsymbol{k}}^{\dagger} = \{\psi_{A\uparrow}^{\dagger}, \psi_{B\uparrow}^{\dagger}, \psi_{A\downarrow}^{\dagger}, \psi_{B\downarrow}^{\dagger}\}$ with $H_{\boldsymbol{k}}$ being

$$H_{\boldsymbol{k}} = \begin{pmatrix} H_{\boldsymbol{k}}(\uparrow\uparrow) & H_{\boldsymbol{k}}(\uparrow\downarrow) \\ H_{\boldsymbol{k}}(\downarrow\uparrow) & H_{\boldsymbol{k}}(\downarrow\downarrow) \end{pmatrix}, \tag{3.44}$$

where each block is a 2×2 matrix and are given by

$$\begin{aligned} H_{\boldsymbol{k}}(\uparrow\uparrow) &= H_{\boldsymbol{k}}^0 + H_{\boldsymbol{k}}^{\lambda_\nu} + H_{\boldsymbol{k}}^{\lambda_{so}}, \\ H_{\boldsymbol{k}}(\downarrow\downarrow) &= H_{\boldsymbol{k}}^0 + H_{\boldsymbol{k}}^{\lambda_\nu} - H_{\boldsymbol{k}}^{\lambda_{so}}, \\ H_{\boldsymbol{k}}(\uparrow\downarrow) &= H_{\boldsymbol{k}}^{\lambda_r}, \quad H_{\boldsymbol{k}}(\downarrow\uparrow) = H_{\boldsymbol{k}}^{\lambda_r \dagger}. \end{aligned} \tag{3.45}$$

Using the lattice vectors shown in Fig. 3.7, the matrices $H_{\boldsymbol{k}}^0$, $H_{\boldsymbol{k}}^{\lambda_\nu}$, $H_{\boldsymbol{k}}^{\lambda_{so}}$ and $H_{\boldsymbol{k}}^{\lambda_r}$ are explicitly represented as

$$\begin{aligned} H_{\boldsymbol{k}}^0 &= \begin{pmatrix} 0 & f(\boldsymbol{k}) \\ f^*(\boldsymbol{k}) & 0 \end{pmatrix}, \\ H_{\boldsymbol{k}}^{\lambda_\nu} &= \begin{pmatrix} \lambda_\nu & 0 \\ 0 & -\lambda_\nu \end{pmatrix}, \\ H_{\boldsymbol{k}}^{\lambda_{so}} &= \begin{pmatrix} g(\boldsymbol{k}) & 0 \\ 0 & -g(\boldsymbol{k}) \end{pmatrix}, \\ H_{\boldsymbol{k}}^{\lambda_r} &= \begin{pmatrix} 0 & h(\boldsymbol{k}) \\ i(\boldsymbol{k}) & 0 \end{pmatrix}, \end{aligned} \tag{3.46}$$

where

$$\begin{aligned} f(\boldsymbol{k}) &= t[e^{i\boldsymbol{k}\cdot\boldsymbol{a_1}} + e^{i\boldsymbol{k}\cdot\boldsymbol{a_2}} + 1], \\ g(\boldsymbol{k}) &= 2\lambda_{so}[-\sin(\boldsymbol{k}\cdot\boldsymbol{a_1}) + \sin(\boldsymbol{k}\cdot\boldsymbol{a_2}) - \sin(\boldsymbol{k}\cdot(\boldsymbol{a_2}-\boldsymbol{a_1}))], \\ h(\boldsymbol{k}) &= i\lambda_r[e^{i(\boldsymbol{k}\cdot\boldsymbol{a_1}+\frac{\pi}{3})} + e^{i(\boldsymbol{k}\cdot\boldsymbol{a_2}-\frac{\pi}{3})} - 1], \\ i(\boldsymbol{k}) &= -i\lambda_r[e^{-i(\boldsymbol{k}\cdot\boldsymbol{a_1}-\frac{\pi}{3})} + e^{-i(\boldsymbol{k}\cdot\boldsymbol{a_2}+\frac{\pi}{3})} - 1]. \end{aligned} \tag{3.47}$$
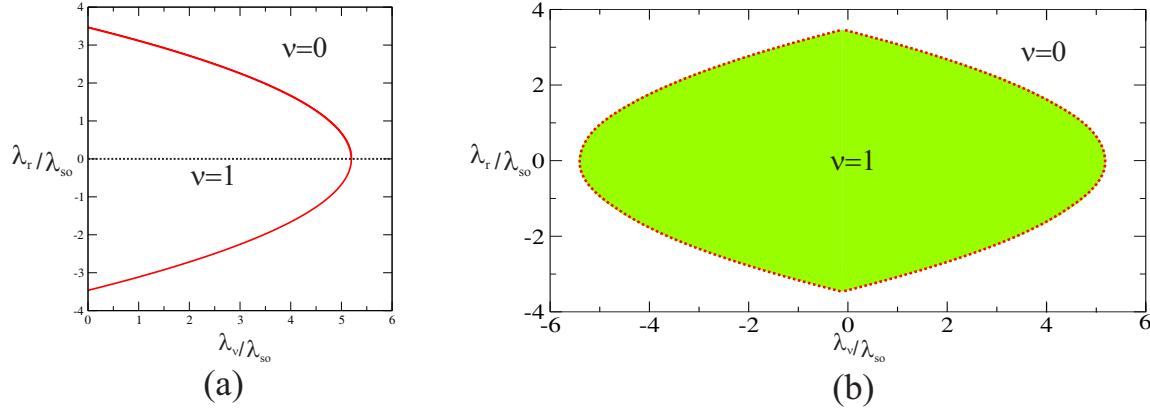
Figure 3.14: (a) Analytic phase transition boundaries of Kane and Mele model obtained from Eq. (3.50). Calculated phase diagram of Kane and Mele model using numerical formula Eq (3.51).

One can simply diagonalize this Hamiltonian to obtain the energy spectrum of this model. This gives rise to band insulators in which can be either trivial or topological [139]. The transition between these trivial and topological phases depends on the values of parameters λ_{so}, λ_ν, and λ_r which result in a phase diagram. At the phase transition boundary, a band closure occurs which are located at K and K$'$. The explicit representation of Hamiltonian (6.14) at K$'$ point is

$$H_K = \begin{pmatrix} \lambda_\nu - 3\sqrt{3}\lambda_{so} & 0 & 0 & -3i\lambda_r \\ 0 & -\lambda_\nu + 3\sqrt{3}\lambda_{so} & 0 & 0 \\ 0 & 0 & \lambda_\nu + 3\sqrt{3}\lambda_{so} & 0 \\ +3i\lambda_r & 0 & 0 & -\lambda_\nu - 3\sqrt{3}\lambda_{so} \end{pmatrix}, \tag{3.48}$$

which results in the energy gap

$$E_g = |6\sqrt{3}\lambda_{so} - \lambda_\nu - \sqrt{\lambda_\nu^2 + 9\lambda_r^2}|. \tag{3.49}$$

Here, we assume that $\lambda_{so} > 0$ and rewrite the energy gap in unit of λ_{so} as $E_g/\lambda_{so} = |6\sqrt{3} - \lambda_\nu/\lambda_{so} - \sqrt{(\lambda_\nu/\lambda_{so})^2 + 9(\lambda_r/\lambda_{so})^2}|$. Therefore the phase transition boundaries as shown in Fig. 3.14 are given by

$$\frac{\lambda_r}{\lambda_{so}} = \pm\sqrt{12 - 4\frac{\sqrt{3}}{3}\frac{\lambda_\nu}{\lambda_{so}}}. \tag{3.50}$$

To recognize the topology of each region, we can examine the edge band structure of graphene strip with zigzag edges for fixed values of parameters. We choose t as the energy scale and fix the values of the other parameters as Ref. [139] to be $\lambda_{so} = 0.06t$,
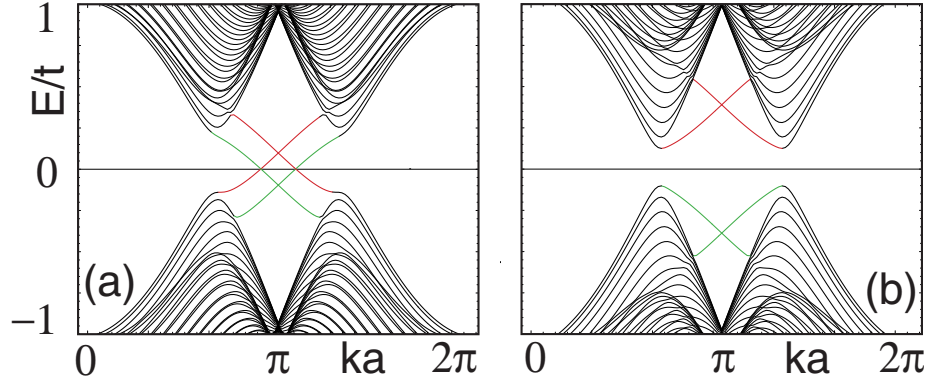
Figure 3.15: 1D energy bands for a zigzag strip in the Kane and Mele model adapted from [139]. (a) QSH phase with $\lambda_\nu = 0.1t$ and (b) Normal insulating phase with $\lambda_\nu = 0.4t$. For both cases $\lambda_{so} = 0.06t$ and $\lambda_r = 0.05t$.

$\lambda_r = 0.05t$, and $\lambda_\nu = 0.1t$ and $\lambda_\nu = 0.4t$ for Figs. 3.15(a) and (b) [139], respectively. As seen, both energy spectrum have a bulk energy gap and edge states. But, the different behavior of the edge states signals the existence of the distinct topological phases. As shown in Figs. 3.15(a) and (b), in the QSH phase the edge states traverse the energy gap in pairs, whereas in the insulating state the edge states do not traverse the gap [139]. Therefore, we can simply classify the separated regions as $\nu = 1$ and $\nu = 0$ (see Fig. 3.14(a)).

As discussed before, the most straightforward way for determining the topology of the band insulators and obtaining the corresponding phases is the calculation of the $\mathbb{Z}_2$ invariant. Here, we proceed by numerical calculation of the $\mathbb{Z}_2$ invariant for the Kane and Mele model and comparing the obtained phase diagram with the analytic expression.

Equation (3.39) is the formula for the $\mathbb{Z}_2$ invariants of rectangular lattices. Therefore, in order to use this formula for the Kane and Mele model with a honeycomb lattice, one can again simply use the change of variables (2.54 to convert the equivalent rhombus shape of the honeycomb BZ in k space as shown in Figs. 2.10(a) and (b), into a unit square in q space (See Fig. 2.10). This, allows us to use the more simple lattice version of Eq. (3.27)

$$\nu = \frac{1}{2\pi i} \left[\sum_{q_l \in \partial \text{HBZ}} A_x(q_l) - \sum_{q_l \in \text{HBZ}} F_{xy}(q_l) \right] \text{(mod 2)}, \tag{3.51}$$

where the lattice sites of the BZ are labeled by q_l. Thus, the described gauge fixing procedure is applied on the equivalent q points. The unimodular link variable U, the Berry potential $\mathcal{A}$ and the Berry field $\mathcal{F}$ are rewritten in the q_x-q_y plane, and the numerical calculations is done over the lattice version of square BZ in Fig. 2.10(b).

In Fig. 3.14(b), we have shown the numerically obtained $\mathbb{Z}_2$ phase diagram for the Kane

and Mele model. We see that the two phases obtained from our numerical calculations are accurately described by the analytic expression (dotted lines) for the phase transition boundary.

3.4.2 $\mathbb{Z}_2$ invariants for bilayer graphene

As one more example, we consider the TB Hamiltonian for the AB-stacked bilayer graphene in the presence of Rashba SOC [171]. We also suppose that an interlayer potential difference $2V$ is applied by a gate voltage to the planes of bilayer graphene [171]. Hence, the model Hamiltonian is given by
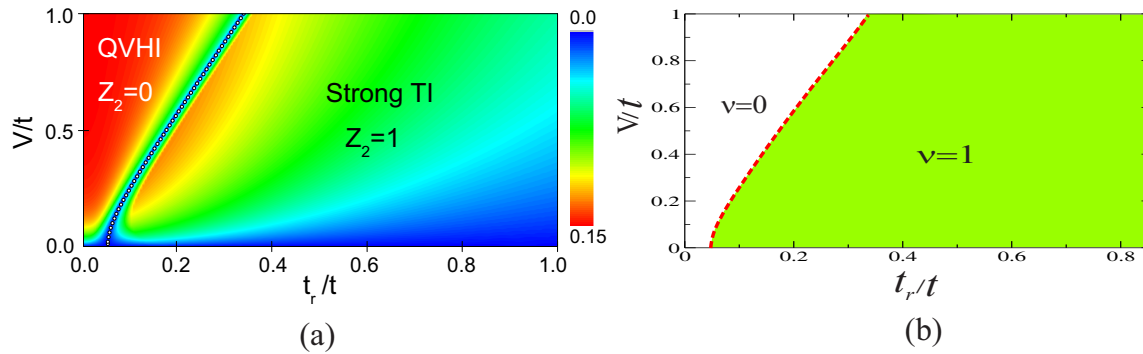
Figure 3.16: (a) Phase diagram of $\mathbb{Z}_2$ invariants of bilayer graphene as a function of gate voltage and Rashba SOC at fixed interlayer tunneling $t_\perp/t = 0.1429$. Adapted from [171]. (b) Reproduction of the phase diagram (a) using numerical formula Eq. (3.51). The dashed line shows the analytic expression for the boundary of a topological phase transition which exactly matches the obtained numerical boundary.

$$
\begin{aligned}
H_{\mathrm{BLG}} \;=\; & H_{\mathrm{SLG}}^{\mathrm{T}} + H_{\mathrm{SLG}}^{\mathrm{B}} + t_\perp \sum_{i\in\mathrm{T},j\in\mathrm{B},\sigma} c_{i\sigma}^\dagger c_{j\sigma} \\
& + V \sum_{i\in\mathrm{T},\sigma} c_{i\sigma}^\dagger c_{i\sigma} - V \sum_{i\in\mathrm{B},\sigma} c_{i\sigma}^\dagger c_{i\sigma}.
\end{aligned}
\tag{3.52}
$$

Here, $H_{\mathrm{SLG}}^{\mathrm{T}}$ ($H_{\mathrm{SLG}}^{\mathrm{B}}$) is the single layer Hamiltonian of the top (bottom) graphene layer including the Rashba SOC [171]

$$
H_{\mathrm{SLG}} = t \sum_{\langle ij\rangle\sigma} c_{i\sigma}^\dagger c_{j\sigma} + i\lambda_r \sum_{\langle ij\rangle\sigma\sigma'} c_{i\sigma}^\dagger (\mathbf{s}\times\hat{\mathbf{d}}_{ij})_z^{\sigma\sigma'} c_{j\sigma'},
\tag{3.53}
$$

as we have explained in the Kane and Mele model. The third term in Eq. (3.52) is the interlayer tunneling between the two layers with hopping energy $t_\perp$, and the mentioned interlayer potential difference $2V$ is given by the last two terms [171].

Similarly, we can rewrite this model Hamiltonian in the Fourier space and diagonalize it to obtain the corresponding energy bands. Using the formula Eq. (3.51), we numerically calculated the $\mathbb{Z}_2$ invariants over the honeycomb BZ of bilayer graphene as a function of V and λ_r at fixed hopping $t_\perp/t = 0.1429$ to reproduce the obtained phase diagram of the $\mathbb{Z}_2$ invariants in Ref. [171] (see Figs. 3.16(a) and (b)). Using the low-energy Hamiltonian of bilayer graphene, it was shown [171] that the topological phase transition boundary is given by

$$\lambda_r^2 = V^2 + t_\perp^2. \tag{3.54}$$

We have plotted this analytic expression (dashed line) on the numerically obtained boundary of topological phase transition in Fig. 3.16(b). The comparison between the phase diagrams in Fig. 3.16(a) and Fig. 3.16(b) shows that the results of Fig. 3.16(a) have accurately reproduced which demonstrates the validity of our algorithm to determine the topology of band insulators.

In the remaining parts of this thesis, we will use this numerical recipe for the calculation of the $\mathbb{Z}_2$ invariants whenever it is required to investigate the topology of bulk band structures.

3.5 Experimental Signatures of TIs

During the past few years many 2D TI and 3D TI host materials have been theoretically predicted (A comprehensive review on the 2D and 3D host materials for TIs can be found in Ref. [132]). However, many of the theoretically predicted TI host materials have not been realized experimentally [132]. For example, as we mentioned before, the theoretical predictions of QSH phase in graphene [57] and in conventional semiconductors in the presence of a strain gradient [58] are very difficult to be realized in experiments. Nevertheless, some of these potential host materials have already been verified by experiments [132]. To the best of our knowledge, the materials realization of 2D TIs is still limited to only the quantum well systems CdTe/HgTe/CdTe [118] and InAs/GaSb/AlSb [172]. On the other hand, the movement toward synthesizing 3D TI host materials has been easier, leading to a wider generation of materials realization including simple elements, binary compounds, ternary compounds, and quaternary compounds [173]. In what follows, we introduce briefly the experimental methods to identify the signature of QSHE in 2D TIs and the existence of topologically protected surface states in 3D TIs.
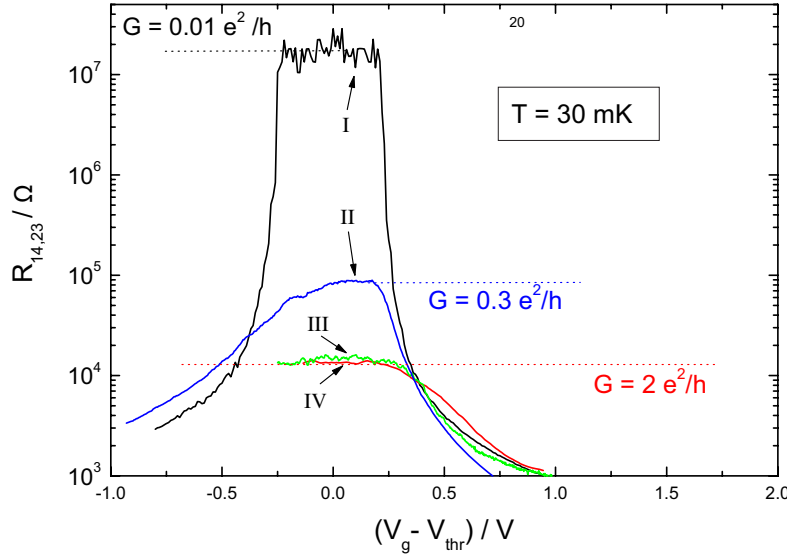
Figure 3.17: The first experimental evidence which establishes the existence of QSH phase. Adapted from [118]. Shown are the four-terminal resistance $R_{14,23} = V_{23}/I_{12}$ in a Hall bar geometry as a function of the gate voltage $V_g - V_{th}$ at temperature 30mk.

3.5.1   Transport measurements

In a further attempt to investigate new materials with non-trivial topology, Bernevig, Hughes, and Zhang [121] (BHZ) introduced an effective model which provides an experimental way to achieve a topological phase transition from a normal insulator to a TI in a sample of inverted HgTe/CdTe quantum well by varying the thickness d_c of the HgTe layer. They showed that in the heterostructure CdTe/HgTe/CdTe the band inversion in the HgTe thin film necessarily gives rise to a level crossing at the critical thickness $d_c \approx 6.3$nm [121]. This is due to the fact that CdTe is a normal insulator with a positive gap whereas HgTe is a semi-metal with inverted (negative) gap [121]. Therefore, the predominance of CdTe or HgTe in the sample leads to different electronic band structure of corresponding heterostructure [121]. For thickness $d_c < 6.3$nm the quantum well is in the normal phase, because the CdTe is predominant. For thickness $d_c > 6.3$nm the quantum well is in the topological phase, because the HgTe film dominates [121].

 This theoretical prediction of the QSH phase was soon observed in a series of transport measurements on HgTe quantum wells [118, 174]. Figure 3.17 shows the first experimental evidence which established the existence of the QSH state [118]. As seen, the four-terminal resistances $R_{14,23} = V_{23}/I_{12}$ in a Hall bar geometry have plotted for samples with different sizes as a function of the gate voltage $V_g - V_{th}$. Here, V_{th} denotes the thresh-

old voltage which $R_{14,23}$ takes its maximum value. The transport measurements have been done in the absence of any magnetic field and at temperature 30mk. Indeed, by varying the gate voltage one can probe the presence of an energy gap. Then, to establish the existence of a pair of conducting counter-propagating edge states at one edge, the analysis of the transport measurement must be done where the Fermi level position is inside the band gap. Therefore, each one of them shares a conductance of e^2/h which results in a non-zero value of conductance $2e^2/h$ for the bulk-insulating regime.

The black curve I and curves II, III and IV (blue, green and red respectively) show the transport measurements for the well thicknesses $d_c = 5.5$nm and $d_c = 7.3$nm, respectively. The sample sizes are $(20.0 \times 13.3 \ \mu\text{m}^2)$ for samples I and II, $(1.0 \times 1.0 \ \mu\text{m}^2)$ for sample III, and $(1.0 \times 0.5 \ \mu\text{m}^2)$ for sample IV. As expected, since in the sample I the thickness of the well corresponds to a normal band ordering, it shows a large resistance if the Fermi energy is in the band gap. In contrast, the thicknesses of the wells II, III, and IV correspond to inverted band gaps. Hence, one expects theoretically to observe a conductance $2e^2/h$ associated with one edge when the Fermi energy is in the band gap. However, due to the inelastic scattering length (which is estimated at about $l_{in} \approx 1\mu\text{m}$ [118] for the temperature used in the measurement) compared to the sample size, the measured conductance shows an enhanced resistance as seen in curve II. This originate from the fact that in the presence of TR symmetry elastic scattering is prohibited but it does not protect them against inelastic scattering which leads to backscattering and contribution in the enhancement of longitudinal resistance [118]. Notably, in curves III and IV where the sample sizes are shorter than the inelastic scattering length, measurements show a conductance $2e^2/h$ independent of the sample sizes which convincingly demonstrate the existence of counter-propagating edge states in the QSH phase [118]. Note that some fluctuations are seen at plateaus which can be explained by the existence of potential fluctuations within the sample [118].

3.5.2   Angle-resolved photoemission spectroscopy measurements

Angle-resolved photoemission spectroscopy (ARPES) is one of the most direct methods to investigate the electronic band dispersion in crystalline solids [176]. In recent years, this method has been used especially to study the topological characteristics of TIs [175], Dirac semimetals [177] and Weyl fermions [178]. Among the list of experimentally confirmed 3D TIs, the most famous family is the binary compounds Bi_2Te_3, Bi_2Se_3, Sb_2Te_3, and their alloys [132, 173]. As an example, we have shown in Fig. 3.18 the obtained ARPES measurements for the electronic band structure of undoped Bi_2Se_3 [175]. As can be seen in Fig. 3.18(a), in addition to the bulk conduction band (BCB) and bulk valence band (BVB), there exists a surface state band (SSB) which consists of a single Dirac cone demonstrating
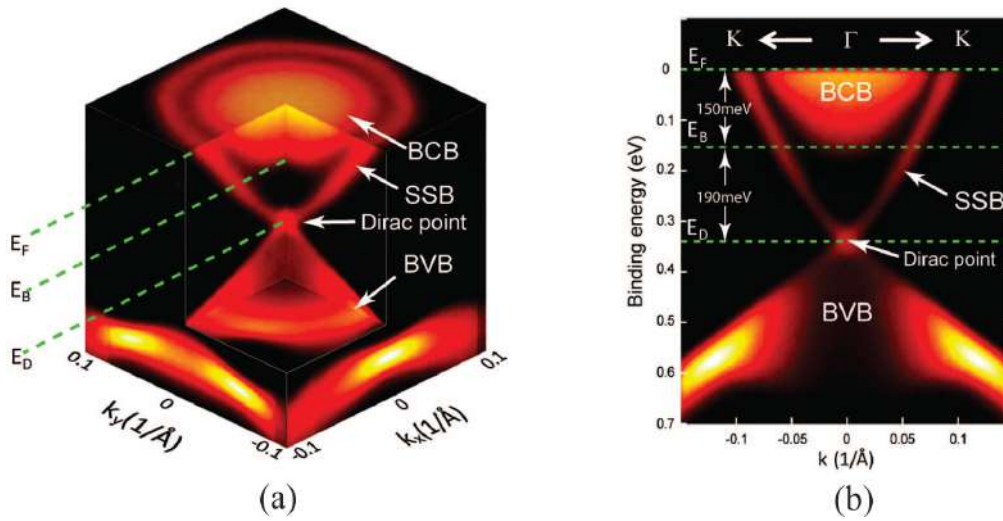
Figure 3.18: Detection of Z2 topological order in Bi_2Se_3 using ARPES. Adapted from [175]. (a) In addition to BCB and BVB, there exists a SSB which consists of a single Dirac cone. (b)The band structure along with some high symmetry points in the hexagonal surface BZ of Bi_2Se_3.

that Bi_2Se_3 is a 3D TI [175]. Figure. 3.18(b) shows the band structure along with some high symmetry points in the hexagonal surface BZ of Bi_2Se_3. The BCB bottom (E_B) is about 190 meV above the Dirac energy (E_D) and 150 meV below (E_F).

3.5.3 Scanning tunneling microscope measurements

Scanning tunneling microscopy and spectroscopy (STM/S) measurements are also expected to play an important role in making progress toward the experimental observation of 3D TIs [179, 180]. Using this surface sensitive technique whose principle of operation is based on the idea of quantum tunneling, one can study surface topography (STM measurement) and obtain some information on the electronic structure at a given location in the sample (STS measurement) [180]. The STS measurements give rise to a plot of the local density of states as a function of energy of the sample [180] which can be utilized to establish the realization of topological gapless surface states in a host material [179, 180]. As an example of the experimental demonstration of topological surface states, Zhang *et al.* [179] used a scanning tunneling microscope to report direct imaging of standing waves in 3D TI Bi_2Te_3 due to scattering of the topological states off Ag impurities [179]. The existence of standing waves robustly supports the idea of the surface nature of topological modes [179]. They also studied the gapless surface states of Bi_2Te_3 by STS which detects the differential tunneling conductance dI/dV [179]. As depicted in Fig. 3.19(a), their
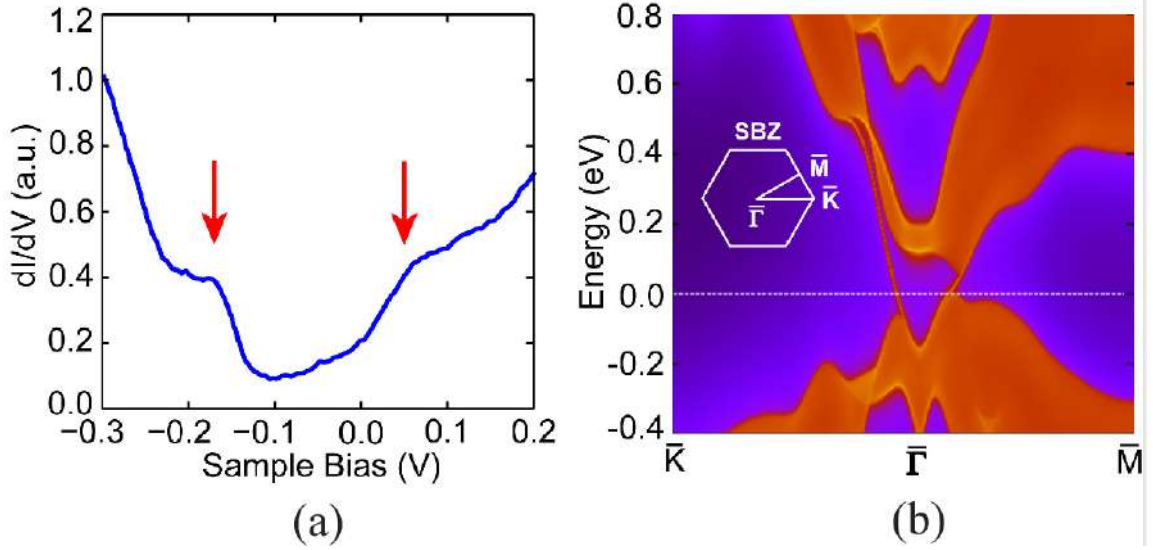
Figure 3.19: (a) The differential tunneling conductance dI/dV taken on bare $Bi_2Te_3(111)$ surface. Adapted from [179]. (b) The calculated band structure of $Bi_2Te_3(111)$ along with high symmetry directions of surface BZ. Adapted from [179].

results showed that the differential conductance in the bulk insulating gap of Bi_2Te_3 behaves linearly with respect to the applied bias in which is attributed to the realization of the gapless surface states. Figure 3.19(b) shows the calculated band structure of $Bi_2Te_3(111)$ along with high symmetry directions of surface BZ which is the theoretical proof of the observed topological surface states.

Scaling laws for band gaps of phosphorene nanoribbons

In this chapter, we analyze the band structure, the state characterization, and electronic transport of monolayer zigzag phosphorene nanoribbons (zPNRs) and armchair phosphorene nanoribbons (aPNRs), using five-parameter TB approximation. In zPNRs, the ratio of the two dominant hopping parameters indicates the possibility of a relativistic dispersion relation and the existence of a pair of separate quasi-flat bands at the Fermi level. Moreover, the corresponding states are edge localized if their bands are well separated from the valence and conduction bands. We also investigated the scaling laws of the band gaps versus ribbon widths for the armchair and zigzag PNRs. In aPNRs, the transverse electric field along the ribbon width enhances the band gap closure by shifting the energy of the valence and conduction band edge states. For zPNRs, a gap occurs at the middle of the relatively degenerate quasi-flat bands; thus, these ribbons are a promising candidate for future field-effect transistors (FETs).

4.1   Introduction

2D structures that are inspired by graphene such as hexagonal boron nitride (BN) and TMDs have attracted considerable attentions owing to their remarkable electronic properties [1, 3, 181–184]. Graphene is known to have novel electronic and mechanical properties such as high carrier mobility; however, its zero band gap limits its performance. As a TMD, MoS_2 has a direct band gap of $\sim$1.8 eV [12] and a relatively high on/off ratio [13].

However, the carrier mobility of MoS_2 is much less than that of graphene. These layered structures can be etched or patterned as quasi-one-dimensional (1D) strips referred to as nanoribbons. Graphene nanoribbons (GNRs) and MoS_2 nanoribbons are examples of these 1D strips. These 1D nanoribbons can offer better tunability of their electronic structures because of quantum confinement and edge effects [185–187].

Monolayer BP has attracted much attention recently because of its remarkable properties as we reviewed in chapter 1. Experiences with graphene and other 2D materials suggest the electronic structure and optical properties of PNRs must be studied for future research on phosphorene-based nanoelectronics.

Numerous studies on electronic properties of MLP and PNRs have focused on first-principle calculations [188–193]. In this chapter, we first introduce a TB model for describing the low-energy spectrum of MLP. Then the band structure and effective masses of the MLP near the gap are presented based on this TB model and it is shown that the dispersion is relativistic along the a direction and the Fermi velocities along this direction are calculated. Thereafter, the TB model is applied to zigzag and armchair PNRs to analyze their band structure and quantum conductance and compare the results with other more sophisticated calculations. The scaling behavior of band gap with ribbon width is presented and the obtained results are compared with those of the other methods. Then,we examine the effect of transverse electric field on the band structure and quantum conductance of both zigzag and armchair nanoribbons.

4.2   Model Hamiltonian

We have illustrated in Fig. 4.1 the crystal structure and the lattice constants of MLP. As can be seen, the phosphorus sites are grouped in two zigzag layers. The upper and lower sites are shown with darker and lighter colors, respectively. The proposed TB model for MLP includes hopping integrals (t_i) over five neighbouring sites [29] as shown in Fig. 4.1(a). The TB Hamiltonian in second quantization formalism is written as [29]

$$H = \sum_{i,j} t_{ij} c_i^\dagger c_j, \qquad (4.1)$$

where the summation is over the lattice sites, and t_{ij} are the hopping integrals between the ith and jth sites. Further, $c_i^\dagger$ and c_j represent the creation and annihilation operators of electrons in sites i and j, respectively. The connections in the upper or lower layers in each zigzag chain are represented by t_1 hopping integrals, and the connections between a pair of upper and lower zigzag chains are represented by t_2 hopping integrals. Further, t_3 denotes the hopping integrals between the nearest sites of a pair of zigzag chains in the upper or
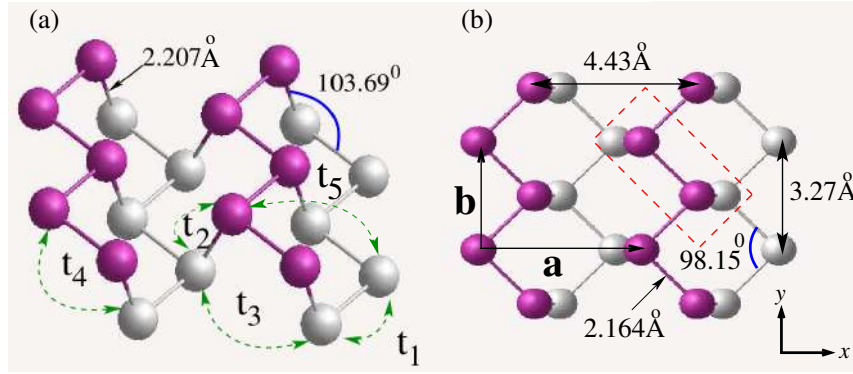
Figure 4.1: (a) Crystal structure and hopping integrals t_i of single layer phosphorene for the TB model. (b) Top view. Note that the dark (gray) balls represent the P atoms in the upper (lower) layer. The dotted rectangle indicates a primitive unit cell containing four atoms. The parameters for the bond angles and unit cell lengths are taken from [194].

lower layer, and t_4 denotes the hopping integrals between the next nearest neighbor sites of a pair of upper and lower zigzag chains. Finally, t_5 is the hopping integrals between two atoms on the upper and lower zigzag chains that are farthest from each other. The specific values of these hopping integrals as suggested in [29] are as follows: $t_1 = -1.220$ eV, $t_2 = 3.665$ eV, $t_3 = -0.205$ eV, $t_4 = -0.105$ eV, and $t_5 = -0.055$ eV. The special characteristic of this model is that the second hopping integral is positive. This implies that the zigzag chains have negative t_1 hopping integrals along the chains and positive t_2 hopping integrals connecting these chains. For zPNRs, the eigenstates of the transverse modes, which characterize the behavior of the states as edge or bulk states, are along both t_1 and t_2 connections. The role of this behavior in creation of a relativistic band dispersion along the Γ-X direction will be discussed in the next section.

4.3   TB calculations of electronic properties of MLP

In this section the band structure and effective masses of the electron and hole states of the bulk MLP is calculated based on the above mentioned TB model and the results are compared with *ab-inito* calculations. Since each unit cell of a single layer phosphorene contains four P atoms [Fig. 4.1(b)], initially, a four band model is created. The band dispersion along the two periodic directions of Γ-X and Γ-Y are compared and the electron and hole effective masses are compared along the two directions. In the next subsection it is argued that the unit cell for the electronic model only contains two P atoms resulting in a two band model. Finally, the band gap at Γ point is derived as a function of the hopping
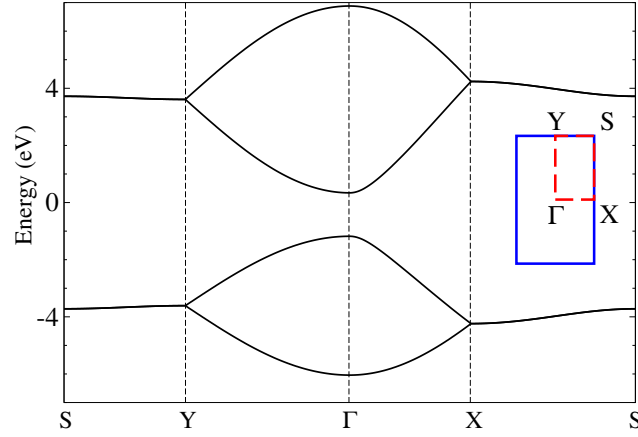
Figure 4.2: Tight-binding energy band structure for bulk phosphorene.

parameters.

4.3.1   Four-band TB model

As shown in Fig. 4.1(b) the unit cell of the MLP is a rectangle containing four P atoms. Fourier transforming, the general Hamiltonian in momentum space is given by

$$H = \sum_{\mathbf{k}} \psi_{\mathbf{k}}^{\dagger} H_{\mathbf{k}}^{[4]} \psi_{\mathbf{k}}, \tag{4.2}$$

where $\psi_{\mathbf{k}}^{\dagger} = (a_{\mathbf{k}}^{\dagger} \ b_{\mathbf{k}}^{\dagger} \ c_{\mathbf{k}}^{\dagger} \ d_{\mathbf{k}}^{\dagger})$ and $H_{\mathbf{k}}^{[4]}$ is a 4×4 matrix

$$H_{\mathbf{k}}^{[4]} = \begin{pmatrix} 0 & A_{\mathbf{k}} & B_{\mathbf{k}} & C_{\mathbf{k}} \\ A_{\mathbf{k}}^* & 0 & D_{\mathbf{k}} & B_{\mathbf{k}} \\ B_{\mathbf{k}}^* & D_{\mathbf{k}}^* & 0 & A_{\mathbf{k}} \\ C_{\mathbf{k}}^* & B_{\mathbf{k}}^* & A_{\mathbf{k}}^* & 0 \end{pmatrix}, \tag{4.3}$$

whose elements are given by

$$\begin{aligned} A_{\mathbf{k}} &= t_2 + t_5 e^{-ik_a} \\ B_{\mathbf{k}} &= 4t_4 e^{-i(k_a - k_b)/2} \cos(k_a/2) \cos(k_b/2) \\ C_{\mathbf{k}} &= 2e^{ik_b/2} \cos(k_b/2)(t_1 e^{-ik_a} + t_3) \\ D_{\mathbf{k}} &= 2e^{ik_b/2} \cos(k_b/2)(t_1 + t_3 e^{-ik_a}). \end{aligned}$$

$$\tag{4.4}$$

Here $k_a = \mathbf{k} \cdot \mathbf{a}$ and $k_b = \mathbf{k} \cdot \mathbf{b}$, where $\mathbf{a} = a\hat{\mathbf{x}}$ and $\mathbf{b} = b\hat{\mathbf{y}}$ are the primitive translational vectors of the structure displayed in Fig. 4.1(b). Bulk energy bands for the MLP are shown in Fig. 4.2. The band dispersion is relativistic along the x direction whereas it is nonrelativistic along the y direction. Considering a relativistic band dispersion, $E = \sqrt{m^2 v_F^4 + p^2 v_F^2}$, along the Γ-X direction and a parabolic form along the Γ-Y direction near the conduction band minimum (CBM) and valence band maximum (VBM) the effective masses and the Fermi velocities are calculated and presented in Table 4.1. It can be deduced from Table 4.1 that electrons and holes moving along the zigzag direction are more than six times heavier than those moving along the armchair direction. There is a simple explanation for the reason why this special combination for the dominant hopping parameters ($t_1 = -1.220$ eV and $t_2 = 3.665$ eV) creates a nearly relativistic dispersion near Γ point along the x direction. We introduce a lattice model (Fig. 4.3(a)), which is equivalent to the MLP within the two parameter TB approximation. For this model the dispersion along the y direction for large wavelengths along x ($|k_a| \sim 0$ and no dynamics along the x direction) can be modeled by TB on a linear chain shown in Fig. 4.3(b). Similarly, the dispersion along the x direction for $|k_b| \sim 0$ can be modeled by TB on a chain shown in Fig. 4.3(c). For the linear chain of Fig. 4.3(b) the dispersion would be $2t_1 \cos(k_b)$, which near $k_b \simeq 0$ is $-|2t_1| + |t_1|k_b^2$, and it is parabolic. This dispersion gives rise to an effective mass of $m = 1.17m_0$, which is consistent with the data in Table 4.1. The dispersion for the linear chain of Fig. 4.3(c) along the x direction is given by $\pm\sqrt{(2t_1)^2 + t_2^2 + 4t_1 t_2 \cos(k_a)}$. In terms of the absolute values of the hopping parameters and near the $k_a \simeq 0$, this relation is reduced to $\pm\sqrt{(|2t_1| - |t_2|)^2 + 2|t_1 t_2|k_a^2}$. When $|t_2|$ is close to $|2t_1|$, we can ignore the first term under the square root and the dispersion will be linear $\pm\sqrt{2|t_1 t_2|}k_a$ and the constant of proportionality gives a Fermi velocity of $2\pi\sqrt{2(1.22\text{eV})(3.665\text{eV})} \times (4.43\text{Å}/2)/(12400\text{eVÅ}) \times c \sim 10^6$ m/s which is consistent with the data of Table 4.1. For the model of Eq.(4.1), $|t_2| \simeq 3|t_1|$ which does not give an exactly linear dispersion but it gives a massive relativistic dispersion, and for larger values

Table 4.1: Fermi velocities and effective masses of electron and hole states near the CBM and VBM along the two directions of Γ-X and Γ-Y.

Band	v_F ($\times 10^5$ m/s)	m/m_0
Γ-X (e)	9.71	0.164
Γ-X (h)	8.26	0.179
Γ-Y (e)	–	0.873
Γ-Y (h)	–	1.175
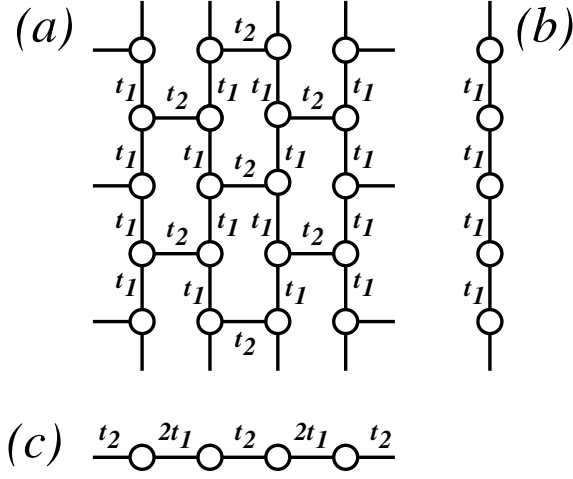
Figure 4.3: (a) Topologically equivalent structure to MLP within two parameter TB model. (b) Equivalent linear chain model along the zigzag direction. (c) Equivalent linear chain model along the armchair direction.

of k_a it is nearly linear.

4.3.2   Two-band TB model

In the TB Hamiltonian of Eq. (4.1), if we project the positions of the upper and lower zigzag chains on a horizontal plane and keep the previous hopping integrals, the unit cells of the electronic system is reduced to two P atoms per unit cell. The Fourier transform of the resulting two band model is given by

$$H = \sum_{\mathbf{k}} \phi_{\mathbf{k}}^{\dagger} H_{\mathbf{k}}^{[2]} \phi_{\mathbf{k}} \tag{4.5}$$

where $\phi_{\mathbf{k}}^{\dagger} = (a_{\mathbf{k}}^{\dagger} \ b_{\mathbf{k}}^{\dagger})$ and $H_{\mathbf{k}}^{[2]}$ is a 2×2 matrix

$$H_{\mathbf{k}}^{[2]} = \begin{pmatrix} B_{\mathbf{k}} e^{i(k_a - k_b)/2} & A_{\mathbf{k}} + C_{\mathbf{k}} e^{i(k_a - k_b)/2} \\ A_{\mathbf{k}}^* + C_{\mathbf{k}}^* e^{-i(k_a - k_b)/2} & B_{\mathbf{k}} e^{i(k_a - k_b)/2} \end{pmatrix} \tag{4.6}$$

Diagonalizing the above matrix, the energy spectrum is

$$E_{\mathbf{k}} = |B_{\mathbf{k}}| \pm |A_{\mathbf{k}} + C_{\mathbf{k}} e^{i(k_a - k_b)/2}| \tag{4.7}$$

The band gap in the Γ point is

$$E_g = 4t_1 + 2t_2 + 4t_3 + 2t_5 = 1.52 \text{ eV}. \tag{4.8}$$

4.4 Electronic and transport properties of PNRs

In the following numerical analysis, the commonly used method for determining the width of graphene nanoribbons [195] is employed to determine the PNR structures. According to this method, the structure of aPNR is defined by the number of dimmer lines across the ribbon width (N_a-aPNRs), whereas that of zPNR is defined by the number of zigzag chains across the ribbon width (N_z-zPNRs) [36]. To calculate the band structure and eigenstates of the nanoribbons, we obtain the eigenvalues and eigenvectors of the following matrix, which is the crystal Hamiltonian between Bloch sums:

$$M_{\alpha\beta}(\mathbf{k}) = -\sum_{ij} t_{i\alpha;j\beta} e^{i\mathbf{k}\cdot\mathbf{R}_{ij}} \tag{4.9}$$

where i and j denote different unit cells, α and β denote the basis sites in a unit cell. Further, $\mathbf{k}$ is the wave vector, and $\mathbf{R}_{ij}$ represents a bravais lattice vector. Moreover, $t_{i\alpha;j\beta}$ are the hopping integrals between the basis site α of unit cell i and the basis site β of unit cell j, and will be substituted by the five hopping parameters of the model, accordingly. For nanoribbons, the periodicity is only along the ribbon length; therefore, the number of basis sites in each unit cell is proportional to the ribbon width.

4.4.1 Edge modes in zPNRs

In order to understand the physics of this model, we study the influence of the ratio of the two dominant hopping parameters on the behavior of the electronic structure for zPNRs. We first study the dependence of quasi-flat bands and their corresponding edge states in zPNRs on the ratio of $|t_2/t_1|$. The band structure and probability amplitude of the upper valence band eigenstates of 100-zPNR for $|t_2/t_1|$ =1, 2, and 3 for $k = 0$ are shown in Fig. 4.4. As can be seen in Figs. 4.4(a), (b), and (c), as the $|t_2/t_1|$ ratio increases, the two middle bands (shown with grey lines) are detached from the bulk bands. The critical value of the ratio for the emergence of edge states at $k = 0$ is 2, namely, at this ratio, the average amplitude of $|\Psi_i|^2$ becomes nearly homogeneous in the bulk. It should be noted that the states corresponding to the quasi-flat bands that are outside the middle region including between Dirac-like points and $k = \pi$ or $k = -\pi$ are always localized on the edges. Fig. 4.4(c) shows the band structure for $|t_2/t_1|$=3. In this case, the edge bands are isolated
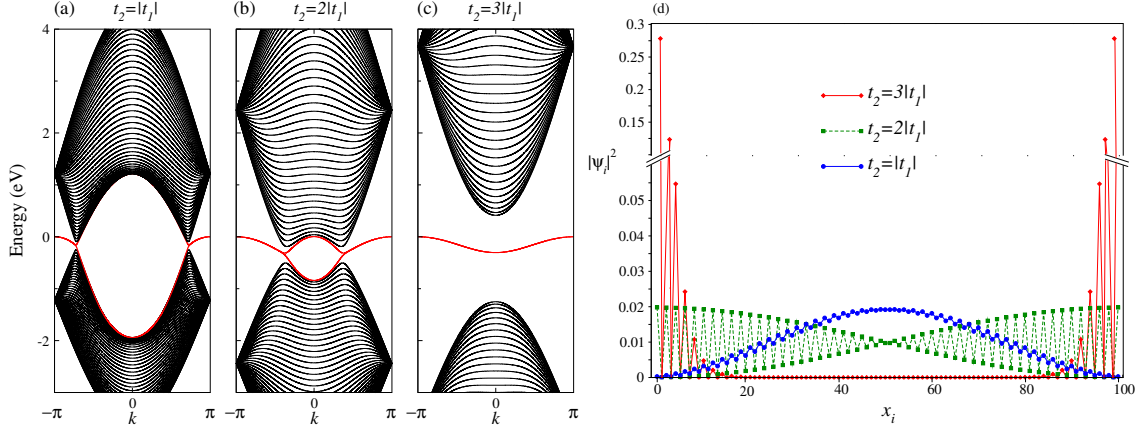
Figure 4.4: Top: Band structure of 100-zPNRs ($w \sim 22$ nm) for $|t_2/t_1|$ ratio values of (a) $|t_2/t_1|$=1, (b) $|t_2/t_1|$=2, and (c) $|t_2/t_1|$=3 for $t_3 = -0.205$ eV, $t_4 = -0.105$ eV, and $t_5 = -0.055$ eV. Note that the red lines represent the edge bands. Bottom: The probability amplitude of the upper valence band eigenstate for $k = 0$ of a zPNR for different ratios of $|t_2/t_1|$. Note that the horizontal axis represents a unit cell in the width of the ribbon.

from the bulk states, and are two-fold degenerate. This degeneracy is lifted in zPNRs with small widths ($N_z < 40$) for wave vectors near $k = 0$. This behavior can be explained by considering the effect of finite electron tunneling between two opposite edges of zPNRs with small widths [196]. Fig. 4.4(d) shows the probability amplitude of the upper valence band eigenstate for $k = 0$ as a function of the position of P atoms. As can be clearly seen, for small values of this ratio, the probability amplitude is large for the bulk sites, whereas for the edge sites, it is minimal or zero. The probability amplitude of the bulk sites decreases as this ratio is increased. For $|t_2/t_1|$=3, only the probability amplitude of the sites near the edges are non-zero, thus indicating the importance of the $|t_2/t_1|$ ratio in the creation of the edge states.

If we refer to the model that was introduced in Fig. 4.3, we can explain the above mentioned behavior as follows. The structure shown in Fig. 4.3 is a bipartite lattice, and each site is connected to three sites of the other sublattice with two t_1 links and one t_2 link. If we separate the total wave function to two components, each having amplitudes only on one sublattice, the local energy contribution of a wave function is proportional to the local amplitudes of the two component wave functions times $\Delta \equiv 2t_1 + t_2$. In the case of $\Delta < 0$ ($|t_2/t_1| < 2$), it is energetically more favourable for the two component wave functions to have maximum overlap, whereas in the case of $\Delta > 0$ ($|t_2/t_1| > 2$), we expect the two component waves to repel each other and push each other to the two edges of the nanoribbon. This is consistent with what is shown in Fig. 4.4(d). It should be mentioned that the
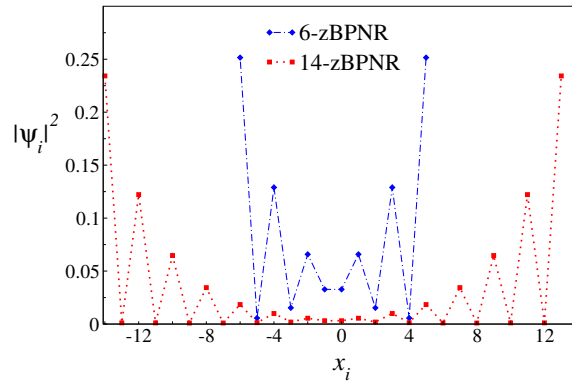
Figure 4.5: Probability amplitude of the edge band eigenstates of 6-zPNR ($w \sim 1.25$ nm) and 14-zPNR ($w \sim 3$ nm). Note that the horizontal axis indicates a unit cell in the width of the ribbon.

above discussion is only valid for the small values of the wave vector along the armchair direction, which corresponds to the quasi-flat bands at the Fermi level.

Clearly, the ribbon width is also important for the creation of the edge states in zPNRs. In zPNRs, the ribbon width must be greater than around 3 nm, which corresponds to 14-zPNR, for the edge states to appear. Fig. 4.5 shows the squared wave functions of the states in the edge band of 6-zPNR and 14-zPNR. For zPNRs with widths greater than 3 nm, the wave function corresponding to the two edges starts to decouple and will localize on the opposite edges.

4.4.2   Scaling laws of band gaps for PNRs

Fig. 4.6 shows the variation in band gap with ribbon width for zPNRs and aPNRs owing to the quantum confinement effect [195, 197–199]. In contrast to boron nitride nanoribbons (BNNRs) [200], graphene nanoribbons (GNRs) [195], and α-graphdiyne nanoribbons [201], the band gap of PNRs decreases monotonically as the ribbon width increases. Fig. 4.6 shows that the bang gap is larger in zPNRs for the same ribbon width, indicating that the energy contribution from quantum confinement is higher in zPNRs, thus resulting in a stronger quantum confinement effect in zPNRs.

The scaling behavior of band gap with increasing ribbon width for both types of PNRs has been calculated using DFT calculations [36, 188]. They suggested a scaling behavior of $\sim 1/w^2$ for aPNRs whereas a $\sim 1/w$ for zPNRs. We argue that the scaling law for the zPNRs is not $1/w$. In fact, since the electrons along the confinement direction of zPNRs, which is the armchair direction, behave like massive-relativistic particles, we fit our data for zPNRs with $E_{gap} = \sqrt{A^2/N_z{}^\alpha + B^2} + C$ ($w \simeq 0.22N_z - 0.08$ nm). The fitted
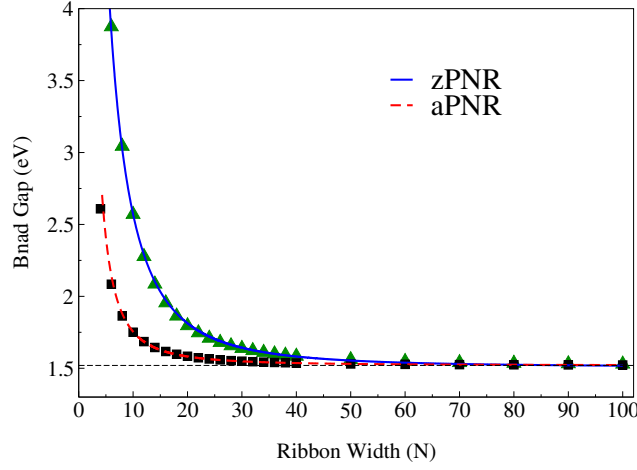
Figure 4.6: Variation in band gap of zPNRs and aPNRs with ribbon width.

values for the parameters are $A = 22.9$ eV, $\alpha = 2.18$, $B = 1.10$ eV, and $C = 0.42$ eV. In this formula, we expect a parabolic scaling law as long as the second term under the square root is much larger than the first term. This condition for the above fitted values occurs for $w \gg 3.5$ nm. In the massless-relativistic limit, where the energy contribution to the quantum confinement is proportional to the momentum, the first term is much larger than the second term, and this condition occurs for $w \ll 3.5$ nm. It should be mentioned that the band dispersion of the DFT calculations near the gap, specially for the Γ-X direction, are very close to our TB calculations, and the above discussion is also applicable to their scaling graphs. The maximum widths considered in the DFT calculations for the scaling is 3 nm; therefore, they have not been able to consider the parabolic region. According to the above discussion, we should not expect a $1/w$ scaling law for zPNRs with ribbon widths larger than 3.5 nm. For aPNRs we fit the data with $E_{gap} = A'/N_a{}^{\beta} + C'$ ($w \simeq 0.164(N_a - 1)$ nm), and the fitted values for the parameters are $A' = 20.4$ eV, $\beta = 1.92$, and $C' = 1.52$ eV, in agreement with previous results [36, 188]. We have also calculated the effective masses of the electron and hole states near the VBM and CBM of PNRs with different ribbon widths. The results are shown if Fig. 4.7. The effective masses of zPNRs are more than six times larger than aPNRs and for small widths their effective masses increase even to higher values.

4.4.3 Response of aPNRs to E_{ext}

Next, we analyze the relationship between the electronic properties of aPNRs (periodicity along the x-direction) and the external electric field (E_{ext}) along the ribbon width. The
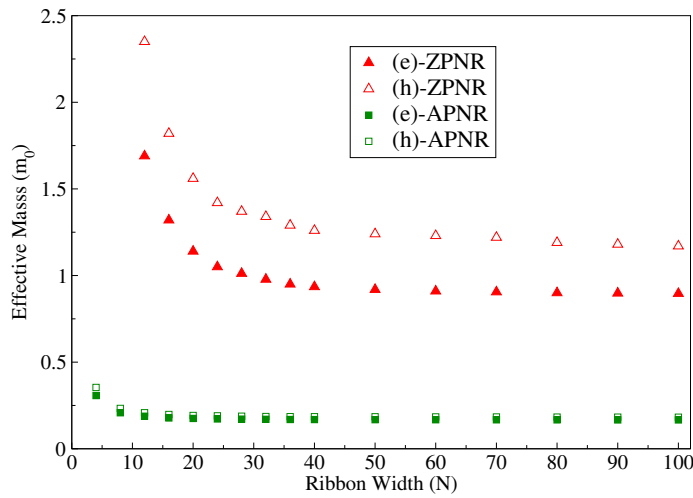
Figure 4.7: Variation in effective masses of zPNRs and aPNRs with ribbon width.

band structure for $E_{ext} = 0$ is shown in Fig. 4.8(a), in which the CBM and VBM determine the band gap. The electronic states associated with the VBM and CBM are located in the bulk of the ribbon [Fig. 4.8(b)]. Also, all aPNRs are semiconductors independent of their ribbon width. When a transverse E_{ext} is applied along the width, the states corresponding to the CBM, which have a positive band curvature (electron states), will shift to lower energies owing to Stark effect, whereas the states corresponding to the VBM (hole states) shift to higher energies. Therefore, the CBM and VBM states will localize on the ribbon edges (Fig. 4.8(d)). By further increasing the field strength, the two bands approach one another because of the electrostatic potential difference between the opposite edges, and the band gap decreases and eventually closes at a critical transverse field, E_c (Fig. 4.8(c)). This trend in band gap variation with E_{ext} has already been observed in other materials such as GNRs [195], carbon nanotubes [202], MoS_2 nanoribbons [196], and BNNRs [199**?** , 200]. It should be noted that in contrast to other compounds such as BN [200], that the structure have a polarization along the width, the gap closure does not change if we reverse the direction of the transverse E_{ext} along the width.

We also calculated the variation in band gap of aPNRs with E_{ext} for four different widths (Fig. 4.9). As the transverse E_{ext} increases, the band gap decreases uniformly. Similar behavior has been observed in the nanoribbons of BN [199, 200] and MoS_2 [196].

As the aPNR width increases, the band gap decreases rapidly with increasing transverse field E_c, and the gap closure occurs for smaller fields because the electrostatic potential difference is proportional to the ribbon width. The variation in band gap with ribbon width and transverse E_{ext} has been calculated recently using DFT [188]. For aPNRs with
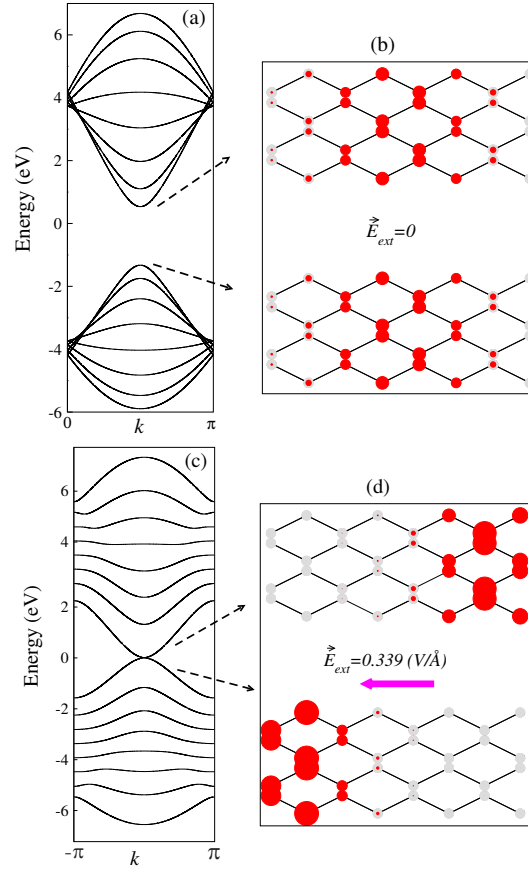
Figure 4.8: Top: (a) Band structure, and (b) probability amplitudes of 8-aPNR for zero transverse electric field. Bottom: The same graph for $E_{ext} = 0.339$ V/Å. Note that the eigenstates correspond to $k = 0$.

large widths, the results obtained with the TB approach are in good agreement with the DFT calculations. As the transverse E_{ext} increases, the gap closes directly at $k = 0$ for E_c=0.339 V/Å, and the edge band states corresponding to the VBM and CBM states are localized on the opposite edges of the aPNRs (Fig. 4.8(d)).

As shown in Fig. 4.9, the gap closure of aPNRs with small widths exhibits an interesting trend. For instance, for the 8-aPNR, the band gap varies slowly under a strong E_{ext}, and the band gap closes for E_c=0.339 V/Å, it opens again and closes at 0.527 V/Å. Note that due to the rapid progress in modern experimental techniques, a strong electric field up to 0.3 V/Åhas already applied to 2D-materials [203, 204]. The opening up of the band gap after its closure for very small ribbon widths is related to the finite hopping integrals between the two opposite edges and the mechanism for a similar behavior in MoS_2 nanoribbons
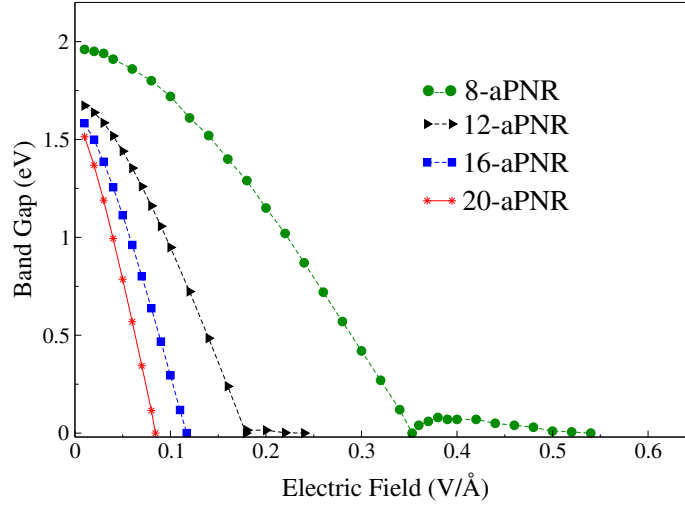
Figure 4.9: Variation in band gap of aPNRs with transverse external electric field for five different ribbon widths.

has been explained elsewhere [196].

4.4.4 Transistor effect in zPNRs

A study based on the TB model has investigated the effect of an external in-plane (E_{ext}) electric field on the edge modes of zPNRs and the effect of an external electric field (E_z) perpendicular to the ribbon surface on zPNRs [76]. The results show that the band gap increases in accordance with $(lE_z)^2$ where l is the separation distance between the upper and lower layers of phosphorene. Moreover, for E_{ext} greater than a critical strength (E_c), the degeneracy of the edge bands in Fig. 4.4 (c) is lifted for the quasi-flat bands, and a transistor effect can be observed. Further, E_c is inversely proportional to the ribbon width ($\propto 1/w$).

In this study, we investigated the transistor effect in zPNRs using the Landauer formalism [205, 206]. In this formalism, the conductance $\sigma(E)$ for nanoscale devices at Fermi energy (E_F) between a pair of leads p and q is given by

$$\sigma(E) = (\frac{e^2}{h})Tr[\Gamma_p(E)G_D^R(E)\Gamma_q(E)G_D^A(E)] \tag{4.10}$$

where $G_D^R(E)$ is the retarded Green's function of the device and $G_D^A(E) = G_D^{R\dagger}(E)$. In this equation, $\Gamma_{p(q)} = i[\Sigma_{p(q)}(E) - \Sigma_{p(q)}^{\dagger}(E)]$ where $\Sigma_{p(q)}(E)$ is the self energy related to
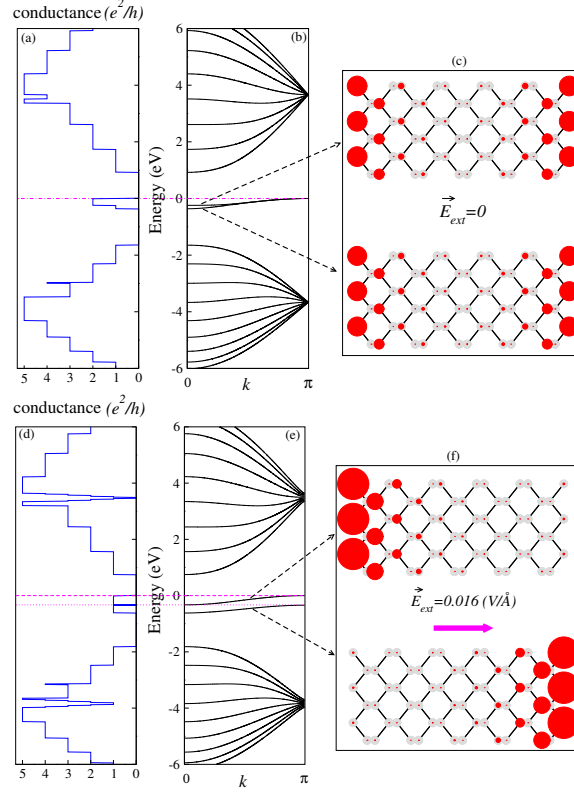
Figure 4.10: Top: (a) Conductance, (b) band structure, and (c) probability amplitudes of the band gap edge states of a 10-zPNR under zero transverse electric field. Bottom: The same graph for $E_{ext} = 0.016$ V/Å. Note that the eigenstates correspond to $k = 0$.

lead p (q). The retarded Green's function of the device ($G_D^R(E)$) is given by

$$G_D^R(E) = [E - H_D - \Sigma_p^R(E) - \Sigma_q^R(E)]^{-1} \tag{4.11}$$

We now analyze the conditions under which the transistor effect can be observed in zP-NRs. The conductance, band structure, and wave functions of a 10-zPNRs for $E_{ext}=0$ and 0.016 V/Åare shown in Fig. 4.10. As can be seen in Fig. 4.10(b), the degeneracy between the two edge modes at zPNRs is slightly lifted close to $k = 0$. Therefore, the conductance is slightly asymmetric near $k = 0$. As shown in Fig. 4.10(c), the wave functions of the upper and lower quasi-flat bands are localized on both the edges. As the external electric field is increased up to a critical field, the overlap between these two bands vanishes. What we have is a conductance controlled by the external electric field at Fermi energy, which is a FET behavior. In this case, the wave functions of the upper and lower edge bands are localized on the opposite edges (Fig. 4.10(f)).
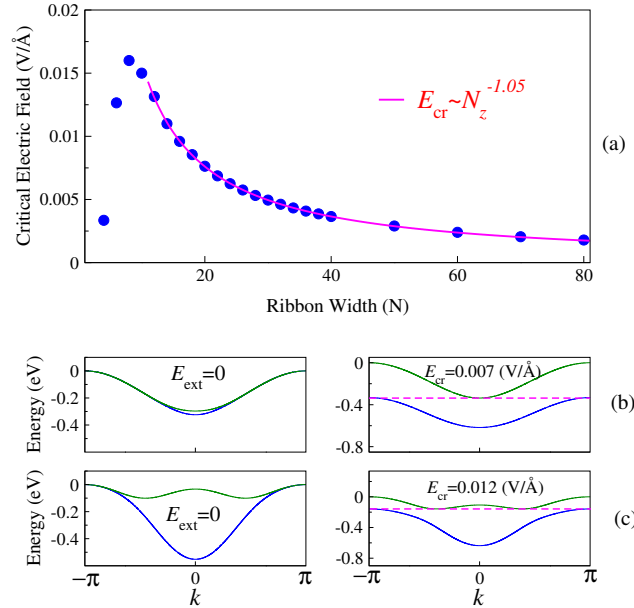
Figure 4.11: (a) Variation in critical transverse electric field with ribbon width of zPNRs. Quasi-flat bands for (b) 20-zPNR for $E_{ext} = 0$ and $E_{ext} = 0.007$ V/Å, and (c) 6-zPNR for $E_{ext} = 0$ and $E_{ext} = 0.012$ V/Å.

The relationship between E_c and ribbon width is shown in Fig. 4.11(a). For zPNRs with widths greater than $N_z = 14$, E_c scales as $1/N_z^{1.05}$, which is in good agreement with the results previously reported by Ezawa [76]. However, for ribbons with widths smaller than $N_z = 14$, we found a completely different behavior. To explain this portion of the graph, we considered the behavior of the edge bands of zPNRs with different widths. Figs. 4.11(b) and (c) show the quasi-flat bands for 20-zPNR and 6-zPNR, respectively. For $E_{ext} = 0$, the quasi-flat bands are different for these two widths. The VBM and CBM of 20-zPNR are located at $k = \pi$ and $k = 0$, respectively. The VBM of 6-zPNR is also located at $k = \pi$ whereas the CBM is located at a k between 0 and π. This displacement of the CBM in 6-zPNR is caused by the finite interaction between the two edge modes. Therefore, a lower external electric field is needed for observing the transistor effect.

4.5   Conclusion

In summary, we presented the numerical results for the band structure and quantum conductance of zPNRs and aPNRs based on a five parameter TB model. It was shown that the general form of the electronic structure is controlled by the two dominant hopping param-

eters. It was discussed that the opposite sign of these two hopping integrals is the origin of the creation of a relativistic band dispersion along the armchair direction. Our numerical results for zPNRs predicts a pair of degenerate quasi-flat bands at the Fermi level that are localized on the ribbon edges, and this degeneracy is lifted for small ribbon widths owing to finite interactions between the edge states. Additionally, our calculations provide scaling laws of the band gap for PNRs as a function of ribbon width. We discussed that the band gap scaling law for both nanoribbons with widths much larger than 3.5 nm is always $1/w^2$. For aPNRs, a semiconducting behavior is predicted, and an insulator-metal transition can be expected when a transverse electric field is applied. In zPNRs, an external transverse electric field can remove the overlap between quasi-flat bands. The anisotropy in the mobility, tunability of the band gap with ribbon width, and the field dependent conductance makes this system a promising candidate for future FET technologies.

Magnetic field dependence of Landau levels in monolayer phosphorene

In this chapter, the basic aspects of low energy electrons and holes of MLP in the presence of a perpendicular magnetic field are discussed. The behavior of the system in the QH regime is in close relation with the characteristics of LLs. The primary goal of this chapter is to address the debating field dependence of LLs in MLP Using a simple approach, we will demonstrate that the LLs dependence on magnetic field is indeed as for conventional 2D semiconductor electron gases. We show that the results are valid up to the very high field regime. Then, we will discuss the conditions for which such a dependence can continuously evolve into another field dependence.

5.1 Introduction

In the broad research area of condensed matter physics, the theoretical and experimental study of IQHE and FQHE in exotic 2D layered materials is a subject of interest. The intense interest in this field of research owes to the fact that it can pave the way for more elucidation of many important features of quantum physics and interacting systems. Moreover, it has also provided a new quantum mechanical metric standard that depends only on the fundamental constants of Planck's constant, h, and electron charge, e [207].

It has been shown that the behavior of zero-field electronic spectrum of a 2D system affects dramatically the dependence of LLs on magnetic field [74]. For example, it was shown that

in a system with linear-quadratic spectrum, the dependence of LLs on the magnetic field is neither linear in the conventional limit nor as $(nB)^{1/2}$ in the Dirac limit [68, 74]. For such a dispersion, the LL energies scale as $(n + 1/2)^{3/2}$ where n is the LL index [68, 74]. The quest for samples with higher mobility has motivated the researchers to investigate the QHE as a prototypical 2D phenomenon in monolayer and few-layer phosphorene [63]. The LLs and the QHE has been studied both theoretically and experimentally in few-layer black phosphorous [63–73]. The highly anisotropic physics in many properties of phosphorene are closely related to its band structure which is Dirac-like in one direction and Schrödinger like in the other direction [44, 72, 75, 76]. Therefore, one might expect to observe a behavior as $B^{2/3}$ in the LLs field dependence. But, there exist other theories arguing that such behavior is not correct [63, 69–71, 73]. Within the framework of the effective $\boldsymbol{k} \cdot \boldsymbol{p}$ Hamiltonian and TB model, they have shown that LLs in phosphorene behave like conventional semiconductor 2D electron gases [69–71, 73] which results in the usual QHE. It has been also argued that the emergence of the mentioned LLs field dependence can be observed in FLP in the presence of electric field [71]. However, due to the mentioned highly anisotropic electronic structure, determining the LLs field dependence is still under theoretical debate.

In this chapter, we study the debating field dependence of LLs in MLP. Using an effective low-energy continuum spectrum derived from the TB model of MLP and a simple approach, we will demonstrate that the LLs dependence on magnetic field is indeed as for conventional 2D semiconductor electron gases. This is in accordance with the second view at least up to very high field regime. Next, we will discuss the conditions under which such a dependence can continuously evolve to the first view.

5.2   Effective low-energy Hamiltonian of MLP

We have shown in Fig. 6.1 the structure parameters of MLP that we have used in this chapter. We have chosen the x and y axes align to armchair and zigzag directions, respectively and the z axis is in the normal direction to the plane of phosphorene. With this definition of coordinates, one can indicate the various atom connections r_i. The structure parameters have been taken from [32] which is very close to experimentally measured parameters [208] for its bulk structure. The components of the geometrical parameters for bond lengths $r_1 = 2.240$ Å and $r_2 = 2.280$ Å are $(r_{1x}, r_{1y}, r_{1z}) = (1.503, 1.660, 0)$ and $(r_{2x}, r_{2y}, r_{2z}) = (0.786, 0, 2.140)$. The two in-plane lattice constants are $a = 4.580$ Å, and $b = 3.320$ Å, and the thickness of a single layer due to the puckered nature is $r_{2z} = 2.140$ Å.
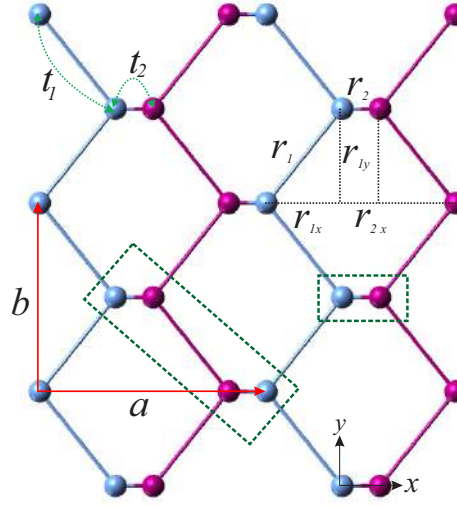
Figure 5.1: The lattice geometry of phosphorene. The two different colors of the P atoms refer to upper and lower chains. Lattice constants and the components of geometrical parameters describing the structure of phosphorene are shown. The hopping parameters t_1 and t_2 used in our TB model are indicated in the figure. Green dashed rectangles show the unit cells of phosphorene.

There exist many studies [29, 30, 209] show that the low-energy electron states near the gap region, are well described by considering only one effective p_z-like orbital per lattice site. The proposed single-orbital TB model of MLP in Ref. [30], involves ten different hopping parameters that are also usable as intra-layer hopping parameters of the FLP or its bulk structure. However, it has been shown [29, 30, 76, 209] that the main aspects of the low-energy spectrum of the MLP, such as energy gap evaluation and bands curvature are well described by only two dominant energy hopping integrals t_1 and t_2 (see Fig. 6.1). These parameters are defined as the hopping between the nearest neighbors align the zigzag and armchair directions respectively. Moreover, the energy bands curvature is a predominant factor that determine the field dependence of LLs in a system [74]. Therefore, it is good enough for our purpose to rewrite the TB Hamiltonian (4.1) as

$$\hat{H} = \sum_{i,j} t_{ij} c_i^{\dagger} c_j, \tag{5.1}$$

where $c_i^{\dagger}$ and c_j are creation and annihilation operators of p_z-like orbitals at sites ith and jth, and the hopping parameters t_{ij} run only over the two hopping parameters t_1 and t_2. As we will see in the following, such an approximation simplifies our analyses in addition to the fact that it does not affect our results based on the above mentioned reasons.

The unit cell of MLP is a rectangle containing four P atoms as shown in Fig. 6.1(a). Fourier transform of the Eq. (5.1) gives the general Hamiltonian in momentum space as

$$H = \sum_{\boldsymbol{k}} \psi_{\boldsymbol{k}}^{\dagger} H(\boldsymbol{k}) \psi_{\boldsymbol{k}}, \tag{5.2}$$

where we have used the basis $\psi_{\boldsymbol{k}}^{\dagger} = \{A_{\boldsymbol{k}}^{\dagger}, B_{\boldsymbol{k}}^{\dagger}, C_{\boldsymbol{k}}^{\dagger}, D_{\boldsymbol{k}}^{\dagger}\}$ with $A_{\boldsymbol{k}}^{\dagger} = \mathcal{N}^{-1/2} \sum_{i} e^{i \boldsymbol{k} \cdot \boldsymbol{r}_i} A_i^{\dagger}$, and so on. Here, $\boldsymbol{k}$ is the Bloch momentum, and $\boldsymbol{r}_i$ is the orbital position with respect to the origin of coordination system located at the position of atom A. The kernel Hamiltonian $H(\boldsymbol{k})$ in Eq. (5.2) is represented as

$$H(\boldsymbol{k}) \;=\; \begin{pmatrix} 0 & h_{12}(\boldsymbol{k}) & 0 & h_{14}(\boldsymbol{k}) \\ h_{12}^{*}(\boldsymbol{k}) & 0 & h_{14}^{*}(\boldsymbol{k}) & 0 \\ 0 & h_{14}(\boldsymbol{k}) & 0 & h_{12}(\boldsymbol{k}) \\ h_{14}^{*}(\boldsymbol{k}) & 0 & h_{12}^{*}(\boldsymbol{k}) & 0 \end{pmatrix}, \tag{5.3}$$

whose elements are given by

$$\begin{aligned} h_{12}(\boldsymbol{k}) &= t_2 e^{i k_x r_{2x}} \\ h_{14}(\boldsymbol{k}) &= 2 t_1 e^{-i k_x r_{2x}} \cos(k_y r_{1y}). \end{aligned} \tag{5.4}$$

Using the Eqs. (5.3) and (5.4), we have obtained the two hopping integrals t_1 and t_2 by simply fitting the TB bands of phosphorene with the DFT data [30]. The obtained numerical values of these parameters are $t_1 = -1.170$ eV and $t_2 = 3.267$ eV. As shown in Fig. 5.2, there exist a good agreement between the TB results and the DFT bands for the low-energy spectrum. This demonstrates the validity of the model near the gap region, allowing us to remarkably simplify our calculations. Due to the D_{2h} point group invariance of MLP lattice [210], one can reduce the four-band model to a two-band Hamiltonian as

$$\mathcal{H}(\boldsymbol{k}) = \begin{pmatrix} 0 & h_{12}(\boldsymbol{k}) + h_{14}(\boldsymbol{k}) \\ h_{12}^{*}(\boldsymbol{k}) + h_{14}^{*}(\boldsymbol{k}) & 0 \end{pmatrix}. \tag{5.5}$$

This form of Hamiltonian allows us to simply do our calculations in order to determine the field dependence of LLs as follows. By expanding the Hamiltonian matrix elements in the vicinity of Γ point, one can write a continuum approximation. Retaining the terms up to the leading non-zero order of k_x and k_y, the continuum model is given by

$$\mathcal{H}(\boldsymbol{k}) = (\alpha + \beta k_y^2)\boldsymbol{\sigma}_x - \gamma k_x \boldsymbol{\sigma}_y, \tag{5.6}$$
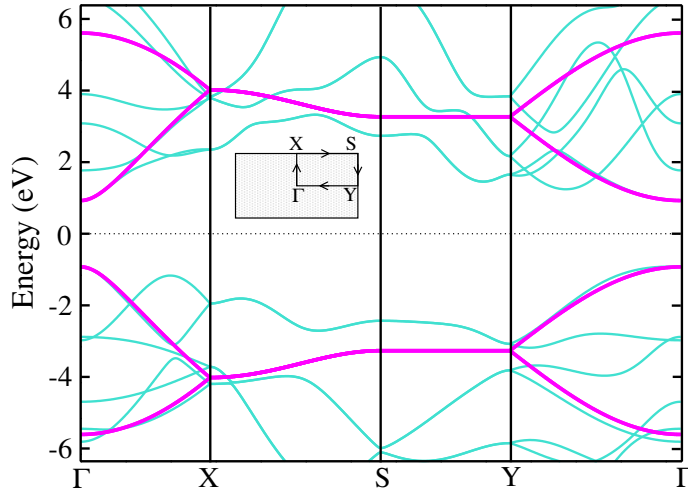
Figure 5.2: The obtained TB bands (magenta lines) from Eq. (5.1) compared to the DFT bands (cyan lines) taken from [30].

demonstrating that the spectrum has relativistic nature along the k_x direction, while it is parabolic along the k_y direction. In this equation, $\boldsymbol{\sigma}_x$ and $\boldsymbol{\sigma}_y$ are Pauli matrices and α, β and γ are given by

$$
\begin{aligned}
\alpha &= 2t_1 + t2, \\
\beta &= -t_1 r_{1y}^2, \\
\gamma &= -2t_1 r_{1x} + t_2 r_{2x},
\end{aligned}
\tag{5.7}
$$

whose numerical values are: $\alpha = 0.925$ eV, $\beta = 3.20$ eV·Å^2 and $\gamma = 5.765$ eV·Å. The continuum spectrum relations for electrons and holes are then simply given by

$$
E(k_x, k_y) = \pm\sqrt{(\alpha + \beta k_y^2)^2 + \gamma^2 k_x^2},
\tag{5.8}
$$

with an energy band gap of $E_g = 2\alpha = 1.85$ eV at the Γ point.
A comparison between the low-energy spectrum of the TB and continuum approximation is shown in Fig. 5.3. The good agreement between the two approaches for energies in the range -1.5 to 1.5 eV is clear. Note that, due to ignoring the further hopping terms [30], we have lost the weak electron-hole asymmetry of the energy spectrum. This, reflects itself as a small error to the effective masses of electrons and holes [70]. Thus, from the dispersion relation of Eq. (5.27) the effective masses of electrons and holes for the x and y directions are estimated as

$$
m_x^{e,h} = \pm\frac{\hbar^2}{2\gamma^2}, \quad m_y^{e,h} = \pm\frac{\hbar^2}{2\beta},
\tag{5.9}
$$
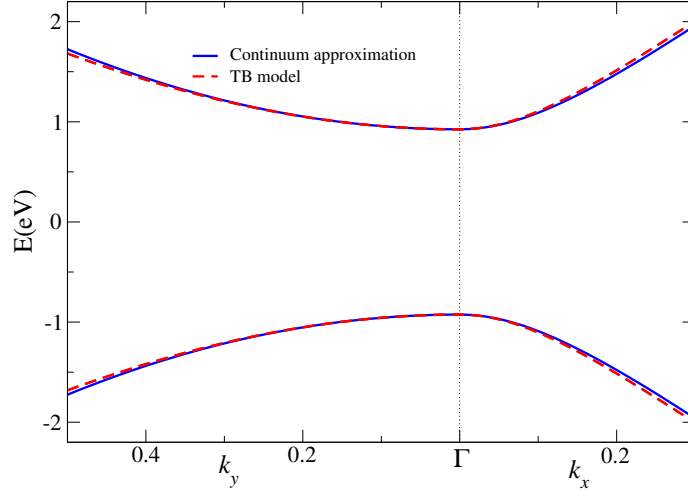
Figure 5.3: The low-energy spectrum of MLP from the continuum approximation and TB model.

where the resulting effective masses in terms of the free electron mass m_0 are $m_x^{e,h} = \pm 0.11 m_0$ and $m_y^{e,h} = \pm 1.19 m_0$ consistent with other results [70, 211]. This implies the existence of a strong anisotropy in the electronic properties of phosphorene that determines the main features of the corresponding properties. Therefore, one can neglect the minimum error arise by the above mentioned reason.

5.3   LLs of MLP

Let us now consider the continuum Hamiltonian of MLP in the presence of perpendicular magnetic field $\boldsymbol{B}$. Using the gauge $\boldsymbol{A} = (0, Bx, 0)$ and the substitution $k_y \to k_y + \ell_B^{-2} x$, the new Hamiltonian is given by

$$\mathcal{H}(\boldsymbol{k}, B) = (\alpha + \beta \eta^2 \tilde{x}^2)\boldsymbol{\sigma}_x - \gamma k_x \boldsymbol{\sigma}_y. \tag{5.10}$$

Here, ℓ_B is the magnetic length which is defined as $\ell_B^{-2} \equiv \eta = eB/\hbar$, and we have defined the new variable $\tilde{x} = k_y/\eta - x$. Squaring the Eq. (5.10), and after some algebraic calculations we arrive at

$$\mathcal{H}^2(\boldsymbol{k}, B) = \gamma^2 k_x^2 + (\alpha + \beta \eta^2 \tilde{x}^2)^2 + i\beta\gamma\eta[k_x, \tilde{x}^2]\boldsymbol{\sigma}_z, \tag{5.11}$$

where σ_z is the z-component of the Pauli matrices. Using the commutation relation $[k_x, \tilde{x}] = -i$, we define the dimensionless variables $X = \tilde{x}/\varepsilon$ and $P = \varepsilon k_x$ so that

they satisfy the commutation relation $[P, X] = -i$. Substituting these new variables in Eq. (5.11) gives

$$\mathcal{H}^2(\boldsymbol{k}, B) = C\big(P^2 + (\delta + X^2)^2 + i[P, X^2]\boldsymbol{\sigma}_z\big), \tag{5.12}$$

where $C = (\beta\eta^2\gamma^2)^{2/3}$, $\delta = \alpha/\sqrt{C}$, and $[P, X^2] = -2iX$. This implies that it is enough to solve an effective Schrödinger equation with the effective potential of

$$V_{eff}(X) = \delta^2 + 2\delta X^2 + X^4 + 2X\boldsymbol{\sigma}_z, \tag{5.13}$$

where the dimensionless variable δ acts as an effective gap and equals to

$$\delta = \frac{\alpha}{[\beta\gamma^2 B^2(e/\hbar)^2]^{1/3}} = \frac{E_g}{2[\beta\gamma^2 B^2(e/\hbar)^2]^{1/3}}. \tag{5.14}$$

Thus, the eigenvalues of the Schrödinger equation $\mathcal{H}(\boldsymbol{k}, B)\Psi_n^{e,h} = \mathcal{E}_n\Psi_n^{e,h}$ are simply related to the eigenvalues E_n of the square Hamiltonian (5.12) via

$$\mathcal{E}_n = \pm(\beta\eta^2\gamma^2)^{1/3}\sqrt{E_n}. \tag{5.15}$$

The quartic form of the effective potential (5.13) in which its low-energy barrier shape is strongly dependent on the effective gap δ is crucial in determining the field dependence of LLs. This implies that in addition to the bands curvature, the energy band gap is also an important factor in determining field dependence of LLs. In order to calculate the LLs spectra of MLP, one can substitute the magnetic length $\ell_B = 256.5/\sqrt{B(\text{Tesla})}$ Å (the magnitude of B is written in the unit of Tesla), and the numerical values of the structural parameters (5.7) in Eq. (5.14) to obtain the dimensionless gap δ as

$$\delta \approx \frac{264.0}{B^{2/3}(\text{Tesla})}. \tag{5.16}$$

This shows that even in the presence of a whopping strength of magnetic field up to $\sim 150\text{T}$ we have $\delta \gg 1$. Thus, even in the presence of very high magnetic field strengths, one can use the low-energy limit of effective potential

$$V_{l-eff}(X) = \delta^2 + 2\delta X^2 \tag{5.17}$$

(see Fig. 5.4) to find the energy levels of

$$\Big(-\frac{d^2}{dX^2} + (\delta^2 + 2\delta X^2)\Big)\psi_n = E_n\psi_n. \tag{5.18}$$
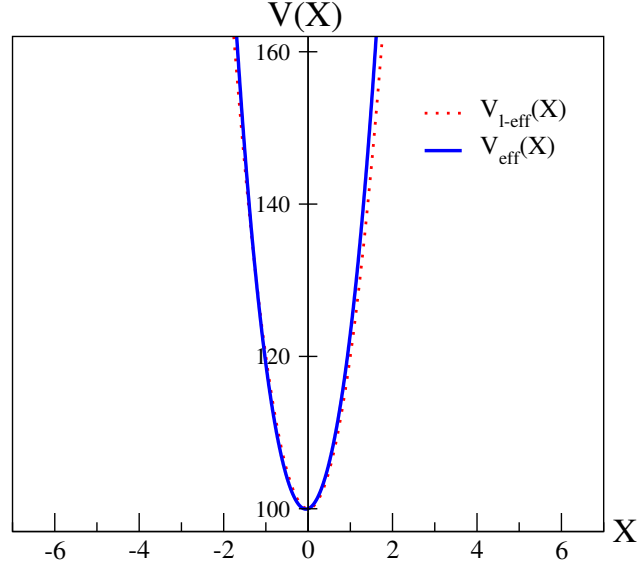
Figure 5.4: Comparison of the effective potentials $V_{eff}(X)$ and $V_{l-eff}(X)$.

As seen, Eq. (5.18) has a quadratic form with the spectrum of

$$E_n = \delta^2 + 2\sqrt{2}\delta(n + \frac{1}{2}).$$ (5.19)

Substituting this spectrum in Eq. (5.15) we arrive at

$$
\begin{aligned}
\mathcal{E}_n &= \pm\alpha\big(1 + \frac{2\sqrt{2}}{\delta\sqrt{\delta}}(n + \frac{1}{2})\big)^{1/2} \\
&\approx \pm\big(\alpha + \frac{\sqrt{2}}{\sqrt{\delta}}\frac{\alpha}{\delta}(n + \frac{1}{2})\big) \\
&= \pm\big(\alpha + \omega_c(n + \frac{1}{2})\big),
\end{aligned}
$$ (5.20)

where we have used Eq. (5.9) to define $\omega_c = eB/\sqrt{m_x m_y}$. This demonstrates that the LLs dependence on magnetic field is indeed as conventional 2D semiconductor electron gases. As seen, the results are valid up to very high field regime.

5.4 Effect of strain on LLs

The role of uniaxial and biaxial strain in manipulating the electronic structure of FLP been investigated via DFT [44–46, 50, 212] and TB approaches [47–49]. Applying tensile or

compressive strain in different directions results in different modifications of the electronic bands. One can observe a direct to indirect gap transition, or a prior direct band gap closing, depending on the type of applied strain [45, 46, 50]. Here, we consider equibiaxial compressive strain in the plane of MLP. This modifies the low energy bands so that the valance and conduction bands approach each other. This band evolution can affect the behavior of LLs of MLP. Investigating the local density of states of p orbitals [46] shows that the used one orbital p_z-like TB model is still valid in the low energy limit. In the following, we will first study the bulk band of phosphorene in the presence of equibiaxial compressive strains using our low-energy TB approach. Then, we will demonstrate that this will result to continuously evolution of LLs from a $(n+1/2)B$ dependence to a $[(n+1/2)B]^{2/3}$ dependence.

It has been shown that the bond lengths and bond angles of phosphorene both change under axial strains [45, 213]. Therefore, the hopping parameters will change. According to the Harisson rule [214], the hopping parameters for p orbitals are related to the bond length as $t_i \propto 1/r_i^2$ and the angular dependence can be described by the hopping integrals along the π and σ bonds. However, our calculations showed that, though the changes in angles are almost noticeable [45, 213], the modification of the hopping parameters due to them is much smaller than the effect of changes of bond lengths. Hence, we consider only changes of the bond lengths in the hopping modulation.

In the following, for simplicity we assume that the strengths of the applied biaxial strains in the two directions are equal, i.e., $\varepsilon_x = \varepsilon_y = \varepsilon$. When an equi-biaxial strain is applied to phosphorene, the rectangle shape of the unit cell with lattice constants of a_0 and b_0 remains unchanged. Therefore the initial geometrical parameter r_i^0 is deformed as $(r_{ix}, r_{iy}) = (1+\varepsilon)(r_{ix}^0, r_{iy}^0)$. In the linear deformation regime, expanding the norm of r_i to first order of ε gives

$$r_i = [1 + (\alpha_x^i + \alpha_y^i)\varepsilon]r_i^0, \tag{5.21}$$

where $\alpha_x^i = (r_{ix}^0/r_i^0)^2$, and $\alpha_y^i = (r_{iy}^0/r_i^0)^2$. Using the Harrison relation, we obtain the strain effect on the hopping parameters as

$$t_i \approx [1 - 2(\alpha_x^i + \alpha_y^i)\varepsilon)]t_i^0, \tag{5.22}$$

where t_i is the modified hopping parameter of deformed phosphorene with new lattice constants a and b. Let us now study the energy spectrum of strained phosphorene with the modified hopping parameters t_1 and t_2 as given by Eq. (5.22). The new k-space Hamiltonian of the strained phosphorene is given by

$$\mathcal{H}_{\text{strained}}(\boldsymbol{k}) = \begin{pmatrix} 0 & h_{12}(\boldsymbol{k}) + h_{14}(\boldsymbol{k}) \\ h_{12}^*(\boldsymbol{k}) + h_{14}^*(\boldsymbol{k}) & 0 \end{pmatrix}, \tag{5.23}$$

where h_{12} and h_{14} are now defined in terms of the modified hopping parameters. Diagonalizing this Hamiltonian at the Γ point gives the band gap as

$$E_g = (4t_1^0 + 2t_2^0) - \sum_j (8\alpha_j^1 t_1^0 + 4\alpha_j^2 t_2^0)\varepsilon, \qquad (5.24)$$

where j denotes the summation over x, y components. The first parentheses is the unstrained band gap i.e. $E_g^0 = 1.85$ eV and the second one indicates the structural dependent values of changes in the band gap due to the applying strain. Using the numerical values of the structural parameters in Eq. (5.24), the band gap evolution of MLP in the presence of compressive equi-biaxial strain is a linear function as

$$E_g = E_g^0 - s_0\varepsilon, \qquad (5.25)$$

where $s_0 = -8.2$ eV. This equation shows that by applying compressive equi-biaxial strain, the band gap decreases which is consistent with DFT calculations [44–46, 50, 212]. Now, the continuum model (5.6) is rewritten in terms of new coefficients α_ε, β_ε and γ_ε, whose values are

$$\begin{aligned} \alpha_\varepsilon &= \alpha_0 - \frac{1}{2}s_0\varepsilon, \\ \beta_\varepsilon &\approx \beta_0[1 - 2\varepsilon(s_1 - 1)] \approx \beta_0, \\ \gamma_\varepsilon &\approx \gamma_0 + \varepsilon[-2(1 - 2s_1)t_1^0 r_{1x}^0 + (1 - 2s_2)t_2^0 r_{2x}^0], \end{aligned} \qquad (5.26)$$

where we have defined $s_1 = \alpha_x^1 + \alpha_y^1 \approx 1.0$, and $s_1 = \alpha_x^2 + \alpha_y^2 \approx 0.12$. This leads to the strain dependent continuum spectrum of electrons and holes as

$$E(k_x, k_y, \varepsilon) = \pm\sqrt{(\alpha_\varepsilon + \beta_\varepsilon k_y^2)^2 + \gamma_\varepsilon^2 k_x^2}, \qquad (5.27)$$

which is defined over the modified BZ. Therefore, the energy spectra along the Γ-Y and Γ-X directions are given by

$$E(k_y, \varepsilon) = \pm(\alpha_\varepsilon + \beta_\varepsilon k_y^2), \qquad (5.28)$$

and

$$E(k_x, \varepsilon) = \pm\sqrt{\alpha_\varepsilon^2 + \gamma_\varepsilon^2 k_x^2}, \qquad (5.29)$$

respectively. Equation (5.28) explicitly shows that for an arbitrary strength of applied strain, the parabolic nature of bands along the Γ-Y direction remains unchanged. Whereas, Eq. (5.26) implies that by increasing its strength, the relativistic nature of bands along the

Figure 5.5: The comparison of the functions $f(\mu)$ and $f(\mu_0)$.

Γ-X direction becomes more rigorous. For the critical strain value ε_c, the energy gap is closed and electrons and holes become massless relativistic particles as

$$E(k_x, \varepsilon_c) = \pm\gamma_{\varepsilon_c} k_x. \tag{5.30}$$

Within the two-parameter TB approximation, such a dispersion corresponds to very large value of applied strain $\varepsilon_c \approx 22.5\%$ which is experimentally challenging. However, owing to the puckered structure of phosphorene, it has a high degree of flexibility. Therefore, it can sustain strain very well specially in the zigzag direction up to about 30% [42, 50]. As a result, the structure is still stable under such a strain.

Let us now consider the effect of applying a perpendicular magnetic field. In terms of the new strain modified hopping parameters one can rewrite Eq. (5.14) as

$$\begin{aligned} \delta(\mu) &= (\mu - 2)f(\mu)^{-1}\ell_B^{4/3}, \\ f(\mu) &= (r_{1y}r_{2x}\mu + 2r_{1y}r_{1x})^{2/3}, \end{aligned} \tag{5.31}$$

where $\mu = |t_2/t_1|$ shows the ratio of two strain modified hopping parameters. For unstrained phosphorene $\mu_0 \approx 2.78$. By applying strain up to the critical value ε_c, the values of μ ranges from 2.78 to 2. As can be seen in Fig. 5.5, the behavior of function $\delta(\mu)/\ell_B^{4/3}$ in this range of μ is similar to the case in which $f(\mu)$ is replaced by $f(\mu_0)$. As a result, by increasing the strength of applied strain, the behavior of strain dependent potential $V_{l-eff}(X)$ is mainly determined by the magnitude of $\mu - 2$ which is indeed the gap of the system. Therefore, in addition to the magnitude of applied magnitude field, the value of the band gap plays an important role in the shape of effective potential. At the critical value ε_c, Eq. (5.32) gives

$$V_{eff}(X) = X^4 + 2X\boldsymbol{\sigma}_z. \tag{5.32}$$

It has been shown that the effect of the linear term in this potential is negligible [74] and the effective potential is indeed related to a quartic oscillator which has been discussed in
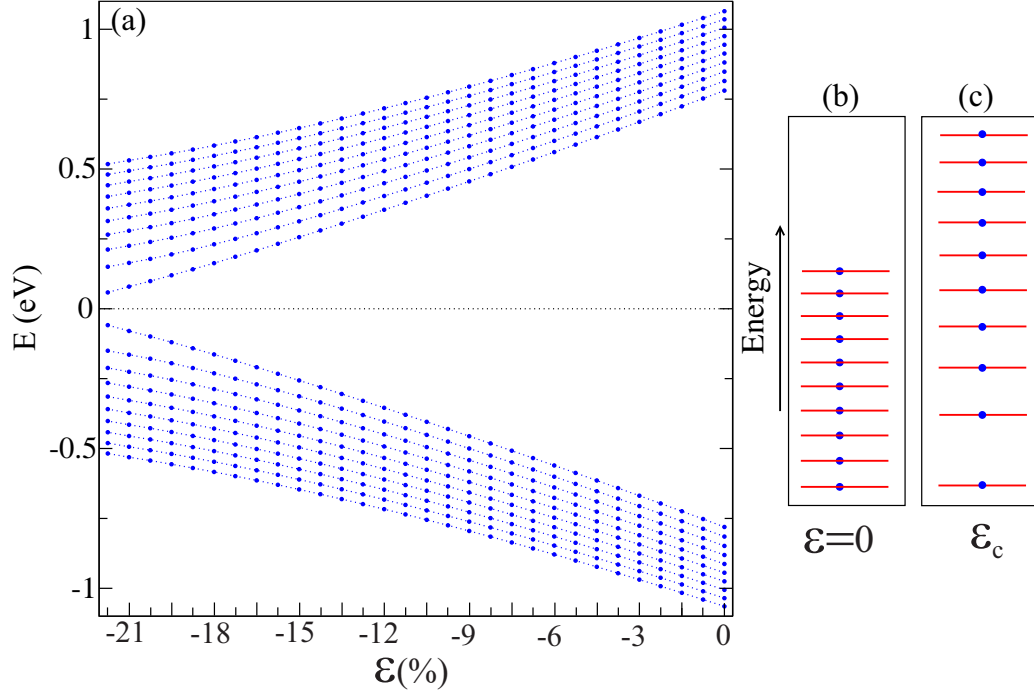
Figure 5.6: (a) The LLs of MLP as a function of biaxial strain. (b) and (c) show equidistant LLs for unstrained phosphorene and $B^{3/2}$ dependence of LLs at the critical value ε_c, respectively.

Ref. [74]. It has been shown that the quantized energy levels of this system follows the field dependence of $[(n+1/2)B]^{3/2}$. As a result, we have shown that by applying compressive equi-biaxial strain, one can continuously evolve the field dependence of LLs from a linear to $B^{3/2}$ dependence. We have numerically obtained the LLs of MLP as a function of equi-biaxial strain as shown in Fig. 5.6. Figures 5.6(b) and (c) show equidistant LLs for unstrained phosphorene and non-equidistant LLs at the critical value ε_c, respectively.

5.5   Conclusions

In this chapter, the salient features of the electronic band dispersion of MLP in determining the dependence of LLs on magnetic field were discussed. The primary goal was to address the field dependence of LLs in MLP. Using the continuum low energy Hamiltonian of the system, we demonstrated that the dependence of the LLs on magnetic field is indeed as for conventional 2D semiconductor electron gases. We showed that the results are valid up to very high field. Then, we studied the effect of applying compressive equi-biaxial strain on the TB Hamiltonian of MLP and obtained a strain dependent low

energy continuum model. We showed that for an arbitrary strength of compressive strain, the parabolic nature of bands along the Γ-Y direction remains unchanged. Whereas, by increasing its strength, the relativistic nature of bands along the Γ-X direct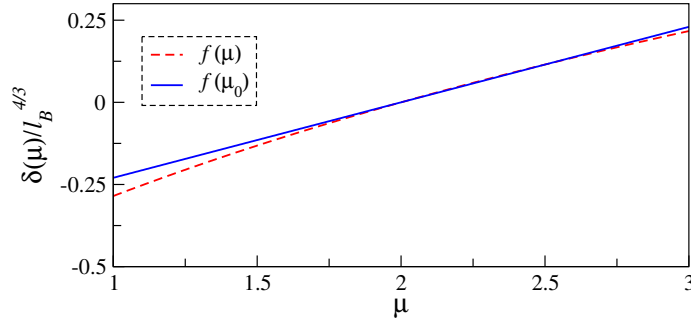ion becomes more clear. For the critical strain value ε_c, the energy gap is closed and electrons and holes become massless relativistic particles. Using this continuum model, we demonstrated that one can continuously evolve the field dependence of LLs from linear to $[(n + 1/2)B]^{3/2}$ dependence.

CHAPTER 6

Strain-induced topological phase transition in phosphorene

In this chapter, using the TB approximation with inclusion of the spin-orbit interaction, we predict a topological phase transition in the electronic band structure of phosphorene in the presence of axial strains. We derive a low-energy TB Hamiltonian that includes the spin-orbit interaction for bulk phosphorene. Applying a compressive biaxial in-plane strain and perpendicular tensile strain in ranges where the structure is still stable leads to a topological phase transition. We also examine the influence of strain on zPNRs and the formation of the corresponding protected edge states when the system is in the topological phase. For zPNRs up to a width of 100 nm the energy gap is at least three orders of magnitude larger than the thermal energy at room temperature.

6.1   Introduction

In chapter (3), we briefly addressed the theory of topological band insulators. We concluded that the emergence of robust edge states in 2DTIs that are protected by TRS, make them promising candidates for potential applications in spintronics and quantum computing [57, 121, 124–126, 137].TIs can exist intrinsically or be driven by external factors such as electrical field or by functionalization [215]. Strain engineering is a well known strategy for switching from NI phase to a TI phase [215, 216]. Among the wide list of systems that possesses such property, 2D materials with fascinating electronic, mechanical and thermal

properties have been in the focus of attention [57, 217].

In the past few years, phosphorene, a monolayer of black phosphorus, has emerged as an encouraging 2D semiconducting material for widespread applications. Phosphorene-based field effect transistors (FETs), show a higher ON/OFF ratio in comparison with graphene [218, 219] and has a higher carrier mobility with respect to TMDs which have recently attracted a lot of attention for FET applications [8, 218, 219]. There exist several works pertinent to the observation of different phases in bulk and multilayer black phosphorous by tuning the lowest energy bands [46, 77, 79, 81, 220]. Using DFT it was shown that few-layers of phosphorene experiences a NI to TI and then a TI to topological metal (TM) phase transition by applying a perpendicular electric field [79]. In a different DFT study [46] such phase transitions for various stacked bilayer phosphorene under in-plane strain has been explored. As we mentioned in the previous chapter the monolayer of phosphorene can sustain strain very well up to about 30% [42, 50]. This makes phosphorene promising for possible applications using strain engineering.

In the present chapter, we investigate the effect of strain on the electronic band structure of phosphorene within the TB approach. The band gaps of this model [29] are close to the most reliable DFT and experimental results [25, 33] that predict band gaps of $1 \sim 2$ eV for phosphorene. In this study, we propose a model Hamiltonian for the SOC for MLP that can be generalized to FLP. We show that, a model which includes the next-nearest(n-n) neighbors in the upper or lower chains, is sufficient for capturing the main physics. Then, strain engineering of this system is investigated through modifying the hopping parameters of the system. We demonstrate that, by applying particular types of strain, the system can make a phase transition to a TI. Finally, we show numerically that though the topological bulk band gaps induced by SOC is about 5 meV, but the highly anisotropic nature of this material causes the corresponding bulk gaps in large widths zPNRs be at least three order of magnitude larger than room temperature thermal energy (~ 26 meV) and makes PNRs excellent candidates for future applications.

The chapter is organized as follows: the effective low-energy TB model Hamiltonian including the SOC terms is obtained in Sec. 6.2 The effect of axial strains on the band structure produced by this model is calculated and our results are compared with DFT results in Sec. 6.3. Demonstration of a topological phase transition in the electronic properties of phosphorene when particular types of strain are applied and the characteristics of corresponding edge states in zPNRs is presented in Sec. 6.4. The conclusion is given in Sec.6.5.

6.2   Tight-binding model including spin-orbit interaction

We have shown in Fig. 6.1 the used coordinate system to describe the puckered atomic structure of phosphorene and its geometrical parameters. x and y axes are the armchair
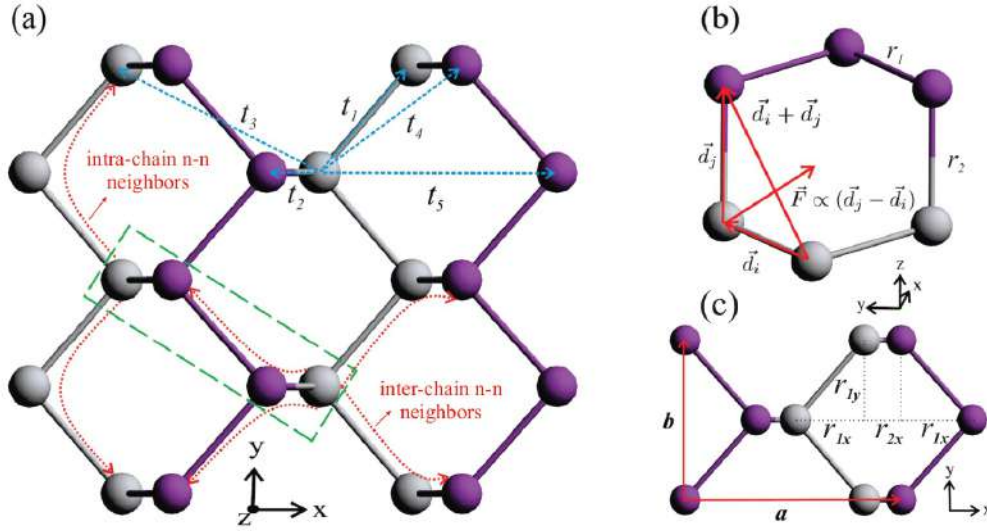
Figure 6.1: The lattice geometry of phosphorene. The two different colors of the P atoms refer to upper and lower chains (a) The hopping parameters $t_1, t_2, ..., t_5$ used in our TB model are indicated in the figure. Red dotted arrows represent two types of n-n neighbors and the green dashed rectangle shows the unit cell of phosphorene. (b) A honeycomb-like ring of phosphorene. The vectors $\vec{d_i}, \vec{d_j}$, $\vec{d_i} + \vec{d_j}$ and $\vec{F} \propto (\vec{d_j} - \vec{d_i})$ are used to derive the SOC. (c) Lattice constants and the components of geometrical parameters describing the structure of phosphorene.

and zigzag directions, respectively and the z axis is in the normal direction to the plane of phosphorene. With this definition of coordinates, one can indicate the various atom connections r_i which correspond to various hopping parameters t_i that are included in the TB model. The structure parameters have been taken from [32] which is very close to experimentally measured parameters [208] for its bulk structure. The components of the geometrical parameters as shown in Figs. 6.1(b) and (c), for bond lengths $r_1 = 2.240$ Å and $r_2 = 2.280$ Å are $(r_{1x}, r_{1y}, r_{1z}) = (1.503, 1.660, 0)$ and $(r_{2x}, r_{2y}, r_{2z}) = (0.786, 0, 2.140)$, and r_3, r_4, r_5 are simply defined by parameters of r_1 and r_2. The two in-plane lattice constants are $a = 4.580$ Å, $b = 3.320$ Å and the thickness of a single layer due to the puckered nature is $r_{2z} = 2.140$ Å.

6.2.1   Tight-binding model

Including the spin degree of freedom and SOC, the Hamiltonian (4.1) is modified into

$$\hat{H} = \sum_{i,j,\alpha} t_{ij} c_{i\alpha}^\dagger c_{j\alpha} + \hat{H}_{SO}, \tag{6.1}$$

where α denotes the spin of electrons. In $\hat{H}_{SO} = \hat{H}_{SO1} + \hat{H}_{SO2}$, the first term is called the usual effective SOC and the second one is the intrinsic Rashba SOC which will be introduced in next subsection. Due to the puckered structure of phosphorene, the Rashba term is rather large as compared to the first term and should be included in our calculations.

6.2.2 Spin-orbit coupling in Phosphorene

The primary goal of this subsection is to introduce a spin-orbit model Hamiltonian for phosphorene which can capture the most important spin-related phenomenon. There exist several studies which showed the anisotropic behaviour in the electronic and optical properties of phosphorene [33, 211, 221, 222] which are due to the anisotropic nature of the band dispersion of phosphorene. This property is reflected in the effective mass of electrons and holes of phosphorene. As a matter of fact, the corresponding band dispersion of the zigzag direction in real space, is relatively flat near the Fermi energy while it has an approximately linear dispersion in the armchair direction [211, 221]. One can define two types of n-n neighbors in the phosphorene structure. As shown in Fig. 6.1(a), each P atom has two intra-chain and four inter-chain n-n neighbors, respectively. The effective mass of electrons in the direction of intra-chain, are at least an order of magnitude larger than the inter-chain direction [221]. Therefore, electrons usually select the inter-chain path for circular motion, allowing us to ignore the intra-chain neighbors and only consider the four n-n inter-chain P atoms in the SOC model.

In general, the SOC term for a 2D system is given by

$$H_{SO} = -\frac{\hbar}{4m_0^2 c^2}(\vec{F} \times \vec{P}) \cdot \vec{\sigma}, \qquad (6.2)$$

where $\hbar$, m_0 and c are Plank's constant, mass of free electron, and the velocity of light, respectively. $\vec{F}$ is the effective electrostatic force, $\vec{P}$ is the effective momentum and $\vec{\sigma}$ denotes the Pauli matrices. As in the cases of graphene and silicene [223], the nearest-neighbor SOC is zero in phosphorene, but the SOC terms of the n-n neighbors are nonzero. As shown in Fig. 6.1(b), in a honeycomb-like ring of phosphorene, we can define $\vec{d_i}$ and $\vec{d_j}$ as vectors that connect the nearest P atoms to each other and $\vec{d_i} + \vec{d_j}$ the connecting vector of n-n neighbors. Using these vectors, the electrostatic force and momentum can be written as $\vec{F} = |\vec{F}|(\vec{d_j} - \vec{d_i})/|\vec{d_j} - \vec{d_i}|$ and $\vec{P} = -i\hbar\vec{\nabla} \equiv -i\alpha(\vec{d_i} + \vec{d_j})$, with α being a prefactor. Rewriting the SOC in terms of the above definitions we obtain

$$H_{SO} = -\frac{\hbar}{4m_0^2 c^2}\left[\frac{|\vec{F}|(-i\alpha)}{|\vec{d_j} - \vec{d_i}|}(\vec{d_j} - \vec{d_i}) \times (\vec{d_i} + \vec{d_j})\right] \cdot \vec{\sigma}. \qquad (6.3)$$

Based on experimental and DFT data, $|\vec{d_i}|$ and $|\vec{d_j}|$ are approximately equal [32, 42, 194, 208], therefore $(\vec{d_i} + \vec{d_j})$ and $(\vec{d_j} - \vec{d_i})$ become perpendicular to each other. This leads to

$$H_{SO} = -i\frac{2\hbar\alpha|\vec{F}|}{4m_0^2 c^2 |\vec{d_j} - \vec{d_i}|}(\vec{d_i} \times \vec{d_j}) \cdot \vec{\sigma} \equiv -i\gamma(\vec{d_i} \times \vec{d_j}) \cdot \vec{\sigma}, \qquad (6.4)$$

where the term $2\hbar\alpha|\vec{F}|/4m_0^2 c^2 |\vec{d_j} - \vec{d_i}| = \gamma$ will be adjusted to obtain the correct value of SOC as obtained by DFT. Notice that the above approximations reduce the two parameters of the usual SOC and intrinsic Rashba SOC into a single parameter. Using $\vec{\sigma} = \sigma_{\shortparallel}\hat{a}_{\shortparallel} + \sigma_z\hat{a}_z$, where $\sigma_{\shortparallel}$ (σ_z) are the in-plane (out of plane) Pauli matrices (matrix), we rewrite Eq. (6.4) as

$$H_{SO} = -i\gamma|\vec{d_i} \times \vec{d_j}|_z \nu_{ij}\sigma_z - i\gamma|(\vec{d_i} \times \vec{d_j})_{\shortparallel}|(\vec{d_i} \times \vec{d_j})_{\shortparallel}^0 \cdot \vec{\sigma}_{\shortparallel}, \qquad (6.5)$$

where $\nu_{ij} \equiv (\vec{d_i} \times \vec{d_j})_z/|\vec{d_i} \times \vec{d_j}|_z = \pm 1$ and $(\vec{d_i} \times \vec{d_j})_{\shortparallel}^0 \equiv (\vec{d_i} \times \vec{d_j})_{\shortparallel}/|(\vec{d_i} \times \vec{d_j})_{\shortparallel}|$ is a dimensionless unit vector. The spin-orbit terms in second quantization are given by

$$\hat{H}_{SO1} + \hat{H}_{SO2} = -i\lambda_{so} \sum_{\ll ij \gg \alpha\beta} \nu_{ij} c_{i\alpha}^\dagger \sigma_z^{\alpha\beta} c_{j\beta} - i\lambda_r \sum_{\ll ij \gg \alpha\beta} c_{i\alpha}^\dagger (\vec{d_i} \times \vec{d_j})^0 \cdot \vec{\sigma}_{\shortparallel}^{\alpha\beta} c_{j\beta}, \quad (6.6)$$

where $\lambda_{so} \equiv \gamma|\vec{d_i} \times \vec{d_j}|_z$ and $\lambda_r \equiv \gamma|(\vec{d_i} \times \vec{d_j})_{\shortparallel}|$ are effective intrinsic SOC and intrinsic Rashba constants, and the summation runs over the inter-chain n-n neighbors. As mentioned before, these two parameters are related to one parameter γ, which can be estimated by adjusting the TB band structure of phosphorene to the one obtained from DFT. It was shown that in the absence of SOC the energy gap of FLP closes under an external electric field or strain [46, 79]. However, including the SOC an energy gap of 5 meV [79] remains in FLP. This results in the value of $\gamma \approx 6$ meV/$\mathring{A}^2$ in our TB model.

6.3 Phosphorene under strain: electronic band structure

In the previous chapter, we studied the effect of applying a equi-biaxial strain on the energy spectrum of MLP. In this chapter, we consider global compressive strain in the plane of FLP [45, 46], and tensile strain in the normal direction [212]. Similarly, this modifies the low energy bands so that the valance and conduction bands approach each other. By further increasing strain, the lower band, coming from p_x orbitals, shifts upward resulting in a semi-metal phase [45] given that at the band crossing point a mini gap opens due to the SOC. Investigating the local density of states of p orbitals [46] shows that our one orbital

p_z-like TB model is still valid in the low energy limit before the semi-metal phase appears. In the following, we will first study the bulk band of phosphorene in the presence of axial strains using our TB approach and demonstrate that a band inversion occurs in the energy spectrum of phosphorene in the range where the structure is still stable under strain. Similar to the previous chapter, here we again use the Harrison rule and write the deformed geometrical parameter r_i in terms of the initial geometrical parameter r_i^0 as $(r_{ix}, r_{iy}, r_{iz}) = ((1 + \varepsilon_x)r_{ix}^0, (1 + \varepsilon_y)r_{iy}^0, (1 + \varepsilon_z)r_{iz}^0)$ where ε_j is the strain in the j-direction and r_i is a deformed geometrical parameter. In the linear deformation regime, expanding the norm of r_i to first order of ε_j gives

$$r_i = (1 + \alpha_x^i \varepsilon_x + \alpha_y^i \varepsilon_y + \alpha_z^i \varepsilon_z)r_i^0, \tag{6.7}$$

where $\alpha_j^i = (r_{ij}^0/r_i^0)^2$ are coefficients related to the structure of phosphorene which are simply calculated via the special geometrical parameters given in previous section. Using the Harrison relation, we obtain the strain effect on the hopping parameters as

$$t_i \approx (1 - 2\alpha_x^i \varepsilon_x - 2\alpha_y^i \varepsilon_y - 2\alpha_z^i \varepsilon_z)t_i^0, \tag{6.8}$$

where t_i is the modified hopping parameter of deformed phosphorene with new lattice constants a and b.

Let us now study the energy spectrum of strained phosphorene with the modified hopping parameters as given by Eq. (6.8). The unit cell of MLP is a rectangle containing four atoms as shown in Fig. 6.1(a). Fourier transform of the strained Hamiltonian of Eq. (6.1) gives the general Hamiltonian in momentum space as

$$H = \sum_{\mathbf{k}} \psi_{\mathbf{k}}^{\dagger} H_{\mathbf{k}} \psi_{\mathbf{k}}, \tag{6.9}$$

where we have used the basis $\psi_{\mathbf{k}}^{\dagger} = \{a_{\mathbf{k}}^{\dagger}, b_{\mathbf{k}}^{\dagger}, c_{\mathbf{k}}^{\dagger}, d_{\mathbf{k}}^{\dagger}\} \otimes \{\uparrow, \downarrow\}$ with $H_{\mathbf{k}}$ being

$$H_{\mathbf{k}} = \begin{pmatrix} H_{\mathbf{k}}(\uparrow\uparrow) & H_{\mathbf{k}}(\uparrow\downarrow) \\ H_{\mathbf{k}}(\downarrow\uparrow) & H_{\mathbf{k}}(\downarrow\downarrow) \end{pmatrix}, \tag{6.10}$$

where

$$\begin{aligned} H_{\mathbf{k}}(\uparrow\uparrow) &= H_{\mathbf{k}}^{(4)} + H_{\mathbf{k}}^{so}, \quad H_{\mathbf{k}}(\downarrow\downarrow) = H_{\mathbf{k}}^{(4)} - H_{\mathbf{k}}^{(so)}, \\ H_{\mathbf{k}}(\uparrow\downarrow) &= H_{\mathbf{k}}^{(R)}, \quad\quad\quad H_{\mathbf{k}}(\downarrow\uparrow) = H_{\mathbf{k}}^{\dagger (R)}, \end{aligned} \tag{6.11}$$

are 4×4 matrices

$$
H_{\mathbf{k}}^{(4)} = \begin{pmatrix} 0 & A_{\mathbf{k}} & B_{\mathbf{k}} & C_{\mathbf{k}} \\ A_{\mathbf{k}}^* & 0 & D_{\mathbf{k}} & B_{\mathbf{k}} \\ B_{\mathbf{k}}^* & D_{\mathbf{k}}^* & 0 & A_{\mathbf{k}} \\ C_{\mathbf{k}}^* & B_{\mathbf{k}}^* & A_{\mathbf{k}}^* & 0 \end{pmatrix},
$$

$$
H_{\mathbf{k}}^{(so)} = \begin{pmatrix} 0 & 0 & E_{\mathbf{k}} & 0 \\ 0 & 0 & 0 & -E_{\mathbf{k}} \\ E_{\mathbf{k}}^* & 0 & 0 & 0 \\ 0 & -E_{\mathbf{k}}^* & 0 & 0 \end{pmatrix},
$$

$$
H_{\mathbf{k}}^{(R)} = \begin{pmatrix} 0 & 0 & F_{\mathbf{k}} & 0 \\ 0 & 0 & 0 & F_{\mathbf{k}} \\ e^{i(k_a - k_b)} F_{\mathbf{k}} & 0 & 0 & 0 \\ 0 & e^{i(k_a - k_b)} F_{\mathbf{k}} & 0 & 0 \end{pmatrix}, \tag{6.12}
$$

whose elements are given by

$$
\begin{aligned}
A_{\mathbf{k}} &= t_2 + t_5 e^{-ik_a}, \\
B_{\mathbf{k}} &= 4t_4 e^{-i(k_a - k_b)/2} \cos(k_a/2) \cos(k_b/2), \\
C_{\mathbf{k}} &= 2e^{ik_b/2} \cos(k_b/2)(t_1 e^{-ik_a} + t_3), \\
D_{\mathbf{k}} &= 2e^{ik_b/2} \cos(k_b/2)(t_1 + t_3 e^{-ik_a}), \\
E_{\mathbf{K}} &= -2\lambda_{so} e^{-i(k_a - k_b)/2} \sin(k_a/2) \sin(k_b/2), \\
F_{\mathbf{K}} &= 4\lambda_r e^{(k_b - k_a)/2}(\cos(k_b/2) \cos(k_a/2) \cos(\theta) + i \sin(k_b) \sin(k_a) \sin(\theta)),
\end{aligned} \tag{6.13}
$$

with $k_a = \mathbf{k}.\mathbf{a}$, $k_b = \mathbf{k}.\mathbf{b}$ and $\theta = \arctan(r_{1y}/r_{1x})$.
The energy spectrum of pristine phosphorene including the effect of SOC and in the absence of strain has been obtained by numerical diagonalization of the TB Hamiltonian Eq. (6.9) in different symmetry directions as shown in Fig. 6.2(a). As can be seen, the space inversion symmetry and the TRS of phosphorene leads to the double spin degeneracy of each electronic bands. As seen in Fig. 6.2 the gap of phosphorene is located at the Γ point. At this point, the valence and conduction bands are degenerate and the change in the gap due to the SOC is very small as compared to the bulk gap. Since axial strain doesn't break TRS, the bands at this point remain degenerate. Therefore, when the bulk gap is modified by an external factor such as strain, we can safely use the spinless Hamiltonian demonstrating the general trend in changes of the gap. All P atoms in a unit cell have the same on-site energy, so we can project the position of upper and lower chains of phosphorene on a horizontal plane to reduce the spinless 4×4 Hamiltonian $H_{\mathbf{k}}^{(4)}$ into
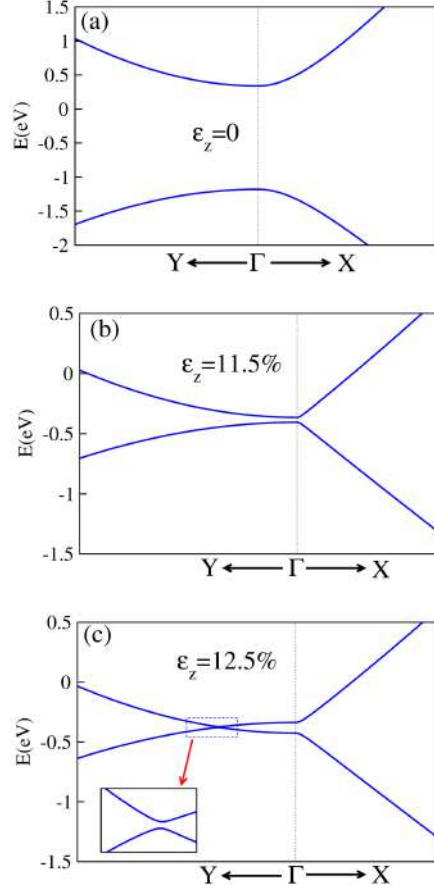
Figure 6.2: (a) The TB bands of phosphorene including the effect of SOC. (b), (c) The energy spectrum right before and after band inversion at 11.5% and 12.5% perpendicular tensile strain, respectively. The inset shows the gap opening due to the SOC, i.e. ~ 5 meV.

a two-band TB model [76, 211]. Therefore the new k-space Hamiltonian of the strained phosphorene in the absence of spin is given by

$$H_{\mathbf{k}}^{(2)} = \begin{pmatrix} B_{\mathbf{k}}e^{i(k_a-k_b)/2} & A_{\mathbf{k}} + C_{\mathbf{k}}e^{i(k_a-k_b)/2} \\ A_{\mathbf{k}}^* + C_{\mathbf{k}}^*e^{-i(k_a-k_b)/2} & B_{\mathbf{k}}e^{i(k_a-k_b)/2} \end{pmatrix}. \tag{6.14}$$

Diagonalizing this Hamiltonian at the Γ point gives the band gap as

$$E_g = (4t_1^0 + 2t_2^0 + 4t_3^0 + 2t_5^0) - \sum_j (8\alpha_j^1\varepsilon_j t_1^0 + 4\alpha_j^2\varepsilon_j t_2^0 + 8\alpha_j^3\varepsilon_j t_3^0 + 4\alpha_j^5\varepsilon_j t_5^0), \tag{6.15}$$

where j denotes the summation over x, y and z components. The first bracket is the unstrained band gap i.e. $E_g^0 = 1.52$ eV and the second one indicates the structural dependent
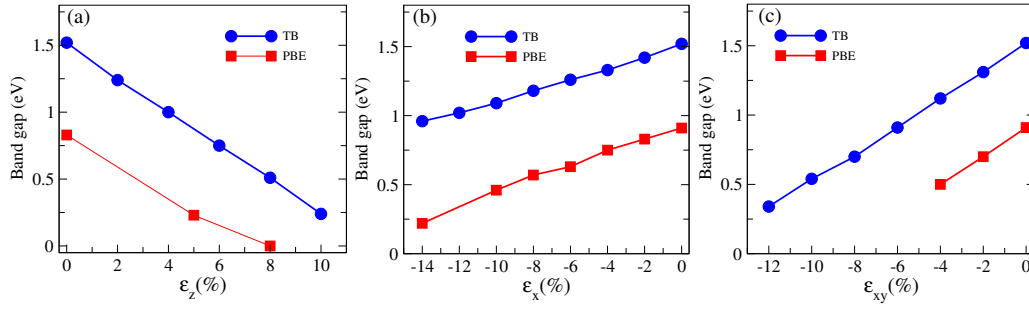
Figure 6.3: Band gap evolution of phosphorene in the presence of (a) perpendicular tensile strain, (b) uniaxial compressive strain in armchair direction, and (c) biaxial compressive in-plane strain.

values of changes in the band gap due to the axial strains. Inserting the numerical values of the structural parameters in Eq. (6.15) we obtain a compact form for the gap equation

$$E_g = E_g^0 - \sum_j \eta_j \varepsilon_j, \qquad (6.16)$$

where $\eta_x = -4.09$ eV, $\eta_y = -5.72$ eV and $\eta_z = 12.86$ eV. Eq. (6.16) shows that by applying in-plane compressive biaxial strain and perpendicular tensile strain, the band gap decreases which is consistent with DFT calculations [44–46, 50, 212]. It is shown that DFT calculations using the PBE exchange correlation functional anticipate properly the general trends of the band structure when applying axial strains on phosphorene [45, 50]. A comparison between the band gaps as function of axial strains using available DFT data [45, 50, 212] and TB model demonstrate that the modification of the hopping parameters in the linear regime are valid for rather large strains and show that the modified TB model predicts correctly the variation of the low energy spectrum. Figure 6.3 shows the band gap values evaluated at the Γ point in the presence of (a) uniaxial perpendicular tensile strain (b) uniaxial compressive strain in armchair direction, and (c) biaxial compressive in-plane strain, respectively. In both DFT and TB approaches the band gaps exhibit linear dependence with applied strain. The discrepancy between the values of the band gaps originate from the specific calculation method. As a particular case we consider the modification of the energy spectrum under a perpendicular tensile strain. By increasing the tensile strain, a band inversion occurs at the critical value of $\varepsilon_z^c = E_g^0/\eta_z = 0.118$. This is a signal of a topological phase transition. Figs. 6.2(b), (c) show the low energy bands just before and after band closing at 11.5% and 12.5% tensile strain, respectively. As shown in the inset of Fig. 6.2(c), the SOC opens a small gap of about 5 meV after band closing preventing the formation of a Dirac like-cone.

Notice from Figs. 6.2 that the low energy bands in the armchair direction become more
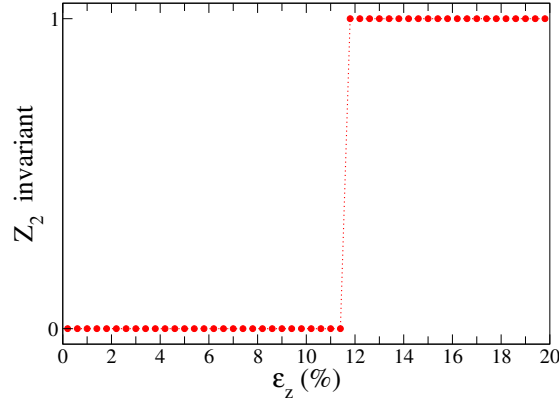
Figure 6.4: Calculation of $\mathbb{Z}_2$ invariant of phosphorene in the presence of perpendicular tensile strain. The critical value for the topological phase transition is 11.8%.

linear under strain. This makes the intra-chain n-n neighbours less important justifying the use of the SOC terms of Eq. (6.6).

6.4   Strain induced topological phase transitions in phosphorene

The $\mathbb{Z}_2$ classification provides a very strong distinction between two different time reversal topological and trivial phases. Pristine phosphorene as a trivial insulator when the intrinsic SOC effect is included preserves the TRS and can exhibit a QSH phase when its electronic properties is influenced by external factors e.g. electric field or strain.

Equation (3.4) for numerical computing the $\mathbb{Z}_2$ invariant, when working in the frame of the TB model [163] is quite efficient for 2D materials such as phosphorene. In what follows, we will demonstrate numerically a topological phase transition in strained phosphorene and calculate the phase diagrams accordingly.

Figure 6.4 shows the obtained numerical results of $\mathbb{Z}_2$ corresponding to the energy bands in Fig. 6.2. As can be seen, at the critical strain of 11.8%, which is consistent with the condition of $\varepsilon_z > E_g^0/\eta_z$ for band inversion, the $\mathbb{Z}_2$ invariant jumps from 0 to 1. This, demonstrates a topological phase transition in the electronic properties of phosphorene. According to Eq. (6.16), another way to observe a topological phase transition in phosphorene, is by applying in-plane compressive biaxial strain at a fixed value of tensile strain in the z direction. Figs. 6.5 show the numerically computed $\mathbb{Z}_2$ phase diagrams as a function of ε_x and ε_y at a fixed value of ε_z. As can be seen, there is a linear border between two distinct topological phases that corresponds to the regimes before and after the gap closing

condition of $\eta_x \varepsilon_x + \eta_y \varepsilon_y = E_g^0 - \eta_z \varepsilon_z^c$, where ε_z^c is a fixed value of strain in the direction of z.

It is worth mentioning that, the relatively large bulk band gap of MLP necessitates a rather large value of strain in order to observe band inversion. As mentioned before, according to DFT calculations, this is accompanied by an upward shift of a new VBM. After a critical percentage of strain, a direct band touching occurs, which is characterized by a TI phase. However, further increase of strain leads to a metal phase and because the topological nature does not change, the system may fall into the TM phase. Our model can not predict the VBM upward shift, hence, in spite of demonstrating the change of the topological phase, it can not distinguish between the TI and TM phases. Note that our approach can be simply extended to the case of FLP in which we expect to observe the topological phase transition at lower strain values, due to the fact that the inter-layers hoppings result in a smaller gap [34].

6.4.1 Electronic properties of PNRs under strain

In this subsection, we investigate the evolution of the band structure of PNRs in the presence of in-plane and perpendicular strain. As we showed, a topological phase transition occurs in the band spectrum of phosphorene. This should lead to the formation of topologically protected edge states in the band structure of the corresponding nanoribbons. For a system including the SOC, one can obtain the eigenvalues and eigenvectors using the following matrix

$$M_{i\alpha,j\beta}(\mathbf{k}) = \sum_{mn} \tau_{mi\alpha,nj\beta} e^{i\mathbf{k}\cdot\mathbf{R}_{mn}}, \qquad (6.17)$$

where $e^{i\mathbf{k}\cdot\mathbf{R}_{mn}}$ are the 1D Bloch wave functions. m, n denote super-cells; i, j are the basis sites in a super-cell and α, β denote the spin degree of freedom. $\mathbf{k}$ is the wave vector, and $\mathbf{R}_{mn}$ represents a Bravais lattice vector. $\tau_{mi\alpha,nj\beta}$ are the hopping integrals with usual SOC or intrinsic Rashba coupling that are conveniently defined between the basis site i with spin α of super cell m and the basis site j with spin β of unit cell n.

Note that, Eq. (6.17) is related to the energy spectrum of nanoribbons that are not edge passivated. The experimental realization of such nanoribbons with pristine edges in low dimensional materials as graphene is well known [224] and may be extended to the case of PNRs. However, the stability of such ribbons is important from the experimental point of view. Formation energy studies [191] showed that pristine PNRs are stable specially for ribbon widths which we have considered in this paper.

The emergence of quasi-flat bands which are detached completely from the bulk bands due to the special structure of phosphorene are well known [76, 211, 225]. As shown in Fig. 6.6 (a), there are topologically non-protected edge modes in the 1D bands of a typical
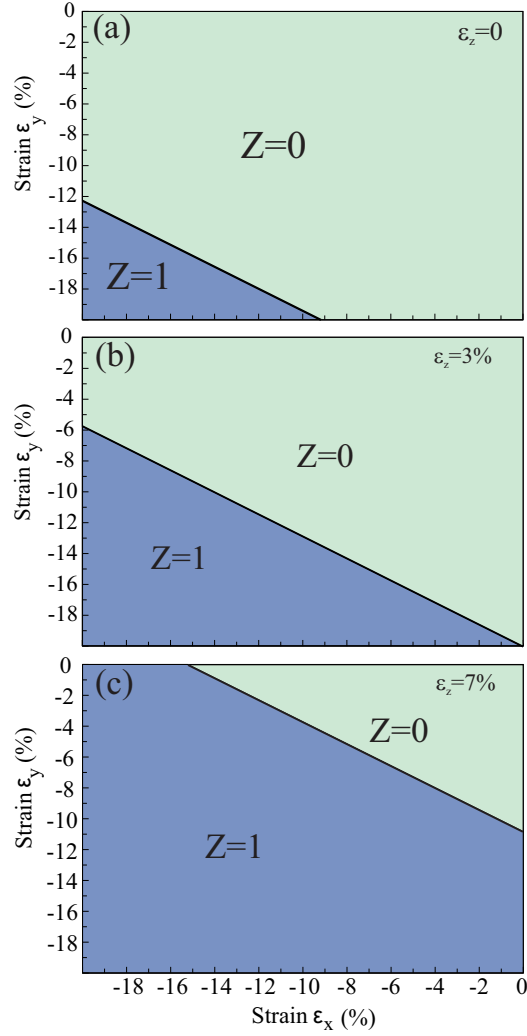
Figure 6.5: Phase diagrams of the $\mathbb{Z}_2$ invariant as function of ε_x and ε_y for different values of ε_z^c. The linear boundaries distinct the two topologically different phases according to the gap closing condition of $\eta_x\varepsilon_x + \eta_y\varepsilon_y = E_g^0 - \eta_z\varepsilon_z^c$.

zPNR (the results are for $N_z = 100$). These quasi-flat bands have been used to propose a FET driven by an in-plane electric field [76, 211]. However, since pristine bulk phosphorene is a trivial insulator, the existence of topologically non-protected edge modes in the corresponding nanoribbons which can be affected by environmental conditions such as disorder or impurities, may not be a good candidate for practical use. As an example, we consider the zigzag nanoribbon in the presence of perpendicular strain. The behaviour in

the presence of other types of strain is similar to this case. As can be seen in Figs. 6.6(b) and (c), by increasing strain the bulk gap of the nanoribbon gradually decreases and after a critical strain, where a band inversion occurs in the bulk spectrum, the corresponding edge states in the ribbon cross the gap which demonstrates a topological insulator phase. Owing to the dependence of the nanoribbon gap on the ribbon width, the critical strain for driving it to a topological insulator phase depends on the width as well. If we consider ribbons with very large widths, the critical value approaches the critical strain value of bulk 11.8% that we have calculated in previous section.

The anisotropic structure of phosphorene results in a large bulk gap for zigzag nanoribbons with experimentally accessible widths. This makes strained zPNRs ideal systems for observing topological states even at room temperature. As shown in Fig. 6.6(c) for a zigzag nanoribbon of width ~ 23 nm this gap is about 200 meV which is much larger than room temperature thermal energy. We have calculated numerically these bulk gaps for relatively large ribbons up to a width of 100 nm and found that the mentioned gaps are at least three orders of magnitude larger than the thermal energy at room temperature.It is worth mentioning that, such a typical ribbon width is wide enough to prevent from overlapping of edge states living on opposite sides of the ribbon. The corresponding probability amplitude of the topological edge modes of Fig. 6.6(c) which have amplitude on opposite edges are shown in Fig. 6.6(d) for $k = 0$. The amplitude of the wave functions drop very quickly along the width of the ribbon demonstrating that the nanoribbon width is wide enough to prevent quantum tunneling. Such excellent properties can pave the way for utilizing it in device applications.

6.5   Conclusions

In summary, we derived a spin-orbit model Hamiltonian based on the structural and electronic properties of phosphorene that captures the main physical properties of spin-orbit related subjects. Then we showed in the frame of this TB model that gap engineering of phosphorene by axial strains can lead to a topological phase transition in the electronic properties of phosphorene. In spite of the relatively small gap induced by SOC in bulk MLP, we predict that due to the special puckered structure of phosphorene, zigzag nanoribbons in the regime of TI have topologically protected edge states with rather large bulk band gaps of about 200 meV for a typical ribbon of width ~ 23 nm. Such gaps are larger that the thermal energy at room temperature and are therefore sufficiently large for practical device engineering at room temperature.
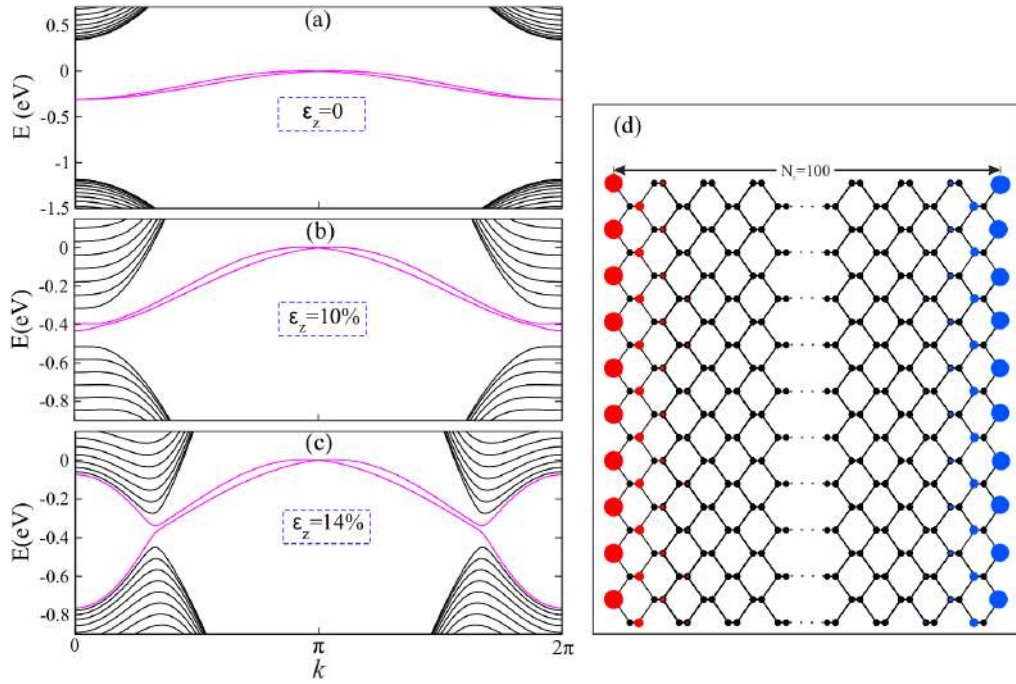
Figure 6.6: 1D energy bands for a typical PNR with $N_z = 100$ (~ 23 nm) in case: (a) without strain, (b) $\varepsilon_z = 10\%$, and (c) $\varepsilon_z = 14\%$. (d) The probability amplitude of the topological edge modes living on opposite edges for $k = 0$.

CHAPTER 7

Summary

In this thesis, the low energy electronic properties of MLP were theoretically investigated using the tight-binding (TB) approach. We specially focused on the topological properties of this system. To investigate these topological features, we have reviewed the basic theories of systems with and without TRS in chapters 2 and 3. In these chapters, we introduced efficient numerical methods for computing the relevant topological invariants which are very useful for characterization of the topology of complicated band structures. We numerically implemented these methods to the Haldane model, Kane-Mele model, and the AB-stacked bilayer graphene and compared the obtained topological phase diagrams with analytic results to demonstrate the validity of our algorithm. Then, we have presented our findings on some electronic and topological properties of phosphorene and PNRs in chapters 4, 5 and 6. The main obtained results are summarized as follows.

Chapter 4 was devoted to some basic electronic properties of monolayer phosphorene (MLP) and its nanoribbons. In this chapter, we first introduced a TB model for describing the low-energy spectrum of MLP. Then, the band structure and effective masses of the MLP near the gap were presented based on this TB model and it was shown that the dispersion is relativistic along the armchair direction and the Fermi velocities along this direction were calculated. Using this model, we showed that electrons and holes moving along the zigzag direction are more than six times heavier than those moving along the armchair direction. We presented a simple explanation for the reason why the special combination of the dominant hopping parameters creates a nearly relativistic dispersion along the armchair direction. Our results were in good agreement with first principle cal-

culations demonstrated the validation of this TB model for theoretical prediction of many electronic properties of MLP.

Thereafter, the TB model was applied to zigzag and armchair PNRs to analyze their band structure, the state characterization, and quantum conductance. We showed that in zPNRs, the ratio of the two dominant hopping parameters indicates the possibility of a relativistic dispersion relation and the existence of a pair of separate quasi-flat bands at the Fermi level. Moreover, the corresponding states are edge localized if their bands are well separated from the valence and conduction bands. We also investigated the scaling laws of the band gaps versus ribbon widths for the armchair and zigzag PNRs. We found that in contrast to GNRs, boron nitride nanoribbons and α-graphdiyne nanoribbons the band gap of PNRs decreases monotonically as the ribbon width increases. We numerically showed that the bang gap is larger in zPNRs for the same ribbon width, indicating that the energy contribution from quantum confinement is higher in zPNRs, thus resulting in a stronger quantum confinement effect in zPNRs. We argued that a DFT study suggested a scaling behavior of $\sim 1/w^2$ for aPNRs whereas a $\sim 1/w$ for zPNRs. But, we demonstrated that the scaling law for the zPNRs is not $1/w$. We argued that one should not expect a $1/w$ scaling law for zPNRs with ribbon widths larger than 3.5 nm.

Next, we analyzed the relationship between the electronic properties of armchair and zigzag PNRs and the external electric field along the ribbon width. We found that in aPNRs, the transverse electric field along the ribbon width enhances the band gap closure by shifting the energy of the valence and conduction band edge states. For zPNRs, a gap occurs at the middle of the relatively degenerate quasi-flat bands; thus, these ribbons are a promising candidate for future FETs.

In chapter 5, the basic aspects of low energy electrons and holes in MLP exposed to a perpendicular magnetic field were studied. We argued that inspired by the the anisotropy of its band structure one might expect to observe a behavior as $B^{2/3}$ in the LLs field dependence. The primary goal of the chapter was to address the controversial field dependence of LLs in MLP. We argued that the energy bands curvature is a predominant factor for determining the field dependence of LLs. We showed that the main aspects of the low energy spectrum of MLP are well described by only two dominant energy hopping integrals t_1 and t_2. We simplified our four-band TB model to a continuum low energy two-band Hamiltonian with zero diagonal elements. Then, using this simplification which preserves the physics of the system in the presence of magnetic field, we demonstrated that the LLs dependence on magnetic field is indeed as for conventional 2D semiconductor electron gases. We showed that the results are valid up to very high field.

Then, we discussed the conditions for which such a dependence can be evolved into another field dependence. As an example, we considered equi-biaxial compressive strain in the plane of MLP. We mentioned that the bond lengths and bond angles of phosphorene

both change under axial strains. Therefore, the hopping parameters will change. However, our calculations showed that although the modification of the hopping parameters due to changes in angles are almost noticeable, the modification of the hopping parameters due to them is much smaller than the effect of changes of the bond lengths. Therefore, we considered only changes of the bond lengths in the hopping modulation and used the Harisson rule $t_i \propto 1/r_i^2$ to modify the hopping parameter. We discussed that this modifies the low energy bands so that the valance and conduction bands approach each other. Using the numerical values of the structural parameters of MLP, we showed that the value of the band gap depends linearly on compressive equi-biaxial strain, in which is consistent with DFT calculations. We also demonstrated that this results to continuously evolution of LLs from a $(n + 1/2)B$ dependence to a $[(n + 1/2)B]^{2/3}$ dependence.

In chapter 6, we proposed a model Hamiltonian for the SOC for MLP that can be generalized to FLP. We showed that a model which includes the n-n neighbors in the upper or lower chains in the phosphorene structure is sufficient for capturing the main physics. We again studied the bulk band of phosphorene in the presence of axial strains using our TB approach and demonstrated that a band inversion occurs in the energy spectrum of phosphorene in the range where the structure is still stable under strain. We argued that pristine phosphorene as a trivial insulator when the intrinsic SOC effect is included preserves the TRS and can exhibit a QSH phase when its electronic properties is influenced by external factors e.g. electric field or strain. Using our algorithm for lattice computation of the $\mathbb{Z}_2$ invariant, we demonstrated numerically a topological phase transition in strained phosphorene and calculated the phase diagrams accordingly. We showed that for in-plane compressive global stain, there is a linear border between two distinct topological phases that corresponds to the regimes before and after the gap closing condition. We also found that the relatively large bulk band gap of MLP necessitates a rather large value of strain in order to observe band inversion. However, our approach can be simply extended to the case of FLP in which we expect to observe the topological phase transition at lower strain values due to the fact that the inter-layers hoppings result in a smaller gap.

Finally, we showed numerically that although the topological bulk band gaps induced by SOC is about 5 meV, but the highly anisotropic nature of this material causes the corresponding bulk gaps in large widths zPNRs be at least three orders of magnitude larger than room temperature thermal energy (~ 26 meV) and makes PNRs excellent candidates for future applications.

CHAPTER 8

Samenvatting

In deze doctoraatsthesis werden de lage energie elektronische eigenschappen van mono-laag fosforeen (MLP) theoretisch onderzocht gebruikend van de tight-binding (TB) be-nadering. Speciale aandacht ging naar de topologische eigenschappen van dit systeem. Om deze topologische kenmerken te onderzoeken, hebben we eerst de basistheorie van systemen met en zonder TRS gegeven in de hoofdstukken 2 en 3.

In deze twee hoofdstukken werden de numerieke methoden geïntroduceerd om de topolo-gische invariantie, die zeer geschikt is voor het beschrijven van complexe bandstructuren, te berekenen. We hebben deze numerieke methoden in de modellen van Haldane, Kane-Mele, en AB-gestapelde bilaag grafeen gebruikt en de resultaten vergeleken met de topolo-gische fasediagrammen die verkregen zijn vanuit analytische berekeningen en dus hebben we aangetoond dat ons algoritme geldig is.

Het vierde hoofdstuk is gewijd aan een aantal elektroneigenschappen van monolaag fos-foreen en zijn nanoribbons. In dit hoofdstuk werd eerst een TB-model geïntroduceerd om het energiespectrum van monolaag fosforeen te beschrijven. Met behulp van dit model hebben we aangetoond dat de elektronen en gaten die in de zigzag richting bewegen, meer dan zes keer zwaarder zijn dan degenen die in de armchair richting bewegen.

Daarna hebben we een eenvoudige verklaring gegeven voor de reden waarom de speciale combinatie van de dominante hopping parameters, aanleiding geeft tot een relativistische energie spectrum in de armchair richting. De verkregen resultaten zijn in goede overeen-stemming met de first-principles berekeningen. Aldus is dit TB-model geldig voor de theoretische voorspelling van de meeste elektroneigenschappen van monolaag fosforeen.

Vervolgens hebben we het TB-model toegepast voor zigzag en armchair fosforeen nanorib-bons, en analyseerde we hun bandstructuur, hun toestand, en hun kwantumgeleidbaarheid. Andere aspecten die we bestudeerd hebben, zijn o.a. de schaling van energiekloven met de breedte. DFT-onderzoek suggereerde een schaalgedrag van $\sim 1/w^2$ voor aPNRs en $\sim 1/w$ voor zPNRs. Maar we hebben aangetoond dat de schaling voor zPNRs niet overeenkomt met $1/w$. Voor nanoribbons met een breedte groter dan 3.5 nm, is het niet mogelijk om een $1/w$ schaling van de energiekloof te vinden. In verband met zPNRs, hebben we aange-toond dat een energiekloof in het midden van de relatief vlakke banden gecreëerd wordt, en daarom kunnen zo'ne nanoribbons, mogelijke kandidaten zijn voor toekomstige veldef-fecttransistoren. In het vijfde hoofdstuk werden de fundamentele aspecten van elektronen en gaten in fosforeen in een verticaal magnetisch veld bestudeerd. We argumenteerde dat op basis van de relatief hoge anisotropie in de bandstructuur van dit systeem, de Landau-niveaus een gedrag in de vorm van $B^{2/3}$ verwacht wordt. Dus het hoofddoel van dit hoofd-stuk was om de afhankelijkheid van het Landau-niveau op het magnetisch veld te analy-seren, die nog steeds ter discussie staat. We hebben het TB-model met vier banden gere-duceerd tot een Hamiltoniaans model met twee continue banden. Daarna hebben we met deze vereenvoudiging bewezen dat de afhankelijkheid van het Landau-niveau op het mag-netische veld, hetzelfde is als van elektronengassen in tweedimensionale halfgeleiders. We hebben aangetoond dat dit resultaat geldig is tot zeer hoge magnetische velden. Daarna hebben we de omstandigheden onderzocht waarin deze afhankelijkheid kan omgezet wor-den in een andere afhankelijkheid.

In het zesde hoofdstuk hebben we een Hamiltoniaan model voor de spinbaan-interactie in monolaag fosforeen, voorgesteld. We hebben met behulp van het TB-model, de ban-denstructuur van fosforeen in aanwezigheid van axiale strain bestudeerd en er wordt be-wezen dat een soort inversie van de banden optreedt in het energiespectrum. Met behulp van ons algoritme voor het berekenen van de $\mathbb{Z}_2$ invariant, hebben we een topologische fase-overgang van fosforeen onder strain gevonden en overeenkomstige fasediagram werd berekend. We hebben ook aangetoond, hoewel de geïnduceerde energiekloof door de spin-baaninteractie ongeveer 5 meV is, dat de grote anisotropie van dit materiaal resulteert in een groter energiekloof in zigzag-nanoribbons, en dit minstens drie keer groter is dan de thermische energie van kamertemperatuur. Aldus zijn nanoribbons van fosforeen een zeer goede kandidaat voor toekomstige toepassingen.

Bibliography

[1] K. S. Novoselov, A. K. Geim, S. V. Morozov, D. Jiang, Y. Zhang, S. V. Dubonos, I. V. Grigorieva, and A. A. Firsov, "Electric field effect in atomically thin carbon films," *Science*, vol. 306, no. 5696, pp. 666–669, 2004.

[2] Y. Zhu, S. Murali, W. Cai, X. Li, J. W. Suk, J. R. Potts, and R. S. Ruoff, "Graphene and graphene oxide: synthesis, properties, and applications," *Advanced Materials*, vol. 22, no. 35, pp. 3906–3924, 2010.

[3] A. C. Neto, F. Guinea, N. M. Peres, K. S. Novoselov, and A. K. Geim, "The electronic properties of graphene," *Reviews of Modern Physics*, vol. 81, no. 1, p. 109, 2009.

[4] M. Katsnelson, *Graphene: carbon in two dimensions*. Cambridge University Press, 2012.

[5] M. J. Allen, V. C. Tung, and R. B. Kaner, "Honeycomb carbon: a review of graphene," *Chemical Reviews*, vol. 110, no. 1, pp. 132–145, 2009.

[6] Q. H. Wang, K. Kalantar-Zadeh, A. Kis, J. N. Coleman, and M. S. Strano, "Electronics and optoelectronics of two-dimensional transition metal dichalcogenides," *Nature Nanotechnology*, vol. 7, no. 11, pp. 699–712, 2012.

[7] S. Z. Butler, S. M. Hollen, L. Cao, Y. Cui, J. A. Gupta, H. R. Gutiérrez, T. F. Heinz, S. S. Hong, J. Huang, A. F. Ismach, *et al.*, "Progress, challenges, and opportunities in two-dimensional materials beyond graphene," *ACS Nano*, vol. 7, no. 4, pp. 2898–2926, 2013.

[8] F. Xia, H. Wang, and Y. Jia, "Rediscovering black phosphorus as an anisotropic layered material for optoelectronics and electronics," *Nature Communications*, vol. 5, p. 4458, 2014.

[9] A. Carvalho, M. Wang, X. Zhu, A. S. Rodin, H. Su, and A. H. C. Neto, "Phosphorene: from theory to applications," *Nature Reviews Materials*, vol. 1, p. 16061, 2016.

[10] M. Pumera and A. H. Loo, "Layered transition-metal dichalcogenides (MoS_2 and WS_2) for sensing and biosensing," *Trends in Analytical Chemistry*, vol. 61, pp. 49–53, 2014.

[11] S. Manzeli, D. Ovchinnikov, D. Pasquier, O. V. Yazyev, and A. Kis, "2D transition metal dichalcogenides," *Nature Reviews Materials*, vol. 2, no. 8, p. 17033, 2017.

[12] A. Kuc, N. Zibouche, and T. Heine, "Influence of quantum confinement on the electronic structure of the transition metal sulfide TS_2," *Physical Review B*, vol. 83, no. 24, p. 245213, 2011.

[13] B. Radisavljevic, A. Radenovic, J. Brivio, i. V. Giacometti, and A. Kis, "Single-layer MoS_2 transistors," *Nature Nanotechnology*, vol. 6, no. 3, pp. 147–150, 2011.

[14] X. Ling, H. Wang, S. Huang, F. Xia, and M. S. Dresselhaus, "The renaissance of black phosphorus," *Proceedings of the National Academy of Sciences*, vol. 112, no. 15, pp. 4523–4530, 2015.

[15] L. Cartz, S. Srinivasa, R. Riedner, J. Jorgensen, and T. Worlton, "Effect of pressure on bonding in black phosphorus," *The Journal of Chemical Physics*, vol. 71, no. 4, pp. 1718–1721, 1979.

[16] P. Avouris, T. F. Heinz, and T. Low, *2D Materials*. Cambridge University Press, 2017.

[17] A. Favron, E. Gaufrès, F. Fossard, N. Y. Tang, P. L. Lévesque, A. Loiseau, R. Leonelli, S. Francoeur, R. Martel, *et al.*, "Photooxidation and quantum confinement effects in exfoliated black phosphorus," *Nature Materials*, vol. 14, no. 8, p. 826, 2015.

[18] R. Gusmao, Z. Sofer, and M. Pumera, "Black phosphorus rediscovered: from bulk material to monolayers," *Angewandte Chemie International Edition*, vol. 56, no. 28, pp. 8052–8072, 2017.

[19] S. Lange, P. Schmidt, and T. Nilges, "Au_3SnP_7 @ black phosphorus: an easy access to black phosphorus," *Inorganic Chemistry*, vol. 46, no. 10, pp. 4028–4035, 2007.

[20] H. Liu, A. T. Neal, Z. Zhu, Z. Luo, X. Xu, D. Tománek, and P. D. Ye, "Phosphorene: an unexplored 2D semiconductor with a high hole mobility," *ACS Nano*, vol. 8, no. 4, pp. 4033–4041, 2014.

[21] J. R. Brent, N. Savjani, E. A. Lewis, S. J. Haigh, D. J. Lewis, and P. O'Brien, "Production of few-layer phosphorene by liquid exfoliation of black phosphorus," *Chemical Communications*, vol. 50, no. 87, pp. 13338–13341, 2014.

[22] Z. Guo, H. Zhang, S. Lu, Z. Wang, S. Tang, J. Shao, Z. Sun, H. Xie, H. Wang, X.-F. Yu, *et al.*, "From black phosphorus to phosphorene: basic solvent exfoliation, evolution of raman scattering, and applications to ultrafast photonics," *Advanced Functional Materials*, vol. 25, no. 45, pp. 6996–7002, 2015.

[23] R. A. Doganov, S. P. Koenig, Y. Yeo, K. Watanabe, T. Taniguchi, and B. Özyilmaz, "Transport properties of ultrathin black phosphorus on hexagonal boron nitride," *Applied Physics Letters*, vol. 106, no. 8, p. 083505, 2015.

[24] J.-S. Kim, Y. Liu, W. Zhu, S. Kim, D. Wu, L. Tao, A. Dodabalapur, K. Lai, and D. Akinwande, "Toward air-stable multilayer phosphorene thin-films and transistors," *Scientific Reports*, vol. 5, p. 8989, 2015.

[25] L. Liang, J. Wang, W. Lin, B. G. Sumpter, V. Meunier, and M. Pan, "Electronic bandgap and edge reconstruction in phosphorene materials," *Nano Letters*, vol. 14, no. 11, pp. 6400–6406, 2014.

[26] R. W. Keyes, "The electrical properties of black phosphorus," *Physical Review*, vol. 92, no. 3, p. 580, 1953.

[27] D. Warschauer, "Electrical and optical properties of crystalline black phosphorus," *Journal of Applied Physics*, vol. 34, no. 7, pp. 1853–1860, 1963.

[28] Y. Maruyama, S. Suzuki, K. Kobayashi, and S. Tanuma, "Synthesis and some properties of black phosphorus single crystals," *Physica B+C*, vol. 105, no. 1-3, pp. 99–102, 1981.

[29] A. N. Rudenko and M. I. Katsnelson, "Quasiparticle band structure and tight-binding model for single-and bilayer black phosphorus," *Physical Review B*, vol. 89, no. 20, p. 201408, 2014.

[30] A. Rudenko, S. Yuan, and M. Katsnelson, "Toward a realistic description of multilayer black phosphorus: From gw approximation to large-scale tight-binding simulations," *Physical Review B*, vol. 92, no. 8, p. 085419, 2015.

[31] Ø. Prytz and E. Flage-Larsen, "The influence of exact exchange corrections in van der waals layered narrow bandgap black phosphorus," *Journal of Physics: Condensed Matter*, vol. 22, no. 1, p. 015502, 2009.

[32] J. Qiao, X. Kong, Z.-X. Hu, F. Yang, and W. Ji, "High-mobility transport anisotropy and linear dichroism in few-layer black phosphorus," *Nature Communications*, vol. 5, p. 4475, 2014.

[33] V. Tran, R. Soklaski, Y. Liang, and L. Yang, "Layer-controlled band gap and anisotropic excitons in few-layer black phosphorus," *Physical Review B*, vol. 89, no. 23, p. 235319, 2014.

[34] Y. Cai, G. Zhang, and Y.-W. Zhang, "Layer-dependent band alignment and work function of few-layer phosphorene," *Scientific Reports*, vol. 4, p. 6677, 2014.

[35] V. Wang, Y. Kawazoe, and W. Geng, "Native point defects in few-layer phosphorene," *Physical Review B*, vol. 91, no. 4, p. 045433, 2015.

[36] V. Tran and L. Yang, "Scaling laws for the band gap and optical response of phosphorene nanoribbons," *Physical Review B*, vol. 89, no. 24, p. 245407, 2014.

[37] Z.-X. Hu, X. Kong, J. Qiao, B. Normand, and W. Ji, "Interlayer electronic hybridization leads to exceptional thickness-dependent vibrational properties in few-layer black phosphorus," *Nanoscale*, vol. 8, no. 5, pp. 2740–2750, 2016.

[38] P. Li and I. Appelbaum, "Electrons and holes in phosphorene," *Physical Review B*, vol. 90, no. 11, p. 115439, 2014.

[39] K. S. Thygesen, "Calculating excitons, plasmons, and quasiparticles in 2D materials and van der waals heterostructures," *2D Materials*, vol. 4, no. 2, p. 022004, 2017.

[40] X. Wang, A. M. Jones, K. L. Seyler, V. Tran, Y. Jia, H. Zhao, H. Wang, L. Yang, X. Xu, and F. Xia, "Highly anisotropic and robust excitons in monolayer black phosphorus," *Nature Nanotechnology*, vol. 10, no. 6, p. 517, 2015.

[41] R. Roldán, A. Castellanos-Gomez, E. Cappelluti, and F. Guinea, "Strain engineering in semiconducting two-dimensional crystals," *Journal of Physics: Condensed Matter*, vol. 27, no. 31, p. 313201, 2015.

[42] Q. Wei and X. Peng, "Superior mechanical flexibility of phosphorene and few-layer black phosphorus," *Applied Physics Letters*, vol. 104, no. 25, p. 251915, 2014.

[43] J.-W. Jiang and H. S. Park, "Negative poisson's ratio in single-layer black phosphorus," *Nature Communications*, vol. 5, p. 4727, 2014.

[44] A. Rodin, A. Carvalho, and A. C. Neto, "Strain-induced gap modification in black phosphorus," *Physical Review Letters*, vol. 112, no. 17, p. 176801, 2014.

[45] C. Wang, Q. Xia, Y. Nie, and G. Guo, "Strain-induced gap transition and anisotropic Dirac-like cones in monolayer and bilayer phosphorene," *Applied Physics Letters*, vol. 117, no. 12, p. 124302, 2015.

[46] T. Zhang, J.-H. Lin, Y.-M. Yu, X.-R. Chen, and W.-M. Liu, "Stacked bilayer phosphorene: strain-induced quantum spin Hall state and optical measurement," *Scientific Reports*, vol. 5, p. 13927, 2015.

[47] J.-W. Jiang and H. S. Park, "Analytic study of strain engineering of the electronic bandgap in single-layer black phosphorus," *Physical Review B*, vol. 91, no. 23, p. 235118, 2015.

[48] Y. Mohammadi and B. A. Nia, "Strain engineering the charged-impurity-limited carrier mobility in phosphorene," *Superlattices and Microstructures*, vol. 89, pp. 204–215, 2016.

[49] H. Duan, M. Yang, and R. Wang, "Electronic structure and optic absorption of phosphorene under strain," *Physica E*, vol. 81, pp. 177–181, 2016.

[50] X. Peng, Q. Wei, and A. Copple, "Strain-engineered direct-indirect band gap transition and its mechanism in two-dimensional phosphorene," *Physical Review B*, vol. 90, no. 8, p. 085402, 2014.

[51] L. D. Landau, "On the theory of phase transitions," *Ukr. J. Phys.*, vol. 11, pp. 19–32, 1937.

[52] K. v. Klitzing, G. Dorda, and M. Pepper, "New method for high-accuracy determination of the fine-structure constant based on quantized Hall resistance," *Physical Review Letters*, vol. 45, no. 6, p. 494, 1980.

[53] D. C. Tsui, H. L. Störmer, and A. C. Gossard, "Two-dimensional magnetotransport in the extreme quantum limit," *Physical Review Letters*, vol. 48, no. 22, p. 1559, 1982.

[54] D. Thouless, M. Kohmoto, M. Nightingale, and M. Den Nijs, "Quantized Hall conductance in a two-dimensional periodic potential," *Physical Review Letters*, vol. 49, no. 6, p. 405, 1982.

[55] R. B. Laughlin, "Anomalous quantum Hall effect: an incompressible quantum fluid with fractionally charged excitations," *Physical Review Letters*, vol. 50, no. 18, p. 1395, 1983.

[56] Y. Xu, I. Miotkowski, C. Liu, J. Tian, H. Nam, N. Alidoust, J. Hu, C.-K. Shih, M. Z. Hasan, and Y. P. Chen, "Observation of topological surface state quantum Hall effect in an intrinsic three-dimensional topological insulator," *Nature Physics*, vol. 10, no. 12, p. 956, 2014.

[57] C. L. Kane and E. J. Mele, "Quantum spin Hall effect in graphene," *Physical Review Letters*, vol. 95, no. 22, p. 226801, 2005.

[58] B. A. Bernevig and S.-C. Zhang, "Quantum spin Hall effect," *Physical Review Letters*, vol. 96, no. 10, p. 106802, 2006.

[59] L. Fu, C. L. Kane, and E. J. Mele, "Topological insulators in three dimensions," *Physical Review Letters*, vol. 98, no. 10, p. 106803, 2007.

[60] L. Fu, "Topological crystalline insulators," *Physical Review Letters*, vol. 106, no. 10, p. 106802, 2011.

[61] F. Schindler, A. M. Cook, M. G. Vergniory, Z. Wang, S. S. Parkin, B. A. Bernevig, and T. Neupert, "Higher-order topological insulators," *Science Advances*, vol. 4, no. 6, p. eaat0346, 2018.

[62] S. Ornes, "Core concept: Topological insulators promise computing advances, insights into matter itself," *Proceedings of the National Academy of Sciences*, vol. 113, no. 37, pp. 10223–10224, 2016.

[63] J. Lado and J. Fernández-Rossier, "Landau levels in 2D materials using Wannier hamiltonians obtained by first principles," *2D Materials*, vol. 3, no. 3, p. 035023, 2016.

[64] L. Li, G. J. Ye, V. Tran, R. Fei, G. Chen, H. Wang, J. Wang, K. Watanabe, T. Taniguchi, L. Yang, *et al.*, "Quantum oscillations in a two-dimensional electron gas in black phosphorus thin films," *Nature Nanotechnology*, vol. 10, no. 7, p. 608.

[65] L. Li, F. Yang, G. J. Ye, Z. Zhang, Z. Zhu, W. Lou, X. Zhou, L. Li, K. Watanabe, T. Taniguchi, *et al.*, "Quantum Hall effect in black phosphorus two-dimensional electron system," *Nature Nanotechnology*, vol. 11, no. 7, p. 593, 2016.

[66] G. Long, D. Maryenko, J. Shen, S. Xu, J. Hou, Z. Wu, W. K. Wong, T. Han, J. Lin, Y. Cai, *et al.*, "Achieving ultrahigh carrier mobility in two-dimensional hole gas of black phosphorus," *Nano Letters*, vol. 16, no. 12, pp. 7768–7773, 2016.

[67] S. Tran, J. Yang, N. Gillgren, T. Espiritu, Y. Shi, K. Watanabe, T. Taniguchi, S. Moon, H. Baek, D. Smirnov, *et al.*, "Surface transport and quantum Hall effect in ambipolar black phosphorus double quantum wells," *Science advances*, vol. 3, no. 6, p. e1603179, 2017.

[68] J. Yang, S. Tran, J. Wu, S. Che, P. Stepanov, T. Taniguchi, K. Watanabe, H. Baek, D. Smirnov, R. Chen, *et al.*, "Integer and fractional quantum Hall effect in ultra-high quality few-layer black phosphorus transistors," *Nano Letters*, vol. 18, no. 1, pp. 229–234, 2017.

[69] X. Zhou, R. Zhang, J. Sun, Y. Zou, D. Zhang, W. Lou, F. Cheng, G. Zhou, F. Zhai, and K. Chang, "Landau levels and magneto-transport property of monolayer phosphorene," *Scientific Reports*, vol. 5, p. 12295, 2015.

[70] J. Pereira Jr and M. Katsnelson, "Landau levels of single-layer and bilayer phosphorene," *Physical Review B*, vol. 92, no. 7, p. 075437, 2015.

[71] S. Yuan, E. van Veen, M. I. Katsnelson, and R. Roldán, "Quantum Hall effect and semiconductor-to-semimetal transition in biased black phosphorus," *Physical Review B*, vol. 93, no. 24, p. 245433, 2016.

[72] M. Ezawa, "Highly anisotropic physics in phosphorene," in *Journal of Physics: Conference Series*, vol. 603, p. 012006, IOP Publishing, 2015.

[73] Y. Jiang, R. Roldán, F. Guinea, and T. Low, "Magnetoelectronic properties of multilayer black phosphorus," *Physical Review B*, vol. 92, no. 8, p. 085408, 2015.

[74] P. Dietl, F. Piéchon, and G. Montambaux, "New magnetic field dependence of landau levels in a graphenelike structure," *Physical Review Letters*, vol. 100, no. 23, p. 236405, 2008.

[75] T. Low, A. Rodin, A. Carvalho, Y. Jiang, H. Wang, F. Xia, and A. C. Neto, "Tunable optical properties of multilayer black phosphorus thin films," *Physical Review B*, vol. 90, no. 7, p. 075434, 2014.

[76] M. Ezawa, "Topological origin of quasi-flat edge band in phosphorene," *New Journal of Physics*, vol. 16, no. 11, p. 115004, 2014.

[77] J. Kim, S. S. Baik, S. H. Ryu, Y. Sohn, S. Park, B.-G. Park, J. Denlinger, Y. Yi, H. J. Choi, and K. S. Kim, "Observation of tunable band gap and anisotropic Dirac semimetal state in black phosphorus," *Science*, vol. 349, no. 6249, pp. 723–726, 2015.

[78] S. S. Baik, K. S. Kim, Y. Yi, and H. J. Choi, "Emergence of two-dimensional massless Dirac fermions, chiral pseudospins, and Berry's phase in potassium doped few-layer black phosphorus," *Nano Letters*, vol. 15, no. 12, pp. 7788–7793, 2015.

[79] Q. Liu, X. Zhang, L. Abdalla, A. Fazzio, and A. Zunger, "Switching a normal insulator into a topological insulator via electric field with application to phosphorene," *Nano Letters*, vol. 15, no. 2, pp. 1222–1228, 2015.

[80] R. Fei, V. Tran, and L. Yang, "Topologically protected Dirac cones in compressed bulk black phosphorus," *Physical Review B*, vol. 91, no. 19, p. 195319, 2015.

[81] Z. J. Xiang, G. J. Ye, C. Shang, B. Lei, N. Z. Wang, K. S. Yang, D. Liu, F. B. Meng, X. G. Luo, L. J. Zou, Z. Sun, Y. Zhang, and X. H. Chen, "Pressure-induced electronic transition in black phosphorus," *Physical Review Letters*, vol. 115, no. 18, p. 186403, 2015.

[82] C. Dutreix, E. Stepanov, and M. Katsnelson, "Laser-induced topological transitions in phosphorene with inversion symmetry," *Physical Review B*, vol. 93, no. 24, p. 241404, 2016.

[83] J. Kim, S. S. Baik, S. W. Jung, Y. Sohn, S. H. Ryu, H. J. Choi, B.-J. Yang, and K. S. Kim, "Two-dimensional Dirac fermions protected by space-time inversion symmetry in black phosphorus," *Physical Review Letters*, vol. 119, no. 22, p. 226801, 2017.

[84] J. Ahn and B.-J. Yang, "Unconventional topological phase transition in two-dimensional systems with space-time inversion symmetry," *Physical Review Letters*, vol. 118, no. 15, p. 156401, 2017.

[85] H. Liu, J.-T. Sun, C. Cheng, F. Liu, and S. Meng, "Photoinduced nonequilibrium topological states in strained black phosphorus," *Physical Review Letters*, vol. 120, no. 23, p. 237403, 2018.

[86] W. A. Benalcazar, B. A. Bernevig, and T. L. Hughes, "Quantized electric multipole insulators," *Science*, vol. 357, no. 6346, pp. 61–66, 2017.

[87] Y. Peng, Y. Bao, and F. von Oppen, "Boundary green functions of topological insulators and superconductors," *Physical Review B*, vol. 95, no. 23, p. 235143, 2017.

[88] M. Ezawa, "Minimal models for Wannier-type higher-order topological insulators and phosphorene," *Physical Review B*, vol. 98, no. 4, p. 045125, 2018.

[89] K. Von Klitzing, "25 years of quantum Hall effect (QHE a personal view on the discovery, physics and applications of this quantum effect," in *The Quantum Hall Effect*, pp. 1–21, Springer, 2005.

[90] T. Fukui, Y. Hatsugai, and H. Suzuki, "Chern numbers in discretized brillouin zone: efficient method of computing (spin) Hall conductances," *Journal of the Physical Society of Japan*, vol. 74, no. 6, pp. 1674–1677, 2005.

[91] J. K. Jain, *Composite fermions*. Cambridge University Press, 2007.

[92] T. D. Stanescu, *Introduction to Topological Quantum Matter & Quantum Computation*. CRC Press, 2016.

[93] V. Lahtinen and J. Pachos, "A short introduction to topological quantum computation," *SciPost Physics*, vol. 3, no. 3, p. 021, 2017.

[94] A. Y. Kitaev, "Fault-tolerant quantum computation by anyons," *Annals of Physics*, vol. 303, no. 1, pp. 2–30, 2003.

[95] D. Reuter, C. Riedesel, P. Schafmeister, C. Meier, and A. Wieck, "Fabrication of high-quality two-dimensional electron gases by overgrowth of focused-ion-beam-doped al x ga 1- x as," *Applied Physics Letters*, vol. 82, no. 3, pp. 481–483, 2003.

[96] R. B. Laughlin, "Quantized Hall conductivity in two dimensions," *Physical Review B*, vol. 23, no. 10, p. 5632, 1981.

[97] M. E. Cage, K. Klitzing, A. Chang, F. Duncan, M. Haldane, R. B. Laughlin, A. Pruisken, and D. Thouless, *The quantum Hall effect*. Springer Science & Business Media, 2012.

[98] W. Kohn, "Effective mass theory in solids from a many-particle standpoint," *Physical Review*, vol. 105, no. 2, p. 509, 1957.

[99] E. Cockayne, G. M. Rutter, N. P. Guisinger, J. N. Crain, P. N. First, and J. A. Stroscio, "Grain boundary loops in graphene," *Physical Review B*, vol. 83, no. 19, p. 195425, 2011.

[100] Y. Zhang, Y.-W. Tan, H. L. Stormer, and P. Kim, "Experimental observation of the quantum Hall effect and Berry's phase in graphene," *Nature*, vol. 438, no. 7065, p. 201, 2005.

[101] J. McClure, "Diamagnetism of graphite," *Physical Review*, vol. 104, no. 3, p. 666, 1956.

[102] Z. F. Ezawa, *Quantum Hall effects: Recent theoretical and experimental developments*. World Scientific Publishing Co Inc, 2013.

[103] K. S. Novoselov, A. K. Geim, S. Morozov, D. Jiang, M. Katsnelson, I. Grigorieva, S. Dubonos, and A. A. Firsov, "Two-dimensional gas of massless Dirac fermions in graphene," *Nature*, vol. 438, no. 7065, p. 197, 2005.

[104] Y. Zheng and T. Ando, "Hall conductivity of a two-dimensional graphite system," *Physical Review B*, vol. 65, no. 24, p. 245420, 2002.

[105] V. Gusynin and S. Sharapov, "Unconventional integer quantum Hall effect in graphene," *Physical Review Letters*, vol. 95, no. 14, p. 146801, 2005.

[106] K. S. Novoselov, E. McCann, S. Morozov, V. I. Falko, M. Katsnelson, U. Zeitler, D. Jiang, F. Schedin, and A. Geim, "Unconventional quantum Hall effect and Berry's phase of 2π in bilayer graphene," *Nature physics*, vol. 2, no. 3, pp. 177–180, 2006.

[107] E. McCann and V. I. Falko, "Landau-level degeneracy and quantum Hall effect in a graphite bilayer," *Physical Review Letters*, vol. 96, no. 8, p. 086805, 2006.

[108] Y. Hatsugai, "Topological aspects of the quantum Hall effect," *Journal of Physics: Condensed Matter*, vol. 9, no. 12, p. 2507, 1997.

[109] M. V. Berry, "Quantal phase factors accompanying adiabatic changes," *Proceedings of the Royal Society of London. A. Mathematical and Physical Sciences*, vol. 392, p. 45, 1984.

[110] D. Xiao, M.-C. Chang, and Q. Niu, "Berry phase effects on electronic properties," *Reviews of Modern Physics*, vol. 82, no. 3, p. 1959, 2010.

[111] M. Kohmoto, "Topological invariant and the quantization of the Hall conductance," *Annals of Physics*, vol. 160, no. 2, pp. 343–354, 1985.

[112] A. Dauphin, M. Müller, and M. Martin-Delgado, "Efficient algorithm to compute the Berry conductivity," *New Journal of Physics*, vol. 16, no. 7, 2014.

[113] M. Lüscher, "Topology of lattice gauge fields," *Communications in Mathematical Physics*, vol. 85, no. 1, pp. 39–48, 1982.

[114] A. Phillips, "Characteristic numbers of U1-valued lattice gauge fields," *Annals of Physics*, vol. 161, no. 2, pp. 399–422, 1985.

[115] T. Fukui and Y. Hatsugai, "Quantum spin Hall effect in three dimensional materials: Lattice computation of $\mathbb{Z}_2$ topological invariants and its application to Bi and Sb," *Journal of the Physical Society of Japan*, vol. 76, no. 5, p. 053702, 2007.

[116] Y. Hatsugai, "Explicit gauge fixing for degenerate multiplets: A generic setup for topological orders," *Journal of the Physical Society of Japan*, vol. 73, no. 10, pp. 2604–2607, 2004.

[117] F. D. M. Haldane, "Model for a quantum Hall effect without landau levels: Condensed-matter realization of the "parity anomaly"," *Physical Review Letters*, vol. 61, no. 18, p. 2015, 1988.

[118] M. König, S. Wiedmann, C. Brüne, A. Roth, H. Buhmann, L. W. Molenkamp, X.-L. Qi, and S.-C. Zhang, "Quantum spin Hall insulator state in HgTe quantum wells," *Science*, vol. 318, no. 5851, pp. 766–770, 2007.

[119] H. Min, J. Hill, N. A. Sinitsyn, B. Sahu, L. Kleinman, and A. H. MacDonald, "Intrinsic and rashba spin-orbit interactions in graphene sheets," *Physical Review B*, vol. 74, no. 16, p. 165310, 2006.

[120] S. Roche and S. O. Valenzuela, *Topological insulators: Fundamentals and perspectives*. John Wiley & Sons, 2015.

[121] B. A. Bernevig, T. L. Hughes, and S.-C. Zhang, "Quantum spin Hall effect and topological phase transition in HgTe quantum wells," *Science*, vol. 314, no. 5806, pp. 1757–1761, 2006.

[122] M. König, H. Buhmann, L. W. Molenkamp, T. Hughes, C.-X. Liu, X.-L. Qi, and S.-C. Zhang, "The quantum spin Hall effect: theory and experiment," *Journal of the Physical Society of Japan*, vol. 77, no. 3, p. 031007, 2008.

[123] X.-L. Qi and S.-C. Zhang, "The quantum spin Hall effect and topological insulators," *Physics Today*, vol. 63(1), p. 33, 2010.

[124] J. E. Moore, "The birth of topological insulators," *Nature*, vol. 464, no. 7286, pp. 194–198, 2010.

[125] M. Z. Hasan and C. L. Kane, "Colloquium: topological insulators," *Reviews of Modern Physics*, vol. 82, no. 4, p. 3045, 2010.

[126] X.-L. Qi and S.-C. Zhang, "Topological insulators and superconductors," *Reviews of Modern Physics*, vol. 83, no. 4, p. 1057, 2011.

[127] C. Kane and J. Moore, "Topological insulators," *Physics World*, vol. 24, no. 02, p. 32, 2011.

[128] B. A. Bernevig and T. L. Hughes, *Topological insulators and topological superconductors*. Princeton University Press, 2013.

[129] S.-Q. Shen, *Topological insulators*, vol. 174. Springer, 2012.

[130] J. K. Asbóth, L. Oroszlány, and A. Pályi, *A short course on topological insulators: Band structure and edge states in one and two dimensions*, vol. 919. Springer, 2016.

[131] G. Tkachov, *Topological insulators: The physics of spin helicity in quantum transport*. CRC Press, 2015.

[132] A. Bansil, H. Lin, and T. Das, "Colloquium: Topological band theory," *Reviews of Modern Physics*, vol. 88, no. 2, p. 021004, 2016.

[133] Y. Fan and K. L. Wang, "Spintronics based on topological insulators," in *Spin*, vol. 6, p. 1640001, World Scientific, 2016.

[134] T. Yokoyama and S. Murakami, "Spintronics and spincaloritronics in topological insulators," *Physica E: Low-dimensional Systems and Nanostructures*, vol. 55, pp. 1–8, 2014.

[135] A. Yazdani, "Topological surface states: science and potential applications," in *Micro-and Nanotechnology Sensors, Systems, and Applications IV*, vol. 8373, p. 837307, International Society for Optics and Photonics, 2012.

[136] W. Tian, W. Yu, J. Shi, and Y. Wang, "The property, preparation and application of topological insulators: A review," *Materials*, vol. 10, no. 7, p. 814, 2017.

[137] L. Fu and C. L. Kane, "Topological insulators with inversion symmetry," *Physical Review B*, vol. 76, no. 4, p. 045302, 2007.

[138] L. Fu and C. L. Kane, "Time reversal polarization and a $\mathbb{Z}_2$ adiabatic spin pump," *Physical Review B*, vol. 74, no. 19, p. 195312, 2006.

[139] C. L. Kane and E. J. Mele, "$\mathbb{Z}_2$ topological order and the quantum spin Hall effect," *Physical Review Letters*, vol. 95, no. 14, p. 146802, 2005.

[140] T. Wolfram and Ş. Ellialtıoğlu, *Applications of group theory to atoms, molecules, and solids*. Cambridge University Press, 2014.

[141] W. Feng, J. Wen, J. Zhou, D. Xiao, and Y. Yao, "First-principles calculation of $\mathbb{Z}_2$ topological invariants within the fp-lapw formalism," *Computer Physics Communications*, vol. 183, no. 9, pp. 1849–1859, 2012.

[142] J. Gu and K. Sun, "Adiabatic continuity, wave-function overlap, and topological phase transitions," *Physical Review B*, vol. 94, no. 12, p. 125111, 2016.

[143] J.-C. Charlier, P. Eklund, J. Zhu, and A. Ferrari, "Electron and phonon properties of graphene: their relationship with carbon nanotubes," in *Carbon nanotubes*, pp. 673–709, Springer, 2007.

[144] C. Bena and G. Montambaux, "Remarks on the tight-binding model of graphene," *New Journal of Physics*, vol. 11, no. 9, p. 095003, 2009.

[145] G. Mikitik and Y. V. Sharlai, "Manifestation of Berry's phase in metal physics," *Physical Review Letters*, vol. 82, no. 10, p. 2147, 1999.

[146] R. Takahashi, *Topological States on Interfaces Protected by Symmetry*. Springer, 2015.

[147] S. Ryu and Y. Hatsugai, "Topological origin of zero-energy edge states in particle-hole symmetric systems," *Physical Review Letters*, vol. 89, no. 7, p. 077002, 2002.

[148] P. Delplace, D. Ullmo, and G. Montambaux, "Zak phase and the existence of edge states in graphene," *Physical Review B*, vol. 84, no. 19, p. 195452, 2011.

[149] G. van Miert, C. Ortix, and C. M. Smith, "Topological origin of edge states in two-dimensional inversion-symmetric insulators and semimetals," *2D Materials*, vol. 4, no. 1, p. 015023, 2016.

[150] K. Nakada, M. Fujita, G. Dresselhaus, and M. S. Dresselhaus, "Edge state in graphene ribbons: Nanometer size effect and edge shape dependence," *Physical Review B*, vol. 54, no. 24, p. 17954, 1996.

[151] B. I. Halperin, "Quantized Hall conductance, current-carrying edge states, and the existence of extended states in a two-dimensional disordered potential," *Physical Review B*, vol. 25, no. 4, p. 2185, 1982.

[152] J. E. Moore and L. Balents, "Topological invariants of time-reversal-invariant band structures," *Physical Review B*, vol. 75, no. 12, p. 121306, 2007.

[153] R. Roy, "Topological phases and the quantum spin Hall effect in three dimensions," *Physical Review B*, vol. 79, no. 19, p. 195322, 2009.

[154] K. W. Kim, *Electronic states in disordered topological insulators*. California Institute of Technology, 2014.

[155] J. Nayak, S.-C. Wu, N. Kumar, C. Shekhar, S. Singh, J. Fink, E. E. Rienks, G. H. Fecher, S. S. Parkin, B. Yan, *et al.*, "Multiple Dirac cones at the surface of the topological metal labi," *Nature Communications*, vol. 8, p. 13942, 2017.

[156] E. Prodan, "Manifestly gauge-independent formulations of the $\mathbb{Z}_2$ invariants," *Physical Review B*, vol. 83, no. 23, p. 235115, 2011.

[157] Y. Ando, "Topological insulator materials," *Journal of the Physical Society of Japan*, vol. 82, no. 10, p. 102001, 2013.

[158] R. Resta, "Electrical polarization and orbital magnetization: the modern theories," *Journal of Physics: Condensed Matter*, vol. 22, no. 12, p. 123201, 2010.

[159] A. A. Soluyanov, *Topological aspects of band theory*. PhD thesis, Rutgers University-Graduate School-New Brunswick, 2012.

[160] D. Sheng, Z. Weng, L. Sheng, and F. Haldane, "Quantum spin-Hall effect and topologically invariant Chern numbers," *Physical Review Letters*, vol. 97, no. 3, p. 036808, 2006.

[161] E. Prodan, "Robustness of the spin-Chern number," *Physical Review B*, vol. 80, no. 12, p. 125327, 2009.

[162] Y. Yang, Z. Xu, L. Sheng, B. Wang, D. Xing, and D. Sheng, "Time-reversal-symmetry-broken quantum spin Hall effect," *Physical Review Letters*, vol. 107, no. 6, p. 066602, 2011.

[163] A. A. Soluyanov and D. Vanderbilt, "Wannier representation of $\mathbb{Z}_2$ topological insulators," *Physical Review B*, vol. 83, no. 3, p. 035108, 2011.

[164] J. Zak, "Symmetry specification of bands in solids," *Physical Review Letters*, vol. 45, no. 12, p. 1025, 1980.

[165] J. Zak, "Band representations and symmetry types of bands in solids," *Physical Review B*, vol. 23, no. 6, p. 2824, 1981.

[166] J. Cano, B. Bradlyn, Z. Wang, L. Elcoro, M. Vergniory, C. Felser, M. Aroyo, and B. A. Bernevig, "Building blocks of topological quantum chemistry: Elementary band representations," *Physical Review B*, vol. 97, no. 3, p. 035139, 2018.

[167] B. Bradlyn, L. Elcoro, J. Cano, M. Vergniory, Z. Wang, C. Felser, M. Aroyo, and B. A. Bernevig, "Topological quantum chemistry," *Nature*, vol. 547, no. 7663, p. 298, 2017.

[168] M. Vergniory, L. Elcoro, Z. Wang, J. Cano, C. Felser, M. Aroyo, B. A. Bernevig, and B. Bradlyn, "Graph theory data for topological quantum chemistry," *Physical Review E*, vol. 96, no. 2, p. 023310, 2017.

[169] L. Elcoro, B. Bradlyn, Z. Wang, M. G. Vergniory, J. Cano, C. Felser, B. A. Bernevig, D. Orobengoa, G. Flor, and M. I. Aroyo, "Double crystallographic groups and their representations on the bilbao crystallographic server," *Journal of Applied Crystallography*, vol. 50, no. 5, pp. 1457–1477, 2017.

[170] B. Bradlyn, L. Elcoro, M. Vergniory, J. Cano, Z. Wang, C. Felser, M. Aroyo, and B. A. Bernevig, "Band connectivity for topological quantum chemistry: Band structures as a graph theory problem," *Physical Review B*, vol. 97, no. 3, p. 035138, 2018.

[171] Z. Qiao, W.-K. Tse, H. Jiang, Y. Yao, and Q. Niu, "Two-dimensional topological insulator state and topological phase transition in bilayer graphene," *Physical Review Letters*, vol. 107, no. 25, p. 256801, 2011.

[172] I. Knez, R.-R. Du, and G. Sullivan, "Evidence for helical edge modes in inverted inas/gasb quantum wells," *Physical Review Letters*, vol. 107, no. 13, p. 136603, 2011.

[173] W. Feng and Y. Yao, "Three-dimensional topological insulators: A review on host materials," *Science China Physics, Mechanics and Astronomy*, vol. 55, no. 12, pp. 2199–2212, 2012.

[174] A. Roth, C. Brüne, H. Buhmann, L. W. Molenkamp, J. Maciejko, X.-L. Qi, and S.-C. Zhang, "Nonlocal transport in the quantum spin Hall state," *Science*, vol. 325, no. 5938, pp. 294–297, 2009.

[175] Y. Chen, J.-H. Chu, J. Analytis, Z. Liu, K. Igarashi, H.-H. Kuo, X. Qi, S.-K. Mo, R. Moore, D. Lu, *et al.*, "Massive Dirac fermion on the surface of a magnetically doped topological insulator," *Science*, vol. 329, no. 5992, pp. 659–662, 2010.

[176] A. Damascelli, "Probing the electronic structure of complex systems by ARPES," *Physica Scripta*, vol. 2004, no. T109, p. 61, 2004.

[177] Z. Liu, B. Zhou, Y. Zhang, Z. Wang, H. Weng, D. Prabhakaran, S.-K. Mo, Z. Shen, Z. Fang, X. Dai, *et al.*, "Discovery of a three-dimensional topological Dirac semimetal, Na_3Bi," *Science*, vol. 343, no. 6173, pp. 864–867, 2014.

[178] B. Lv, H. Weng, B. Fu, X. Wang, H. Miao, J. Ma, P. Richard, X. Huang, L. Zhao, G. Chen, *et al.*, "Experimental discovery of Weyl semimetal TaAs," *Physical Review X*, vol. 5, no. 3, p. 031013, 2015.

[179] T. Zhang, P. Cheng, X. Chen, J.-F. Jia, X. Ma, K. He, L. Wang, H. Zhang, X. Dai, Z. Fang, *et al.*, "Experimental demonstration of topological surface states protected by time-reversal symmetry," *Physical Review Letters*, vol. 103, no. 26, p. 266803, 2009.

[180] P. Cheng, T. Zhang, K. He, X. Chen, X. Ma, and Q. Xue, "Scanning tunneling microscopy studies of topological insulators," *Physica E: Low-dimensional Systems and Nanostructures*, vol. 44, no. 5, pp. 912–916, 2012.

[181] A. K. Geim and K. S. Novoselov, "The rise of graphene," in *Nanoscience and Technology: A Collection of Reviews from Nature Journals*, pp. 11–19, World Scientific, 2010.

[182] A. Splendiani, L. Sun, Y. Zhang, T. Li, J. Kim, C.-Y. Chim, G. Galli, and F. Wang, "Emerging photoluminescence in monolayer MoS_2," *Nano Letters*, vol. 10, no. 4, pp. 1271–1275, 2010.

[183] K. F. Mak, C. Lee, J. Hone, J. Shan, and T. F. Heinz, "Atomically thin MoS_2: a new direct-gap semiconductor," *Physical Review Letters*, vol. 105, no. 13, p. 136805, 2010.

[184] D. Xiao, G.-B. Liu, W. Feng, X. Xu, and W. Yao, "Coupled spin and valley physics in monolayers of MoS_2 and other group-vi dichalcogenides," *Physical Review Letters*, vol. 108, no. 19, p. 196802, 2012.

[185] Y.-W. Son, M. L. Cohen, and S. G. Louie, "Half-metallic graphene nanoribbons," *Nature*, vol. 444, no. 7117, p. 347, 2006.

[186] L. Yang, M. L. Cohen, and S. G. Louie, "Excitonic effects in the optical spectra of graphene nanoribbons," *Nano Letters*, vol. 7, no. 10, pp. 3112–3115, 2007.

[187] X. Wang, Y. Ouyang, X. Li, H. Wang, J. Guo, and H. Dai, "Room-temperature all-semiconducting sub-10-nm graphene nanoribbon field-effect transistors," *Physical Review Letters*, vol. 100, no. 20, p. 206803, 2008.

[188] Q. Wu, L. Shen, M. Yang, Y. Cai, Z. Huang, Y. P. Feng, *et al.*, "Electronic and transport properties of phosphorene nanoribbons," *Physical Review B*, vol. 92, no. 3, p. 035436, 2015.

[189] J. Zhang, H. Liu, L. Cheng, J. Wei, J. Liang, D. Fan, J. Shi, X. Tang, and Q. Zhang, "Phosphorene nanoribbon as a promising candidate for thermoelectric applications," *Scientific Reports*, vol. 4, p. 6452, 2014.

[190] V. Sorkin and Y. Zhang, "The structure and elastic properties of phosphorene edges," *Nanotechnology*, vol. 26, no. 23, p. 235707, 2015.

[191] A. Carvalho, A. Rodin, and A. C. Neto, "Phosphorene nanoribbons," *EPL (Europhysics Letters)*, vol. 108, no. 4, p. 47005, 2014.

[192] X. Peng, A. Copple, and Q. Wei, "Edge effects on the electronic properties of phosphorene nanoribbons," *Journal of Applied Physics*, vol. 116, no. 14, p. 144301, 2014.

[193] H. Guo, N. Lu, J. Dai, X. Wu, and X. C. Zeng, "Phosphorene nanoribbons, phosphorus nanotubes, and van der waals multilayers," *The Journal of Physical Chemistry C*, vol. 118, no. 25, pp. 14051–14059, 2014.

[194] A. Castellanos-Gomez, L. Vicarelli, E. Prada, J. O. Island, K. Narasimha-Acharya, S. I. Blanter, D. J. Groenendijk, M. Buscema, G. A. Steele, J. Alvarez, *et al.*, "Isolation and characterization of few-layer black phosphorus," *2D Materials*, vol. 1, no. 2, p. 025001, 2014.

[195] Y.-W. Son, M. L. Cohen, and S. G. Louie, "Energy gaps in graphene nanoribbons," *Physical Review Letters*, vol. 97, no. 21, p. 216803, 2006.

[196] K. Dolui, C. D. Pemmaraju, and S. Sanvito, "Electric field effects on armchair MoS_2 nanoribbons," *ACS Nano*, vol. 6, no. 6, pp. 4823–4834, 2012.

[197] X. Zhao, C. Wei, L. Yang, and M. Chou, "Quantum confinement and electronic properties of silicon nanowires," *Physical Review Letters*, vol. 92, no. 23, p. 236805, 2004.

[198] L. Yang, C.-H. Park, Y.-W. Son, M. L. Cohen, and S. G. Louie, "Quasiparticle energies and band gaps in graphene nanoribbons," *Physical Review Letters*, vol. 99, no. 18, p. 186801, 2007.

[199] C.-H. Park and S. G. Louie, "Energy gaps and stark effect in boron nitride nanoribbons," *Nano Letters*, vol. 8, no. 8, pp. 2200–2203, 2008.

[200] Z. Zhang and W. Guo, "Energy-gap modulation of bn ribbons by transverse electric fields: First-principles calculations," *Physical Review B*, vol. 77, no. 7, p. 075403, 2008.

[201] X. Niu, D. Yang, M. Si, and D. Xue, "Energy gaps in α-graphdiyne nanoribbons," *Journal of Applied Physics*, vol. 115, no. 14, p. 143706, 2014.

[202] J. O'keeffe, C. Wei, and K. Cho, "Bandstructure modulation for carbon nanotubes in a uniform electric field," *Applied Physics Letters*, vol. 80, no. 4, pp. 676–678, 2002.

[203] Y. Zhang, T.-T. Tang, C. Girit, Z. Hao, M. C. Martin, A. Zettl, M. F. Crommie, Y. R. Shen, and F. Wang, "Direct observation of a widely tunable bandgap in bilayer graphene," *Nature*, vol. 459, no. 7248, p. 820, 2009.

[204] L.-D. Zhang, F. Yang, and Y. Yao, "Possible electric-field-induced superconducting states in doped silicene," *Scientific Reports*, vol. 5, p. 8203, 2015.

[205] S. Datta, *Electronic transport in mesoscopic systems*. Cambridge university press, 1997.

[206] S. Datta, *Quantum transport: atom to transistor*. Cambridge university press, 2005.

[207] K. S. Novoselov, Z. Jiang, Y. Zhang, S. Morozov, H. L. Stormer, U. Zeitler, J. Maan, G. Boebinger, P. Kim, and A. K. Geim, "Room-temperature quantum Hall effect in graphene," *Science*, vol. 315, no. 5817, pp. 1379–1379, 2007.

[208] Y. Takao, H. Asahina, and A. Morita, "Electronic structure of black phosphorus in tight binding approach," *Journal of the Physical Society of Japan*, vol. 50, no. 10, pp. 3362–3369, 1981.

[209] Z. Popović, J. M. Kurdestany, and S. Satpathy, "Electronic structure and anisotropic rashba spin-orbit coupling in monolayer black phosphorus," *Physical Review B*, vol. 92, no. 3, p. 035135, 2015.

[210] M. Kurpas, M. Gmitra, and J. Fabian, "Spin-orbit coupling and spin relaxation in phosphorene: Intrinsic versus extrinsic effects," *Physical Review B*, vol. 94, no. 15, p. 155423, 2016.

[211] E. T. Sisakht, M. H. Zare, and F. Fazileh, "Scaling laws of band gaps of phosphorene nanoribbons: A tight-binding calculation," *Physical Review B*, vol. 91, no. 8, p. 085409, 2015.

[212] G. Huang and Z. Xing, "Semiconductor to metal transition, dynamical stability and superconductivity of strained phosphorene," *arXiv preprint arXiv:1409.7284*, 2014.

[213] B. Sa, Y.-L. Li, J. Qi, R. Ahuja, and Z. Sun, "Strain engineering for phosphorene: the potential application as a photocatalyst," *The Journal of Physical Chemistry C*, vol. 118, no. 46, pp. 26560–26568, 2014.

[214] W. A. Harrison, *Elementary Electronic Structure: Revised*. World Scientific Publishing Company, 2004.

[215] Y. Ren, Z. Qiao, and Q. Niu, "Topological phases in two-dimensional materials: a review," *Reports on Progress in Physics*, vol. 79, no. 6, p. 066501, 2016.

[216] Y. Ma, Y. Dai, W. Wei, B. Huang, and M.-H. Whangbo, "Strain-induced quantum spin Hall effect in methyl-substituted germanane GeCH$_3$," *Scientific Reports*, vol. 4, p. 7297, 2014.

[217] M. Ezawa, "Valley-polarized metals and quantum anomalous Hall effect in silicene," *Physical Review Letters*, vol. 109, no. 5, p. 055502, 2012.

[218] S. P. Koenig, R. A. Doganov, H. Schmidt, A. Castro Neto, and B. Oezyilmaz, "Electric field effect in ultrathin black phosphorus," *Applied Physics Letters*, vol. 104, no. 10, p. 103106, 2014.

[219] L. Li, Y. Yu, G. J. Ye, Q. Ge, X. Ou, H. Wu, D. Feng, X. H. Chen, and Y. Zhang, "Black phosphorus field-effect transistors," *Nature Nanotechnology*, vol. 9, no. 5, p. 372, 2014.

[220] R. Fei, V. Tran, and L. Yang, "Topologically protected Dirac cones in compressed bulk black phosphorus," *Physical Review B*, vol. 91, no. 19, p. 195319, 2015.

[221] R. Fei and L. Yang, "Strain-engineering the anisotropic electrical conductance of few-layer black phosphorus," *Nano Letters*, vol. 14, no. 5, pp. 2884–2889, 2014.

[222] Y. Li, S. Yang, and J. Li, "Modulation of the electronic properties of ultrathin black phosphorus by strain and electrical field," *The Journal of Physical Chemistry C*, vol. 118, no. 41, pp. 23970–23976, 2014.

[223] C.-C. Liu, H. Jiang, and Y. Yao, "Low-energy effective hamiltonian involving spin-orbit coupling in silicene and two-dimensional germanium and tin," *Physical Review B*, vol. 84, no. 19, p. 195430, 2011.

[224] X. Zhang, J. Xin, and F. Ding, "The edges of graphene," *Nanoscale*, vol. 5, no. 7, pp. 2556–2569, 2013.

[225] M. M. Grujić, M. Ezawa, M. Ž. Tadić, and F. M. Peeters, "Tunable skewed edges in puckered structures," *Physical Review B*, vol. 93, no. 24, p. 245413, 2016.

Curriculum vitae

Esmaeil Taghizadeh Sisakht

PhD in condensed matter physics

Name and surname:
Esmaeil Taghizadeh Sisakht
Gender:
Male
Email:
etsisakht28@gmail.com
Citizenship:
Iran
Cell Phone:
+98(917) 8418910
Phone:
+98(31) 33916572

Address:
No.202, Department of Physics, Isfahan University of Technology, Isfahan, Iran

Education

2012 - 2018, Isfahan University of Technology (IUT), Isfahan, Iran & Antwerp University, Antwerp, Belgium
Joint PhD. in Condensed Matter Physics

Graduate Coursework:
- Many Body Physics(G:18/20)
- Advanced Electronic Structure Theory(19.50/20)
- Quantum Field Theory I (G:17.50/20)
- Advanced Statistical Mechanics II (G:19.50/20)
- Magnetic Properties of Materials(G:19.50/20)
- PhD GPA: 18.89/20

2009 - 2011, Isfahan University of Technology (IUT), Isfahan, Iran
M.Sc. in Condensed Matter Physics
GPA: 16.05/20

2004 - 2008, Qom University ,Qom ,Iran

B.Sc. in Physics
GPA: 16.20/20

Main research interests

- Topological Insulators
- Weyl Semimetals
- Electronic Properties of 2D Materials
- Many-Body Effects in 2D Materials
- Quantum Transport

Conferences

1-Taghizadeh sisakht, Esmail; Zare, mohammad Hossein; Fazileh ,Farhad ; " Topological origin of edge states in Phosphorene nanoribbons and their electronic structure properties", presented in 12th Conference on Condensed Matter, Isfahan University of Technology,Iran, 2015.

2-Taghizadeh sisakht, Esmail; Zare, mohammad Hossein; Fazileh ,Farhad ; " Phosphorene nanoribbons ,field effect transistors", presented in 12th Conference on Condensed Matter(poster), Isfahan University of Technology, Iran,2015.

3- E Taghizdehsiskht , F Fazileh ,"Numerical study of the effect of disorder and magnetic field on the quantum transport of two-dimensional nanostructures modeled by tight-binding approximation"presented in Conference of Iranian physics Society(poster), Yazd University, Iran, 2012.

Publications

1-E.T.Sisakht, M. H.Zare, and F.Fazileh, "Scaling laws of band gaps of phos- phorene nanoribbons: A tight-binding calculation", Physical Review B, vol.91, no.8, p.085409, 2015.

2-E.T.Sisakht, F. Fazileh, M. Zare, M.Zarenia, and F.Peeters, "Strain-induced topological phase transition in phosphorene and in phosphorene nanorib- bons", Physical Review B, vol.94, no.8, p.085417, 2016.

3-M.Rezaei, E.T.Sisakht, F. Fazileh, Z. Aslani, and F.Peeters, "Tight-binding model investigation of the biaxial strain induced topological phase transition in $GeCH_3$", Physical Review B, vol.96, no.8, p.085441, 2017.

4-Z.Aslani, E.T.Sisakht,H. Ghorbanfekr-Kalashami,F. Fazileh, and F. M. Peeters "Conductance fluctuations of monolayer GeSnH2 in the topological phase using a low-energy effective tight-binding Hamiltonian", Physical Review B,vol 99,no.11,p.115421,2019.

Name and surname:
Esmaeil Taghizadeh
Sisakht
Gender:
Male
Email:
etsisakht28@gmail.com
Citizenship:
Iran
Cell Phone:
+98(917) 8418910
Phone:
+98(31) 33916572

Address:
No.202, Department of
Physics, Isfahan University
of Technology, Isfahan, Iran

5-E.T.Sisakht, M.Zarenia, F. Fazileh, and F.Peeters, "Electronic properties of phosphorene in the presence of one-dimensional supperlattice potentials and magnetic fields", In preparation

6-E.Taghizdehsiskht , F.Fazileh , M.Forozandeh ,"Numerical study of the effect of disorder and magnetic field on the quantum transport of two-dimensional nanostructures modeled by tight- binding approximation" IJPR 2013, 13(1): 9-16.

Teaching

- Lecturer in "University Physics" at Jahad-e-Daneshgahi Institute for Higher Education, 2013-2015, 2017-present.
- Lecturer in "University Physics" at Palayesh Institute for Higher Education, 2013.
- Teacher assistant of "University Physics" ,Physics Dept., Isfahan University of Technology, 2014-2015,2017.
- Teacher assistant of "Many-Body Physics" Physics Dept., Isfahan University of Technology, 2013.
- Teaching of "Physics Laboratory I" course, Isfahan Physics Dept., Isfahan University of Technology, 2011.

Computer skills

OS Systems: Windows, Ubuntu
Programming Languages: C, FORTRAN
Scientific Software Tools: Comsol, Mathematica, Corel Draw, Qtiplot, Xmgrace ,Gnu plot,...

Language Proficiency

Persian: Native
English: Fluent

References

1-Dr. Farhad Fazileh (advisor)
Department of Physics
Isfahan University of Technology
Isfahan, Iran 84156-83111
Phone: +98 (31) 3391-3764
Email: fazileh@cc.iut.ac.ir
————————————

2-Dr. Farhad Shahbazi
Department of Physics
Isfahan University of Technology
Isfahan, Iran 84156-83111
Phone: +98 (31) 3391-3755
Email: shahbazi@cc.iut.ac.ir
————————————

3-Dr. Javad Hashemifar
Department of Physics
Isfahan University of Technology
Isfahan, Iran 84156-83111
Phone: +98 (31) 3391-3732
Email: hashemifar@cc.iut.ac.ir
————————————

4-Dr. Ismaeil Abdolhosseini Sarsari
Department of Physics
Isfahan University of Technology
Isfahan, Iran 84156-83111
Phone: +98 (31) 3391-2376
Email: abdolhosseini@cc.iut.ac.ir
————————————

5-Dr. Mohammad Zarenia
G.U.218 2020 Antwerpen Belgium
Phone: 032653658
Email: m.zarenia@gmail.com
————————————